SKI Report 2007:08

Research

DECOVALEX-THMC

TASK B
Understanding and characterizing the excavation disturbed zone (EDZ)

Phase 2 Report

Edited by:
John A Hudson (SKB, Sweden, and Rock Engineering Consultants, UK)
Lanru Jing (Royal Institute of Technology, Stockholm, Sweden)

February 2007

ISSN 1104-1374
ISRN SKI-R-07/08-SE

SKI

SKI Report 2007:08

Research

DECOVALEX-THMC

TASK B
Understanding and characterizing the excavation disturbed zone (EDZ)

Phase 2 Report

Edited by
John A Hudson, SKB, Sweden, and Rock Engineering Consultants, UK
Lanru Jing, Royal Institute of Technology, Stockholm, Sweden

With contributions from:
Juha Antikainen, Helsinki University of Technology, Finland
Tobias Backers, GeoFrames GmbH,Germany
Ann Bäckström, SKB/Bergbyggkonsult AB, Sweden
Tomofumi Koyama, SKI, Sweden
Xiating Feng and Pengzhi Pan, Chinese Academy of Sciences, China
Akira Kobayashi, Kyoto University, Japan
Mikael Rinne and Baotang Shen, Fracom Ltd., Finland

February 2007

SKI

This report concerns a study which has been conducted for the Project DECOVALEX-THMC. The conclusions and viewpoints presented in the report are those of the author/authors and do not necessarily coincide with those of the SKI.

Foreword

The DECOVALEX-THMC project is an ongoing international co-operative project that was stared in 2004 to support the development of mathematical models of coupled Thermal (T), Hydrological (H), Mechanical (M) and Chemical (C) processes in geological media for siting potential nuclear fuel waste repositories. The general objective is to characterise and evaluate the coupled THMC processes in the near field and far field of a geological repository and to assess their impact on performance assessment:

- during the three phases of repository development: excavation phase, operation phase and post-closure phase;
- for three different rocks types: crystalline, argillaceous and tuff;
- with specific focus on the issues of: Excavation Damaged Zone (EDZ), permanent property changes of rock masses, and glaciation and permafrost phenomena.

The project involves a large number of research teams supported by radioactive waste management agencies or governmental regulatory bodies in Canada, China, Finland, France, Germany, Japan, Sweden and USA, who conducted advanced studies and numerical modelling of coupled THMC processes under five tasks:

- **Task A**: Influence of near field coupled THM phenomena on performance assessment, initiated by CNSC, Canada.
- **Task B**: The Excavation Disturbed Zone (EDZ). MHC studies of the EDZ, initiated by SKB, Sweden.
- **Task C**: Excavation Damaged Zone (EDZ) in the argillaceous Tournemire site, France, initiated by IRSN, France.
- **Task D**: Permanent permeability/porosity changes due to THC and THM processes, initiated Department of Energy, USA.
- **Task E**: THM Processes Associated with Long-term Climate Change: Glaciations case study, initiated by OPG, Canada.

Work defined in these five tasks are divided into different phases or steps so that the progress can be monitored and achievements documented in project reports.

The present report presents the definition, achievements and outstanding issues of the Phase 2 of Task B, concerning numerical modelling and physical testing of the complete stress-strain curve of intact rock samples in uniaxial compression and comparison with physical testing results.

Lanru Jing, Fritz Kautsky, Ove Stephansson and Chin-Fu Tsang

Stockholm, Sweden
February 2007

Summary

This report summarizes the work contributed to Phase 2 of Task B of the international DECOVALEX-THMC project, which took place during the period of March 2004 to May 2006. The Phase 2 work incorporated the use of a wide range of numerical models to simulate the failure of a number of intact rock core samples, from the APSE tunnel at Äspö HRL, as tested in uniaxial compression and other loading conditions with the intention of establishing the common and code-specific features of the models. The core samples of the Äspö diorite were treated with different initial mechanical and chemical conditions as dry samples, saturated with distilled water, formation water and saline water, with different durations of submersion, respectively, in order to observe the mechanical effects of saturation by different chemical fluids on the mechanical properties of the intact core samples.

In order to understand the physical-chemical processes involved and the damage mechanisms of the cores, various numerical modelling approaches were applied to simulate the core testing, including FEM, DEM, BEM and EPCA (Elasto-Plastic Cellular Automata) methods. The application of such widely different numerical approaches provides a very useful platform for deeper understanding of not only the main features of numerical methods but also their characteristics for representation of the damage mechanisms.

This report presents the definition of the Phase 2 work, core testing procedures and results, results of numerical modelling by different teams and the concluding remarks and outstanding issues in general. The research teams are now in a position to predict the main detailed mechanistic trends relating to the development of the EDZ. The next stages of the Task B work, the Benchmark Test, assessing uncertainties and writing up the Guidance Document on characterising and measuring the EDZ will thus all be supported by the successful Phase 2 work described in this Report.

Content

1. Introduction

John A. Hudson[1,2]
[1]Swedish Nuclear Fuel and Waste Management Co. (SKB), Stockholm, Sweden
[2]Rock Engineering Consultants, UK

1.1 Background

The objective of Task B of DECOVALEX-THMC is to improve understanding of the evolution of the Excavation Disturbed Zone (EDZ) and to be able to numerically model the EDZ THMC mechanisms in a fractured crystalline rock mass within the context of radioactive waste disposal. A deeper understanding of the EDZ will be developed through understanding the driving forces, the couplings including chemical processes, the evolution through excavation, emplacement and closure, and a greater ability to explicitly incorporate the EDZ in PA/SA assessments. There will be studies of the crack/fracture evolution, the distinction between the mechanical and flow EDZs, establishing to what extent a coupled model is required, establishing how to cope with uncertainties, and the utilisation of physical data available from the Äspö Hard Rock Laboratory (HRL) for comparison with the numerical models. The work will conclude with the preparation of a Guidance Document for characterising and measuring the EDZ in a newly excavated environment in crystalline rock.

It is helpful to note at the outset that there is an inevitable EDZ occurring as a consequence of the mechanical changes related to the fact that rock is removed during underground excavation for a repository. Then, there is an additional EDZ component resulting from the type of excavation method used. The inevitable EDZ occurs because, when an excavation is made in a rock mass, changes in the physical variables involved are inevitable. In particular,

- the resistance of the rock previously occupying the excavation has been removed so the surrounding rock will move inwards,
- the magnitudes and orientations of the in-situ stress states are altered so that the principal stresses become parallel and perpendicular to the excavation surface, and
- the hydraulic pressure has been reduced to atmospheric pressure and so the excavation becomes a sink.

Supplementary to these inevitable effects, the additional EDZ component occurs as a result of the additional perturbations introduced by the excavation method. Blasting generally causes greater perturbations than the use of a tunnel boring machine because in blasting all the energy required to fracture the rock is input in the order of a second; whereas, with a tunnel boring machine, the energy is continuous input at a lower power level, resulting in less additional disturbance.

The stages of the development and evolution of the EDZ that are being studied (Fig. 1.1) are:

Stage 1. Initial construction – which alters the mechanical, hydrological and chemical circumstances;
Stage 2. A period when the excavations are left open – when drying of the rock occurs, water flows through the fractures and the chemistry changes; and
Stage 3. After the canisters and backfill are emplaced, the temperature increases and equilibrium is re-established over a long time period

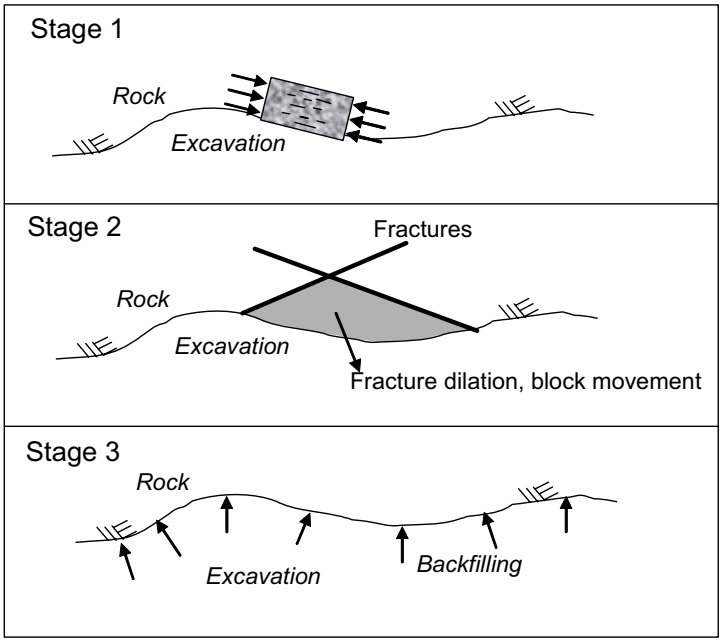

Figure 1.1. Stages of EDZ development during the repository lifetime.

1.2 Task B organisations

The organisations and their representatives participating in the Task B work are as follows:

Research Teams
SKB (Sweden): John A Hudson, Rolf Christiansson, Ann Bäckström
SKI (Sweden): Lanru Jing, Tomofumi Koyama
DOE (USA): Jonny Rutqvist, Eric Sonnenthal
CAS (China): Xia-Ting Feng, Pengzhi Pan
JNC (Japan): Akira Kobayashi, Tomoo Fujita, Masakaya Chijimatsu,
Finnish State Nuclear Waste Management Fund (Finland): Mikael Rinne

The Task Force leader is John A Hudson, SKB, with Lanru Jing (Secretariat, KTH) as the co-leader and Ivars Neretnieks (KTH) as the expert for peer review of the works.

1.3 The Task B research plan and program of work

The Task B research plan is based on building up an understanding of the EDZ and consists of the following components.

- Understand and characterize the complete failure of intact rock in uniaxial compression using different numerical models, physical testing with chemical effects and co-ordination of the results.
- Characterize the failure of intact rock in the same way and with fractures.
- Benchmark test (BMT) modelling of the EDZ with heat, water, chemical effects and failure, with and without pre-existing fractures.

- Development of a method for dealing with uncertainties.
- Use of the Äspö HRL, Sweden, EDZ in-situ experimental work involving tunnel wall sampling, crack mapping and integration of all the information.
- Development of a method to characterize and measure the EDZ in a new crystalline rock situation.

To achieve these aims, the Task B programme of work is comprised of the six associated Phases as follows.

Phase 1 Compilation of literature/information on the EDZ and hydro-chemistry aspects
Phase 2 Numerical modelling and physical testing of the complete stress-strain curve of intact rock samples in uniaxial compression and comparison with physical testing results.
Phase 3 Benchmark testing (BMT) modelling of the EDZ evolution
Phase 4 Use of experimental data from the Äspö HRL, Sweden
Phase 5 Development of a method for dealing with modelling uncertainties
Phase 6 Production of a Guidance Document for characterising and measuring the EDZ in a newly excavated environment in crystalline rock.

These Task B Phases, i.e. sub-tasks, are essentially sequential in nature, but they are being carried out to some extent in parallel because of the significant overlaps in the Phases. A flowchart of the six Phases comprising the programme of work is shown in Fig. 1.2.

1.3.1 Phase 1: Compilation of literature/information

For the Task B EDZ work, it was considered useful to collect the literature pertaining to both the EDZ and the chemical aspects. The latter is a new topic since DECOVALEX-THMC includes chemistry for the first time in the DECOVALEX works. The literature survey is facilitated by recent workshops and seminal papers (Tsang, 2005) as well as collection and analysis of EDZ phenomenon by the individual teams, and will progress with the whole period of the project.

1.3.2 Phase 2: Numerical modelling of the stress-strain relation for intact rock and associated physical testing

During the evolution of the EDZ, there are several processes operating. The initial phase is microcracking in the excavation-proximate rock caused by an increase in the local stress, *cf.* Stage 1 in Fig. 1.1. Thus, the Phase 2 work is aimed at understanding and being able to numerically model this initial microcracking in the intact rocks.

In the rock mechanics discipline, considerable research has been devoted to this subject in the past. The new contribution that the Phase 2 work will make is

- the use of a variety of up-to-date numerical simulation models using similar input data,
- assessment of the numerical simulations to indicate which aspects of the results are common to all the codes and which are code-specific,

- consideration of the chemical effects, and
- comparison of the numerical results and the physical testing results from Äspö cores tested under controlled saturation and chemical conditions.

The numerical work is supported by physical testing, see Figs. 1.3a and 1.3b. The large rings at the top and bottom of the specimen hold the axial displacement transducers; the chain around the central portion of the specimen is the circumferential displacement transducer. (Äspö diorite rock core; photograph taken in the SP Lab, Borås, Sweden).

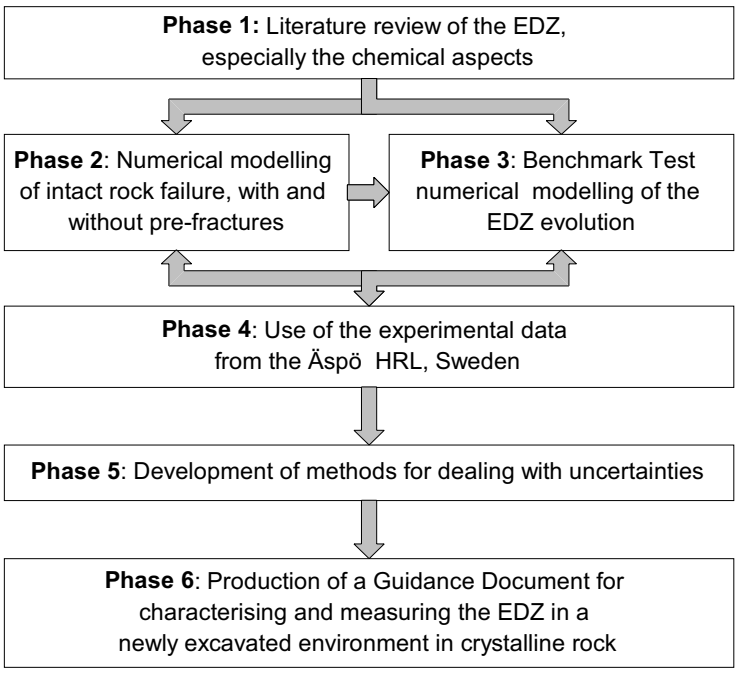

Figure1. 2. Flowchart of the six phases comprising the DECOVALEX-THMC Task B programme of work

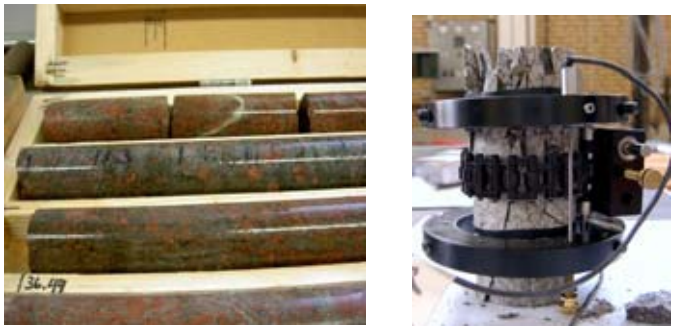

(a) (b)

Figure 1.3 a) Äspö HRL rock cores selected for the uniaxial rock testing programme: b) A rock specimen on completion of the complete stress-strain curve testing in uniaxial compression.

1.3.3 Phase 3: Benchmark test (BMT) modelling of the EDZ evolution

As indicated in the sketch in Fig.1.4, removal of rock for repository construction causes the rock to move inwards (because the rock modulus has been reduced to zero), the rock principal stresses to be lined up parallel and perpendicular to the excavation

surface (because at the surface there are no longer significant shear stresses), the ground water to initially move into the excavation (because the pressure has been reduced to atmospheric), and in time causes reduced rock fracture permeability because of chemical precipitation.

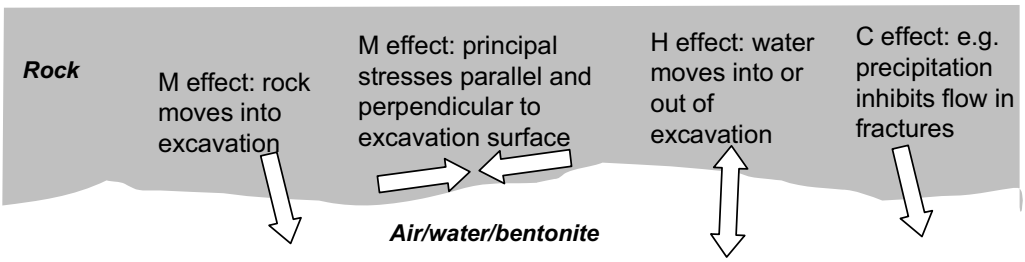

Figure 1.4. Sketch of the HMC effects in the wall of the repository deposition tunnels and deposition holes.

Thus, and as shown in Fig. 1.2, following the numerical modelling and physical testing of rock cores in Phase 2, it is necessary to simulate the EDZ circumstances using a BMT numerical model. A generic crystalline fractured rock model has been established to characterize the HMC effects in the EDZ, see Fig. 1.5. This will include the development of cracking and fractures, movement of loose blocks/solid rock inwards, the interaction between the EDZ stress and the rock fracture apertures, permeability studies of the EDZ fractured rock, and possibly including the chemical effects, concentrating on chemical precipitation in fractures and the effect on the fractures (because data on the long-term inflow is available from Äspö HRL). A key output from the EDZ modelling will be evaluation of whether the EDZ effects can be studied separately or whether it is essential to use a coupled model.

The following repository stages will be studied:

1) **Excavation:** Initial construction of the excavation, which alters the mechanical, hydrological, and chemical circumstances
2) **Pre-emplacement:** A period when the excavation is left open as drying of the rock occurs, water flows through the fractures, and the chemistry changes
3) **Post closure:** A period after the waste and back-fill is emplaced, when the block is exposed to high temperature and thermal stress and (later) cooling and stress relief, and then establishment of equilibrium over a long time period.

The work required for this BMT should be conducted via the following stages:

Stage 1 **Linear thermal-hydro-elastic modelling:** Model inception with linear elastic properties

Stage 2 **Non-linear failure modelling:** Extend model to include non-linear and elasto-plastic properties for failure analysis

Stage 3 **Time-dependent failure modelling:** Extend model to include time-dependent changes in mechanical properties for analysis of creep and mechanical degradation

Stage 4 **Chemo-mechanical modelling (optional):** Extend model to include simplified chemical modelling of time-dependent pressure solution/stress corrosion, or other chemo-mechanical effects

Stage 5 **Full THMC modelling (optional):** Implement chemo-mechanical model developed under Stage 4 to link THC and THM models into a fully coupled THMC model.

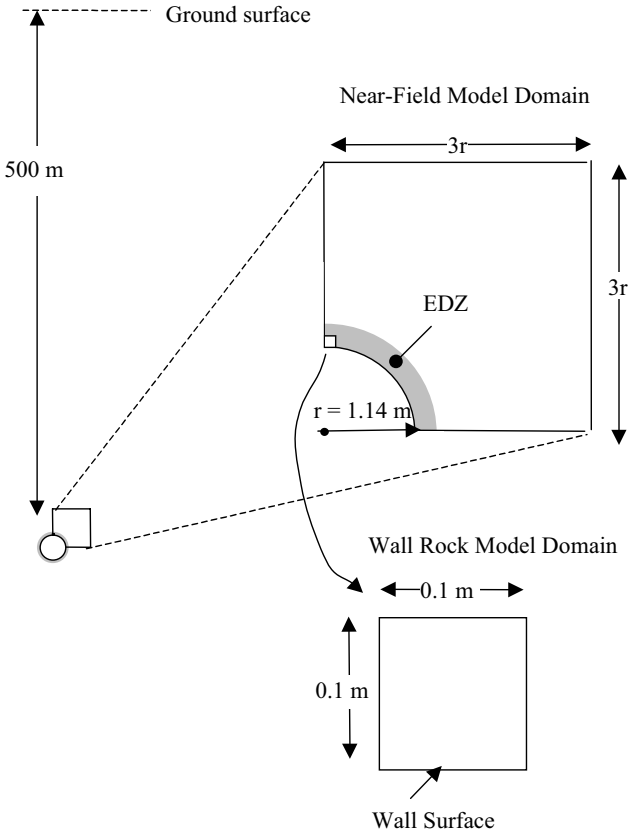

Figure 1.5. Two model sizes for detailed analysis of coupled THMC processes in the EDZ of a deposition tunnel or shaft.

1.3.4 Phase 4: Use of experimental data from the Äspö HRL, Sweden

For some years, SKB have managed the Äspö HRL in Sweden and conducted in-situ experiments related to radioactive waste disposal. The most recent of these experiments has been the Äspö Pillar Stability Experiment (APSE) at the 450 m level, involving the excavation of a tunnel and two deposition holes. The intention of the experiment is to study the stability of the rock hosting the deposition holes – by orientating the tunnel to be perpendicular to the maximum normal horizontal stress component and excavating the deposition holes close together. In this way the rock stress is significantly concentrated in the pillar between the deposition holes and spalling may occur. The specific purposes of the experiment is to: demonstrate the capability to predict spalling in a fractured rock mass; demonstrate the effect of backfill (confining pressure) on the rock mass response via a pressurised bladder in one of the deposition holes; and compare the 2D and 3D thermal predictive capabilities. The pillar response has been predicted by several numerical codes and the results from those codes are being compared to each other and the actual measured results. The ASPE experiment is described in Andersson (2004) and Anderson et al. (2004) and the tunnel blasting in Olsson et al. (2004).

SKB have a programme for assessing the EDZ in the APSE tunnel. This has involved a study of the blasting technique (Olsson et al., 2004) and the types of cracking that have occurred in the tunnel-peripheral rock (see Fig. 1.6) and at the top of the deposition holes.

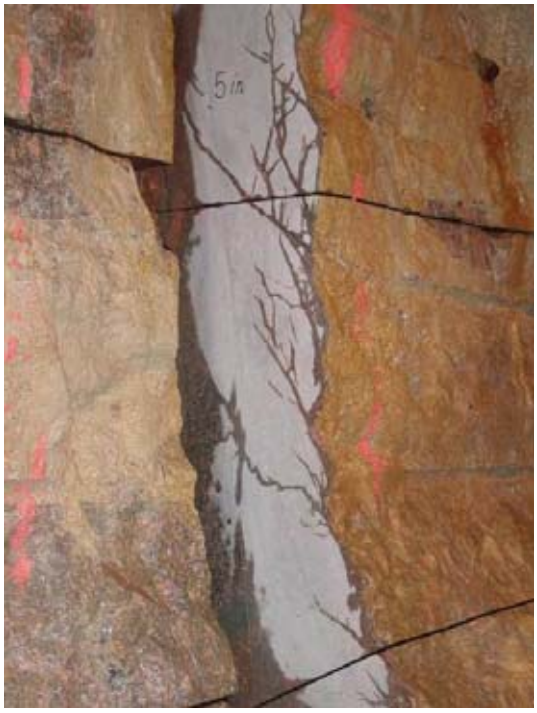

Figure 1.6. A slot cut in the wall to study the EDZ. Note the blasting-induced cracks.

1.3.5 Phases 5 and 6: Development of a method for incorporating uncertainties and preparing an EDZ Guidance Document

In Phase 5 of the work for Task B, emphasis will also be placed on dealing with the uncertainties, and how to track uncertainty in the data and models making sure that the specified uncertainties do in fact span the uncertainty space. It can be seen in Figure 1.2 that Phase 5 occurs after the numerical modelling of the laboratory failure in Phase 2, the BMT modelling in Phase 3 and the use of the field data in Phase 4. Thus the work on uncertainties has not yet been started in earnest.

Similarly, preparation of the EDZ Guidance Document, which will utilise all the research results, will begin in the summer of 2007, i.e. towards the end of the project duration.

This report is concerned with the results of Phase 2, including the laboratory tests on rock core samples (Chapter 2), and numerical modelling of the core tests by different teams (Chapters 3-6) and the summary of the current understanding and outstanding issues regarding intact rock failure types and damage mechanisms (Chapter 7).

Acknowledgements

The Funding Organisations for DECOVALEX THMC in the period 2004-2007 are gratefully thanked for their support of the Task B work outlined in this Chapter and as described in the succeeding Chapters

References

Andersson, J. C., *Äspö stability experiment. Summary of preparatory work and predictive modelling*. SKB Report R-03-02, 2004.

Andersson, J. C., Martin, C. D. and Christiansson, R., SKB's *Äspö stability experiment, Sweden. Proceedings of Gulf Rocks 2004 "Rock mechanics across borders and disciplines",* June, 2004.

Olsson, M., Niklasson, B., Wilson, L. Andersson, J. C., and Christiansson, R., *Äspö HRL. Experiences of blasting of the TASQ tunnel.* SKB R-04-73, 2004.

Tsang, C.-F., Bernier, F. and Davies, C., *Geohydromechanical processes in the Excavation Damaged Zone in crystalline rock, rock salt, and indurated and plastic clays—in the context of radioactive waste disposal. Int. J. Rock Mech. & Min. Sci.,2005 (42)*, 109–125.

2. Laboratory tests on Äspö Diorite

Ann Bäckström[1], Juha Antikainen[2] and Tobias Backers[3]
[1]Bergbyggkonsult AB, Solna, Sweden,
[2]Helsinki University of Technology (TKK), Finland
[3]GeoFrames GmbH, Potsdam, Germany.

2.1 Introduction

A series of laboratory tests has been performed to address the chemical and time dependent effects on the mechanical strength of a crystalline rock mass. The results from three campaigns of tests performed on specimens of the Äspö diorite from the Äspö HRL are presented here.

In the first set, compression tests were performed on specimens subjected to different chemical conditions, focusing on saturation with fluids of different salinity. These tests have been conducted at the Swedish National Testing and Research Institute (SP) in Borås, Sweden. They will increase the understanding of how the mechanical properties of Äspö diorite are affected by chemical processes. Moreover, the results are going to be used in models for simulating the deterioration of the rock matrix due to chemical processes. The loading is carried out until the post-failure regime in order to study the mechanical behaviour of the rock after cracking.

The second set was tested at Helsinki University of Technology, Finland, where the tests consist of uniaxial compression tests with acoustic emission monitoring, indirect tensile tests (Brazilian test), triaxial tests (with constant axial strain rate control) and strain rate stepping tests (with constant axial displacement rate control). In this laboratory campaign the Strain Rate Stepping Test was selected because there is better control of the failure of brittle rock specimens compared to other creep tests. The testing methods (except the strain rate stepping test) and equipment are described in detail in Hakala et al. (1997). This long term testing is used to provide data to be compared to a time-dependent model of rock strength and deformability. The results from these tests show that the problems of creeping in hard rock testing related to the heterogeneity of the rock material can be dealt with during strain rate stepping tests.

The third contribution summarises the experimental investigation program on time-dependent behaviour of saturated Äspö diorite. It includes the development of new methods to determine parameters describing the subcritical crack growth under tensile and shear loading. These parameters, such as the subcritical parameters A and n (Charles, 1958), are needed to numerically model the behaviour of brittle rock specimens during laboratory experiments. There are very few methods available to determine these parameters, and if so, for Mode I (tensile) fracture growth only. This contribution explains the new experimental procedures developed to determine A and n for Mode I and Mode II by means of a statistical approach to the laboratory results. These tests were developed and conducted by GeoFrames GmbH in Germany

2.2 The influence of salinity on the uniaxial compressive strength of the Äspö Diorite

Uniaxial compression tests, with loading beyond the failure point into the post-failure regime, have been conducted on dry and water-saturated specimens sampled from boreholes KF0066A01 and KF0069A01 retrieved from the Äspö HRL. These tests belong to one of the activities performed as part of the project DECOVALEX IV, Task B (HMC Studies of the Excavation Disturbed Zone (EDZ) in Crystalline rock) lead by the Swedish Nuclear Fuel and Waste Management Co (SKB). The tests were carried out in the material and rock mechanics laboratories at the department of Building Technology and Mechanics at the Swedish National Testing and Research Institute (SP). The results are reported in (Jacobsson and Bäckström, 2005).

2.2.1 Method

Uniaxial compression tests (UCS) with deformation into the post-failure regime were carried out on 20 cylindrical specimens of intact rock. To prevent any bias of the results due to structural differences between the specimens, the specimens were taken in a "cyclic order" from two 51 mm cores, drilled horizontally, 3 m apart from each other at the 450 m level of Äspö HRL, Sweden (Fig. 2.1). The specimens were prepared for the uniaxial compression test according to the ISRM standard (Fairhurst and Hudson, 1999) with exception for the water saturation.

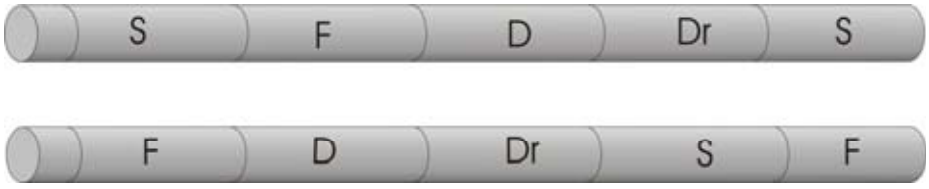

Figure 2.1. Example of cyclic sampling of the cores where the (S) is the specimens subject to saline environment, (F) formation water, (D) distilled water and (Dr) are dry conditions.

The wet density of the specimens as well as the open porosity was determined according to the standard EN 1936 (1999). After the determination of the wet density and open porosity the specimens were dried in an oven at 105 °C until a constant mass was reached. The specimens were saturated with saline formation water and distilled water. Five specimens were dried and the remaining 15 specimens, with 5 specimens of each type, were water saturated with distilled, formation and saline water (10% NaCl solution) respectively. The water denoted as "formation water" in this study is retrieved at the same depth as the specimens and has a pH of about 7 and a salinity of about 0.68%, which denotes a weak salinity. To investigate the saturation time aspect, the five specimens saturated with distilled water were divided into two groups with three specimens submerged for 90 days and two specimens submerged for 40 days. The five specimens saturated in formation water were also sub-divided into two groups: one group with two specimens saturated in formation water for 90 days; and a second group of three specimens saturated for 40 days.

When conducting the UCS tests, the surface of the saturated specimens was dried with paper to enable the connection of all the gauges to the specimens. The axial deformation was measured using two independent systems: one attached to the loading plates and one attached to the specimens. The radial deformation was obtained from a chain mounted around the specimen at about mid-height. The chain was connected to a LVDT gauge (Fig. 2.2). The specimens were tested in a servo-controlled testing machine especially designed for rock tests with a load cell with maximum capacity of 1.5 MN and an uncertainty of < 1%. In order to obtain the complete response of the post-failure regime, the uniaxial compression tests were carried out using circumferential strain as the feed-back signal.

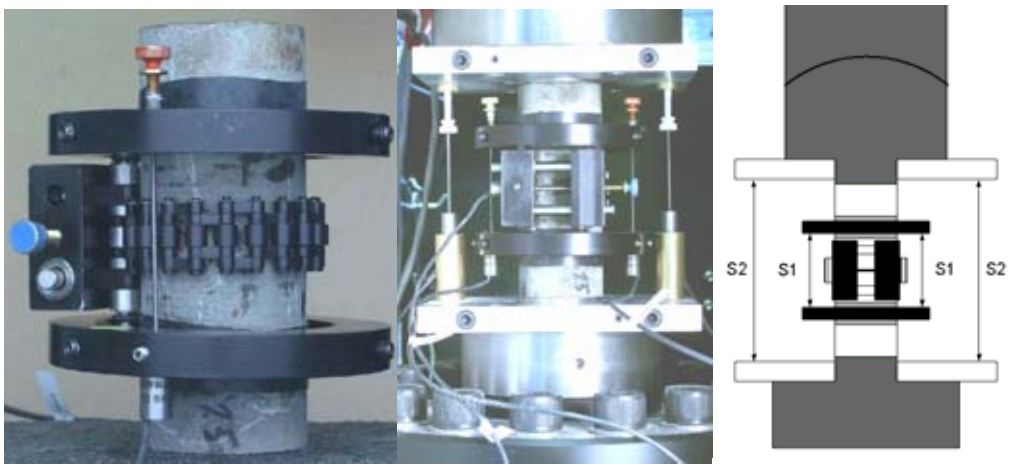

Figure 2.2: Left: Rings, LVDTs and chain for local axial and radial deformation measurements. Middle: Specimen inserted between the loading plates with the two separate axial deformation measurement devices (Jacobsson and Bäckström, 2005). Right: Principal sketch showing the two systems used for the axial deformation measurements. System (S1) that measures the local axial deformation (rings) and system (S2) that measures the deformation between the aluminium plates (total deformation)

2.2.2 Data analysis

During the uniaxial compression test, the axial stress (σ_a), axial strain (both ε_a local and ε_a total) and the radial strain (ε_r) were retrieved. The uniaxial compressive strength (σ_c) was obtained as the highest axial stress for the individual specimens. From these parameters the Young's modulus (E) of each specimen was calculated from the slope of the stress-strain curve between 40-60% of the UCS and the Poisson's ratio (ν) as the slope of the radial strain-axial strain curve between 40-60% of the UCS. The crack initiation stress (σ_{ci}) was determined using the method suggested in Martin and Chandler (1994). The crack initiation stress is obtained from the deviation from the elastic response of the specimen as the axial cracking starts in the pre-peak region of the stress-strain curve. It is obtained from the crack volumetric strain curve. By subtracting the elastic volumetric strain from the total volumetric strain measured from the specimens the crack, volumetric strain is obtained. The total volumetric strain of the specimens subject to UCS tests is calculated as:

$$\varepsilon_{vol} = \varepsilon_a + 2\varepsilon_r \tag{2.1}$$

where ε_{vol} is the total volumetric strain, the ε_a is the axial strain and the ε_r is the radial strain measured during the test. Thus the crack volumetric strain is calculated by:

$$\varepsilon_{vol}^{cr} = \varepsilon_{vol} - \frac{1-2\nu}{E}\sigma_a \tag{2.2}$$

where ε_{vol}^{cr} is the crack initiation stress, the ε_{vol} is the total volumetric strain, ν is the Poisson's ration. The E is Young's modulus and σ_a is the axial stress. In Martin and Chandler, the elastic volumetric strain is expressed as:

$$\varepsilon_{vol}^{e} = \frac{1-2\nu}{E}(\sigma_1 - \sigma_3) \tag{2.3}$$

where ε_{vol}^{e} is the elastic volumetric strain, σ_1 is the major principal stress and the σ_3 is the minor principal stress. The minor principal stress in uniaxial compression stress tests is 0, thus σ_a in equation (2.3) equals σ_1.

After retrieving the crack volumetric strain curve, an adjustment to scale is made so that the maximum value of the curve is set to 0. The crack initiation stress is visually obtained as the first non-zero point of the fitted crack volumetric curve (Eloranta and Hakala, 1999).

The slope of the post-failure curve is calculated from the maximum load of each post-failure cycle. Examples of the linear trend of these maxima are plotted in Fig. 2.3.

2.2.3 Results

The laboratory results have been obtained at the Swedish National Testing and Research Institute (SP) in Borås, Sweden.

2.2.3.1 The stress-strain curves

The behaviour of a brittle rock, such as granite, can be described according to the five regions presented in Martin and Chandler (1994) (Fig. 2.4). The region of the test where the specimens act as an elastic material (Elastic region II) can be described by the Young's modulus. The onset of the region of stable crack growth III is represented by the crack initiation stress and the results can be found in Tables 2.1 and 2.2 together with the resulting UCS that represent the boundary between region IV (the region of unstable cracking) and V (the post-peak region).

Due to a pre-existing flaw, undetectable by ocular investigation, one of the specimens prepared for the saline solution has been excluded from this study. Hence the group is limited to four specimens saturated with saline water.

When comparing the resulting axial stress-strain curve for the different groups of samples (i.e. dry, saturated with distilled, formation or saline water) the saline samples exhibited different behaviour in several ways compared to the other groups (Fig. 2.3).

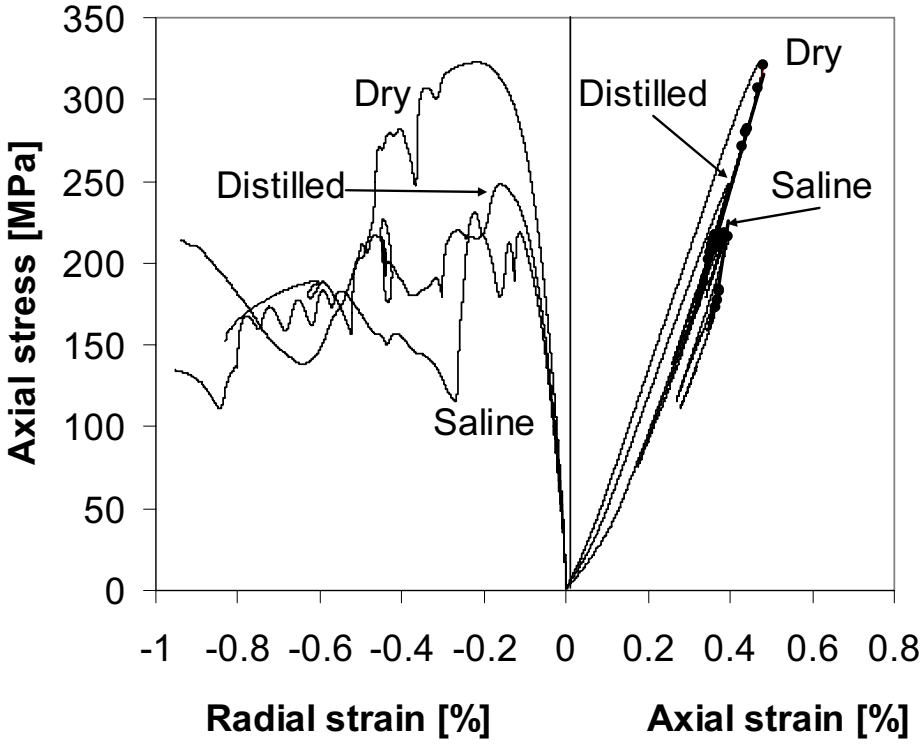

Figure 2.3: Stress-strain curve for three specimens subjected to dry conditions, distilled water and saline water for 90 days each, where the filled circles are the maximum load of each post-failure cycle.

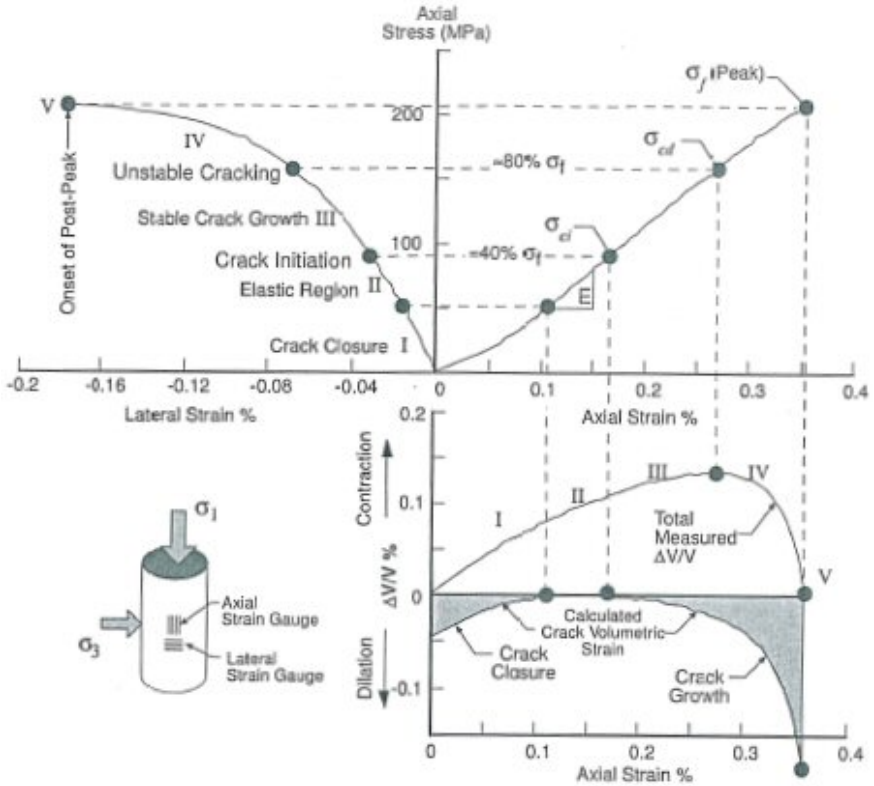

Figure 2.4. Stress-strain diagram from UCS test on Lac du Bonnet granite (from Martin and Chandler, 1994).

2.2.3.2 The elastic region

A contrast between the results for the saline and for the dry specimens can be discerned when looking at the Young's modulus (i.e. the inclination of the elastic response of the specimens) for the different groups of specimens (Table 2.1). The values are lower for specimens subjected to the saline solution compared to the ones at dry conditions, or subjected to distilled water and formation water (subject to formation water for 40 days). The group of specimens subjected to formation water displays a Young's modulus rather similar to that of the saline specimens. The maximum value of the Young's modulus for the group subjected to saline water is similar to the minimum value of the group subjected to distilled water. The ranges of variation for the dry and saline groups are 2.3 and 2.7 GPa respectively. The difference between the maximum value for the saline group and the minimum value for the dry group is 2.6 GPa. The group with specimens subjected to distilled water for 90 days shows a Young's modulus slightly lower than that for dry specimens.

2.2.3.3 Uniaxial compressive strength (UCS) and crack initiation stress

The dry specimens generally exhibited higher uniaxial compressive strengths than specimens saturated with any of the three different fluids in this study. The dry specimens display a uniaxial compressive strength about 10% higher than that of distilled water. The three specimens subjected to distilled water for the same interval of time as the saline specimens exhibit a UCS varying between 249 and 287 MPa; whereas, the specimens subjected to the saline solution vary between 277 and 220 MPa (Table 2.1).

The crack initiation stress calculated for the different specimens mimics the results of the UCS. Here also, the highest values can be found among the dry specimens (Table 2.1). The specimens subjected to the saline solution have rather lower crack initiation stress, which ranges between 115 MPa and 143 MPa. The maximum value for this range only touches the lower limit of the range for the dry specimens. This can be considered in relation to the values for distilled water that ranges from 132 to 151 MPa, where the high values are well within the range of the dry specimens.

2.2.3.4 Time aspects

The specimen with the highest UCS among the saturated groups can be found among those subjected to formation water. The three specimens saturated with formation water for 40 days have a high average UCS of 298 MPa (Table 2.2) compared to the two specimens subjected to formation water for 90 days, which have an average UCS of about 249 MPa (Table 2.1). The difference between the results for the three specimens subject to distilled water for 90 days and the two specimens submerged for 40 days is negligible (270.5 compared to 270.9 MPa, respectively). The specimen with the highest Young's modulus can be found in the group of three specimens subjected to formation water for 40 days (73.4 GPa).

Table 2.1. Failure mechanical properties of the specimens tested in different chemical conditions (after 90 days immersion).

Specimen group		UCS [MPa]	Crack initiation stress (σ_{ci}) [MPa]	Young's modulus (E) [GPa]	Slope of the post failure locus [GPa]
Dry	Min.	273.9	140	70.4	87
	Ave.	302.3	157	71.6	95
	Max.	335.8	179	72.7	111
Distilled	Min.	249.4	132	67.5	85
	Ave.	270.5	142	68.5	101
	Max.	287.4	151	69.4	111
Formation	Min.	232.8	126	66.1	84
	Ave.	248.5	133	66.6	97
	Max.	264.2	140	67.2	115
Saline	Min.	220.4	115	65.1	82
	Ave.	249.4	130	66.8	141
	Max.	277.0	143	67.8	209

Table 2.2. Pre-failure mechanical properties of the specimens tested in different chemical conditions (after 40 days immersion).

Specimen group		UCS [MPa]	Crack initiation stress (σ_{ci}) [MPa]	Young's modulus (E) [GPa]
Distilled	Min.	262.6	139	72.1
	Ave.	270.9	141	72.3
	Max.	279.1	143	72.4
Formation	Min.	291.6	153	71.8
	Ave.	298.1	155	72.8
	Max.	305.1	159	73.4

All specimens in this group display a high Young's modulus (Table 2.2) quite similar to the Young's modulus for the dry specimens (Table 2.1). The specimens subjected to the formation water for 90 days show a similar Young's modulus (66.1-67.2 GPa) to that of the specimens subjected to saline water. The specimens subjected to distilled water also display a difference between the subgroups submerged for 40 days, compared to the ones submerged for 90 days. In addition, the two specimens submerged for the shorter time display a higher Young's modulus (72.1-72.4 GPa) than the three specimens submerged for 90 days (67.5-69.4 GPa).

2.2.3.5 Failure mode

The post-failure locus seen in Fig. 2.3 shows a different behaviour for the saline water saturated specimens compared to the distilled water saturated specimens and dry specimens. The general trend is that the slope of the failure locus for several of the saline water saturated specimens is higher than that of the specimens from all the other groups (Table 2.1). The groups of specimens saturated with distilled or formation water show a post-failure pattern similar to that of the dry specimens.

2.2.4 Discussion

On average, five specimens were collected and tested for each water condition. The number of specimens required to guarantee the representativity of a specimen sample from a population is a classical problem in statistics. This is especially true when testing geological materials such as crystalline rocks due to their potential heterogeneity.

Several of the mechanical properties of the specimens, as they were uniaxially compressed, varied both with time and fluid solution. These different properties are probably a response to a similar phenomenon. Regarding the effect of a saline solution on the UCS, the change is about 17% when comparing the average values for the UCS for the dry and saline specimens. In other words, the saturated specimens require a lower energy for creating a new fracture surface area (lower specific work of fracture) than the dry ones (Karfakis and Akram, 1993). Laboratory experiments by Feng et al. (2001) show that the salinity has a negative effect on the UCS of granite specimens. A decrease of up to 33% compared to dry specimens in the shear strength of sandstone was also observed by Feucht and Logan (1990).

The difference in Young's modulus between the dry specimens and the specimens saturated with saline water could be explained by the lack of a lubricant effect in the dry samples and the effect of the salinity, primarily for the biotite minerals.

The longer the time the specimens are exposed to a weak saline solution the larger the effect on the elastic behaviour of the specimen will be. The specimens saturated with saline water exhibit a larger decrease in elastic properties than the specimens saturated with distilled water. The post-failure behaviour of the specimens in terms of the slope of the post-failure locus is also affected by the fluid composition. All of these results indicate that a saline solution makes the rock specimens softer and more ductile, i.e. tending towards Class I behaviour.

The increase in salinity of the pore water seems to lead to lower strength and stiffness of the specimens. This behaviour can be explained by the development of an electro-catalytical osmotic pressure that may facilitate the propagation of the crack tips during loading (Karafakis and Akram, 1993). Another explanation for such a decrease in strength and stiffness might be weathering due to exchange of potassium with sodium ions in the biotite. This substitution involves effects on the superficial layer and an enlargement of interlayer distance of the biotite, sometimes associated with the formation of kaolin (Rausell-Colom et al, 1965; Malmström et al, 1995).

2.3 Uniaxial, Brazil and strain rate stepping testing of Äspö Diorite

The specimens of Äspö diorite were selected carefully with the aim of selecting as homogenous and identical specimens as possible. The number of specimens selected was based on the core availability, the possibility of using previous testing results for the same material, and time and budget constraints. Because the available cores were visually heterogeneous, six sets of four consecutive specimens for the four different tests described below were selected within visually uniform core portions. In particular, the specimens for triaxial and strain rate stepping tests were taken as close to each other as possible, because their similarity is of paramount importance in interpretation of strain rate test results.

The samples were prepared and tested as far as possible according to the ISRM Suggested Methods (ISRM SM 1978, 1983, 1999). All specimens were either dry or saturated with different fluids according to the test design before testing.

The tests consisted of:

- uniaxial compression tests with acoustic emission monitoring
- indirect tensile tests (Brazilian test)
- triaxial tests (in constant axial strain rate control)
- strain rate stepping tests (in constant axial displacement rate control)

The testing methods (except the strain rate stepping test) and equipment are described in detail in Hakala and Heikkilä. 1997.

2.3.1 Uniaxial and Brazil tests

The testing was made according to ISRM Suggested Methods (ISRM SM 1978, 1999) with a MTS 815 Rock Mechanics Testing equipment.

Both in the indirect tensile tests (Brazilian test) and in the uniaxial compression tests a large variation in rock strength was observed (Table 2.3). This produced some problems with the planning of strain rate stepping tests, because the duration of tests depends on the stress level where the stepping is started. If strain rate stepping is started at very low stress level, the duration of single test may be several days. On other hand, if the starting stress level is too high, very fast specimen failure will result and the time-dependent behavior is not recorded.

Table 2.3. The location, dimensions, saturated density, uniaxial compressive strength UCS, modulus of elasticity (Young's modulus) E and Poisson's ratio of uniaxially tested specimens. The indirect tensile strength values at the same locations are presented for comparison.

Drillhole N:o	Depth (m)	Length (mm)	Diam. (mm)	Dens. (kg/m³)	UCS (MPa)	Tensile strength (MPa)	E (GPa)	Poisson's ratio
KF0066A01	26.40	129.3	50.8	2720	185.3	11.1	61.6	0.32
KF0066A01	36.04	129.3	50.8	2673	270.2	17.1	70.1	0.31
KF0066A01	38.95	129.8	50.8	2683	300.0	14.9	69.9	0.31
KF0066A01	49.89	129.8	50.8	2670	257.4	16.6	70.4	0.29
KA3376B01	12.08	130.3	50.8	2743	182.1	13.5	63.0	0.32
KF0069A01	45.77	129.5	50.7	2677	301.6	18.1	71.2	0.32

2.3.2 Strain rate stepping test

The ultimate goal of long-term testing of rock is usually to construct a time-dependent model of rock strength or deformability, or even both. It is shown here that the problems in hard rock creeping tests due to the heterogeneous rock material can be dealt with by using the strain rate stepping test. The experiments in this study provide well-documented laboratory test cases for later comparison with the results of numerical models.

Typical compression tests are:

- Constant Stress Test, where the time-to-failure is recorded at different constant stress values,
- Fixed Strain or Stress Relaxation Test, where the axial strain is kept constant and the changes in load and radial strain are recorded,
- Stress Stepping Test, where the axial stress is increased and possibly decreased stepwise while the strains are recorded,
- Strain Rate Stepping Test, where the axial strain rate is varied while the strains and axial stress are recorded (Lockner, 1998).

Each of these methods has specific advantages and disadvantages. The main advantage of Strain Rate Stepping Test, compared to the two first tests, is that the testing time is much shorter and predictable. Furthermore, in this laboratory campaign, the Strain Rate Stepping Test was selected due to the better control of the failure of brittle rock specimens.

2.3.3 Description of strain rate test

The specimens are prepared according to the respective ISRM Suggested Method. The instrumentation of specimens consists of one strain gauge glued onto the specimen surface and two axial and one chain extensometer attached outside the thin protective neoprene jacket. The interpretation of strain rate stepping tests also requires results from triaxial tests as reference. The standard triaxial experiment is done at loading rates of 0.5 – 1.0 MPa/s. In the first series the confining pressure P is 7 MPa, which provides a reasonably stable process. As the critical inelastic strain is a function of confining pressure (Lockner, 1998), additional tests with lower confining pressure are underway. The specimen is tested with axial strain rate control corresponding to the above loading rate. The peak differential stress value $\sigma_{\Delta po}$, inelastic strain rate $\acute{\varepsilon}_o$ at peak stress and the critical inelastic strain (strain at fault nucleation) ε_n are interpreted from the test results and utilised as reference values (Fig. 2.5). The term 'inelastic strain' by Lockner (1998) should be understood here as 'non-linear component of total strain'.

In the second experimental set-up the specimen is subjected to a strain rate stepping procedure. The specimen is loaded at the above specified loading rates to 60% of the peak strength of the triaxial test and then strain rate stepping is started. The strain rates are varied stepwise from 10% to 0.1% of strain rates in the normal tests resulting in stepwise increasing stresses (Fig. 2.6). For interpretation, the measured stress and strain values are plotted as a function of time (Fig. 2.6) and the values of inelastic strain rate $\acute{\varepsilon}_i$ at selected differential stress levels σ_Δ are recorded. The last regular shaped step is used for interpretation because at that point the inelastic strain is larger and change in stress smaller than at previous steps. Also the possible elastic non-linear component of inelastic strain is smallest here.

2.3.4 Interpretation of results

One aim of the experiments, in the context of this study, is to evaluate the time-to-failure t_f under constant stress loading. The inelastic strain rate sensitivity, $a_{o,}$ at constant temperature and constant confining stress can be solved from equations (2.4)-(2.5) (Lockner, 1998):

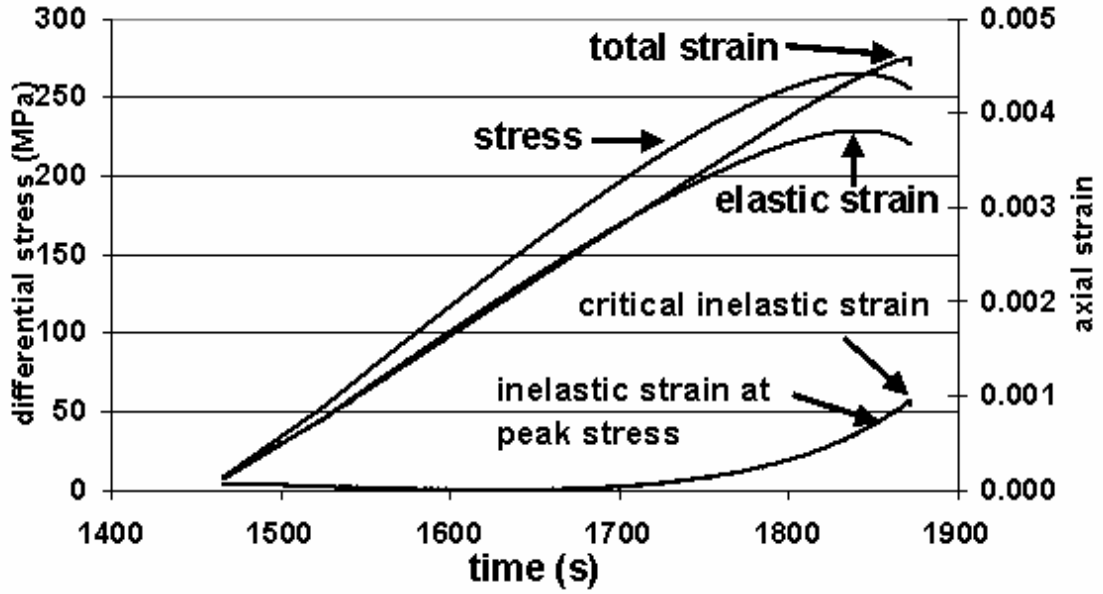

Figure 2.5. Interpretation of a typical standard triaxial test at a confining stress P = 7 MPa for determining reference values.

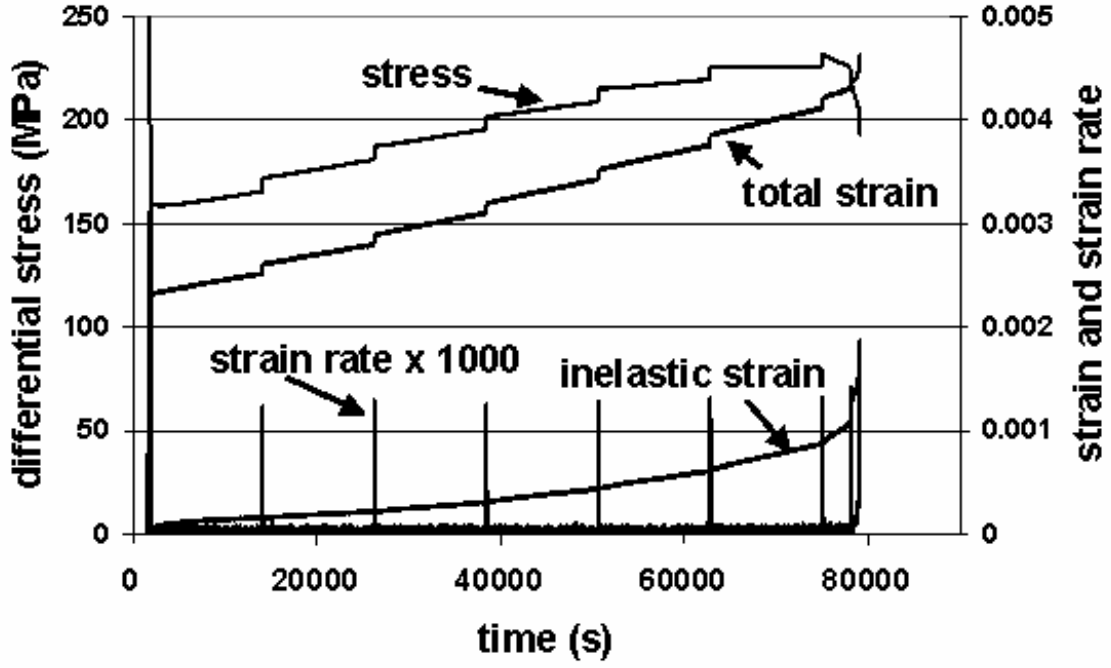

Figure 2.6. Measured axial strain rate, differential axial stress, total strain and calculated inelastic strain in a strain rate stepping test at a confining stress P = 7 MPa.

$$\sigma_{\Delta} = \sigma_{\Delta po} + a_o \sigma_{\Delta po} \ln \frac{\varepsilon_i'}{\varepsilon_o'} \tag{2.4}$$

and

$$a_o = \frac{\sigma_{\Delta} - \sigma_{\Delta po}}{\sigma_{\Delta po} \ln \frac{\varepsilon_i'}{\varepsilon_o'}} \tag{2.5}$$

By rearranging the terms in equation (2.5) the inelastic strain rate is solved:

$$\varepsilon_i' = \varepsilon_o' e^{\frac{\sigma_{\Delta} - \sigma_{\Delta po}}{a_o \sigma_{\Delta po}}} \tag{2.6}$$

The apparent time-to-failure t_f at selected value of differential stress σ_{Δ} is estimated using the critical inelastic strain ε_n from triaxial testing results (Eq. 2.7). The solution forms a straight line on logarithmic time scale (Fig. 2.7).

$$t_f = \frac{\varepsilon_n}{\varepsilon_i'} \tag{2.7}$$

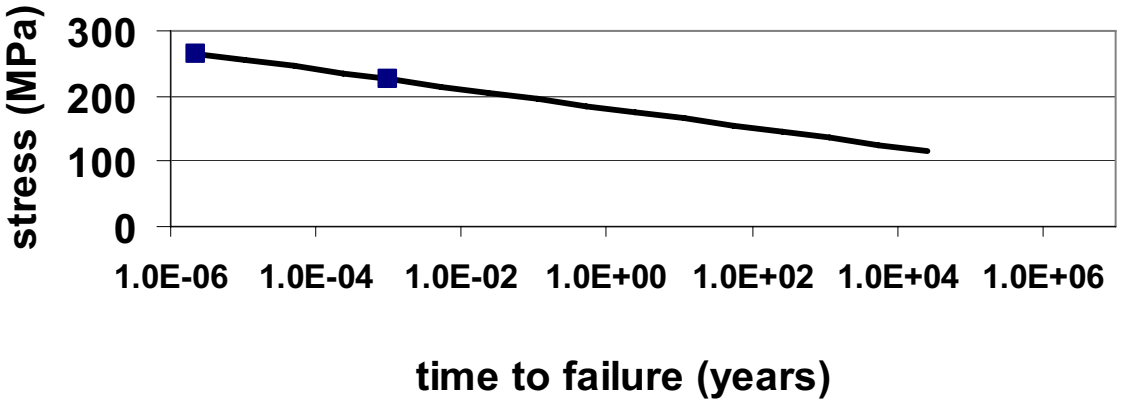

Figure 2.7. Time-to-failure graph derived from Figures 2-5 and 2-6 and with equations 2.4 –2.7).

2.3.5 Discussion

The main goal of these strain stepping experiments was to provide well-documented laboratory test cases for comparing with numerical models. Some of the modelling work is finished and results are presented in this report in Chapter 6.

2.4 Development of an Experimental Method to Determine the Subcritical Crack Growth Parameters A and n of Äspö Diorite

2.4.1 Background and material

Charles (1958) power law is the most commonly used equation to describe subcritical crack growth by stress corrosion. It relates the stress intensity factor K to crack velocity v and may be written as

$$v = A \cdot K^n \tag{2.8}$$

where A is a constant and n is the subcritical crack growth index (also known as stress corrosion index when this mechanism dominates). The stress corrosion index is a measure of the susceptibility of the material to stress corrosion cracking in the particular environment. Atkinson and Meredith (1987) have reported that n is generally in the range 30-60 for tensile failure in rocks. Other laws relating v to K have also been proposed (e.g. Wiederhorn and Boltz, 1970; Lawn, 1975), but the discussion of those is beyond the scope of the study.

For determination of the subcritical crack growth parameters relatively few methods exist, e.g. the Double Torsion Method (Evans, 1972). These are designed for Mode I (tensile) loading only. For the description of the time-dependent behaviour of Mode II (shear) fractures in rock no methodology is known to the authors.

All experiments in this study were carried out at ambient temperature and pressure conditions on Äspö diorite. Mode I fracture toughness K_{IC} = 2.7 MPa $m^{1/2}$ (Chevron-Bend test; ISRM SM, 1988) and Mode II fracture toughness K_{IIC} = 4.5 MPa $m^{1/2}$ (Punch-Through Shear test; Backers, 2005, Backers et al., 2002). All specimens tested were saturated with de-ionised water.

2.4.2 Determination of subcritical crack growth parameters

In this development work a fracture statistics method is employed for determining subcritical crack growth parameters. It uses Weibull statistics to predict time dependent failure (Weibull, 1951). Wilkins (1980, 1987) used it for Lac du Bonnet granite and others. Wilkins carried out tensile tests in order to obtain data in the form of $\ln \sigma_H$ versus $\ln t_f$ (time-to-failure). The homologous stress ratio σ_H is the ratio of applied stress σ_A to instantaneous breaking stress σ_i of the material. t_f and σ_i cannot be measured on the same samples; they were estimated from the sample population by using the Weibull distribution, given by

$$P_i = 1 - \exp\left[-\sigma_i/\sigma_w\right]^f \tag{2.9}$$

where P_i is the cumulative probability of a given instantaneous fracture stress, while σ_w and f are the distribution constants.

In practice, the method consists of two sets of tests on the same population of samples. Firstly, a series of rapid loading tests is carried out in order to determine the

Weibull distribution parameters. Subsequently, a series of constant load tests is performed on a second set of specimens of identical volume. These tests determine the time-to-failure t_f at a specific stress. The determined t_f values are ranked and paired with the measured values from the rapid loading tests. This allows a t_f versus σ_H diagram to be constructed, where the slope corresponds to the stress corrosion index n. The test data and K_{IC} can be used to evaluate the factor A in the Charles power law (equation (2.8).

2.4.2.1 Experimental set-up and procedure

The experiments were carried out by using a stiff and servo-controlled MTS loading machine. The maximum force capacity of the rig is 4600 kN. High accuracy load cells of range 0-25 kN and 0-1000 kN were used.

The experimental and specimen design of the Mode I (notched three-point bending) and the Mode II (Punch-Through Shear, PTS-) loading set-ups are given in Fig. 2.8. The experiments to achieve the Weibull distribution parameters are run at a constant displacement rate until failure. The experiments to determine the time-to-failure data are run at a constant load that corresponds to a certain failure probability.

2.4.2.2 Mode I loading results

Nineteen constant displacement rate experiments have been performed at tensile loading. The data is ranked and the cumulative probability is plotted against the failure stress σ_{Ti} in the ln- space (Fig. 2.9). The plot determines a linear regression with slope f = 7.82 and the axis intercept is -f ln σ_{TW} = -19.61, and σ_{TW} = 12.25 and hence

$$P_i = 1 - \exp - [\sigma_{Ti} / 12.25]^{7.82} \tag{2.10}$$

The applied F_A in the constant load series is 7.0 kN, corresponding to a probability for failure of about 0.259. Therefore, about 25.9 % of the tested specimens should fail at zero time. Of the total of 26 time-to-failure tests seven samples failed instantaneously, corresponding to 26.9 %, which is in close agreement with the predicted instantaneous failure rate from the Weibull probability.

The data is ranked and paired with the corresponding homologous ratio, $\sigma_{TH} = \sigma_{TA}/\sigma_{Ti}$, where σ_{TA} = 10.5 MPa and σ_{Ti} is derived from equation (2.10). The paired data is then plotted into the ln- space (Fig. 2.10) yielding a linear regression with slope m = -0.021 and axis-intercept b = 0.017 and m = -1/n. Hence, the subcritical crack growth exponent n = 48.

The scaling factor A can be calculated following the procedure of Wilkins (1980) by

$$A = \frac{2 \cdot K_c^{(2-n)} \cdot \left[1 - \sigma_{Hx}^{(2-n)}\right]}{(2-n) \cdot t_{fx} \cdot \sigma_A^2} \tag{2.11}$$

where σ_{Hx} and t_{fx} are corresponding values taken from the plot of ln σ_H vs. ln t_f, and σ_A is the applied stress corresponding to F_A.

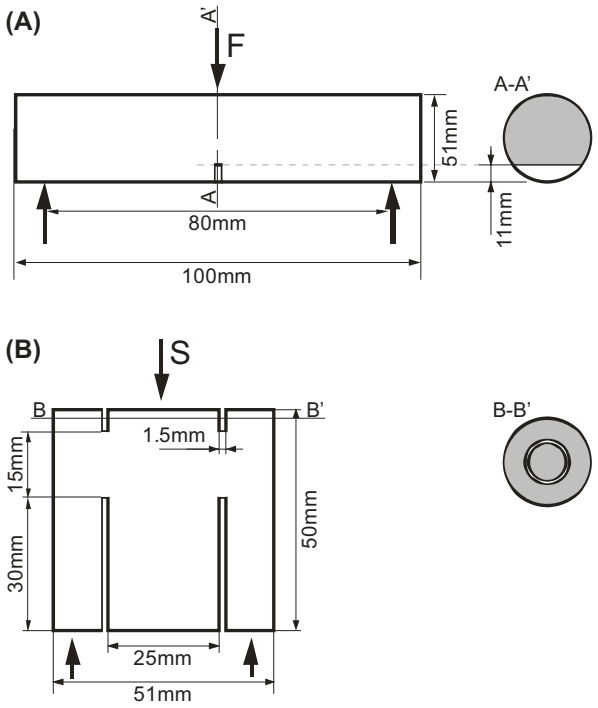

Figure 2.8. Experimental set-up for (A) Mode I and (B) Mode II loading (Punch-Through Shear test; Backers, 2005). F: applied point load; S: applied load yielding a shear stress in the notch plane.

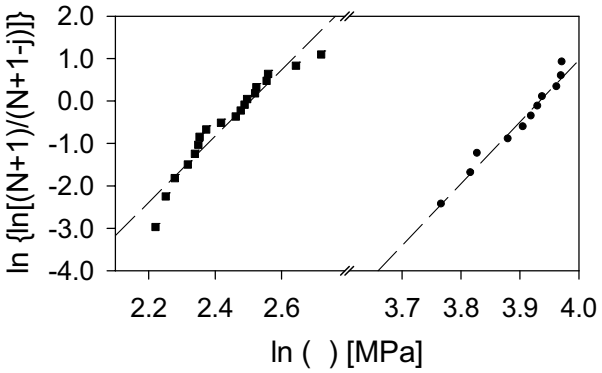

Figure 2.9. Weibull diagram of tensile (square) and shear (circle) testing data. The linear regression to the data delivers the adjustables to the probability function.

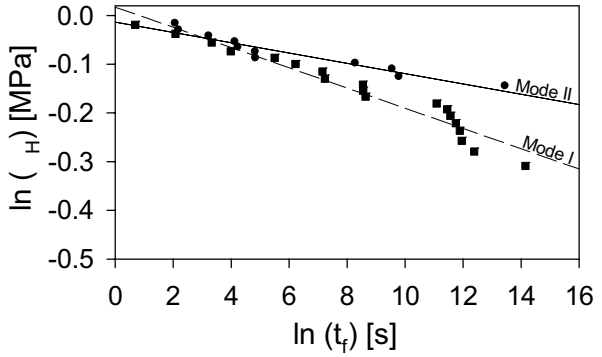

Figure 2.10. Homologous ratio as a function of the ranked time-to-failure data. Mode I: squares and dashed line, Mode II: circles and solid regression.

Calculated from eleven data pairs $A = 1.2 \cdot 10^{-24} \pm 8.3 \cdot 10^{-25}$. The crack velocity vs. K_I for the diorite is plotted in Fig. 2.11. The lowest crack velocity is estimated from the $\sigma_{TH} = 0.7343$ for the slowest experiment performed; from this the K- axis intercept is $K_I = \sigma_{TH} \cdot K_{IC} = 2.01$ MPa $m^{1/2}$.

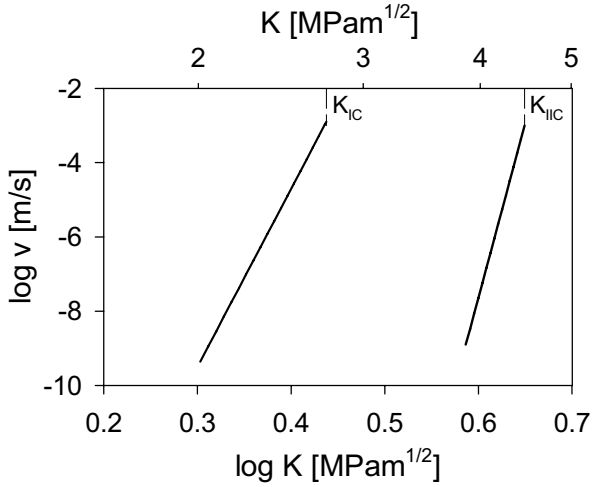

Figure 2.11. Crack velocity v vs. stress intensity factor K plot for Mode I and Mode II subcritical crack growth.

2.4.2.3 Mode II loading results

In the case of the data sample from the PTS tests constant displacement rate experiments the number of experiments is 11. The data is ranked and the cumulative probability is plotted against the failure stress (Fig. 2.9). The load is recalculated to the shear stress, σ_{Si}, acting in the fracture plane. The data yields f = 14.57, -f ln σ_{Sw} = -57.30, $\sigma_{SW} = 51.10$. and, hence, the probability function is

$$P_i = 1 - \exp - [\sigma_{Si} / 51.10]^{14.57} \qquad (2.12)$$

The applied shear load S_A in the constant load series is 56.0 kN ($\sigma_{SA} = 47.5$ MPa, K_{II} = 4.28 MPa $m^{1/2}$), corresponding to a probability for failure of 0.291. Five samples of the constant-load population failed instantaneously, corresponding to 31.3 %, being in close agreement with the predicted instantaneous failure rate.

The constant load data is ranked and paired with the corresponding homologous ratio, $\sigma_{SH} = \sigma_{SA}/\sigma_{Si}$, where $\sigma_{SA} = 47.5$ MPa and σ_{Si} is derived from equation (2.12). A regression to the plotted data (Fig. 2.10) yields slope m = -0.0106 and axis-intercept b = -0.0135. Hence, the subcritical crack growth exponent *n* = 94.

Parameter *A* is calculated to $9.1 \cdot 10^{-65} \pm 8.0 \cdot 10^{-65}$. The crack velocity vs. K_{II} for the diorite is plotted in Fig. 2.11. The K- axis intercept as derived from the slowest experiment is $K_{II} = \sigma_{SH} \cdot K_{IIC} = 3.86$ MPa $m^{1/2}$.

2.4.3 Discussion

K_{IIC}= 5.1 MPa $m^{1/2}$ is reported for dry samples of Äspö diorite (Backers, 2005). The saturated specimens in this series show a fracture toughness about 12 % lower, K_{IIC} = 4.5 MPa $m^{1/2}$. Although the specimens are not manufactured from the same sample, the indication is given that K_{IIC} is lowered by the presence of a fluid. This is in perfect analogy to the behaviour of the Mode I fracture toughness in this study. Backers (2005) reports K_{IC} = 3.8 for Äspö diorite. The fracture toughness determined for saturated samples in this report is about 30 % lower.

It is reported in the literature that average n values for tensile stress corrosion cracking is in the range of n = 30-60 (Atkinson and Meredith, 1987). This study yields n = 48 in perfect agreement with the reported range. The shear stress corrosion cracking index is n = 94. This is higher than the average range reported for tensile boundary conditions, but still within a sensible regime.

Figure 2.11 presents the crack velocity vs. stress intensity factor data for Mode I and Mode II loading conditions. To achieve a certain fracture propagation velocity, the necessary stress intensity under Mode I loading is well below that under Mode II conditions for the data of the present study. This was to be expected from the ratio of K_{IC} to K_{IIC}, i.e. K_{IC}/K_{IIC} = 0.6

Once the above developed methods have reached a mature stage in laboratory testing, they provide a powerful, easy to apply and economic way to estimate the subcritical fracture growth parameters of rocks under laboratory conditions.

2.5 Conclusions

The different laboratory tests described in this chapter have contributed to building up a database for the development of constitutive models that can capture the chemical and time dependent features observed in intact crystalline rock during fracturing and failure. From the results of the uniaxial compression tests it can be shown that there is an effect of water salinity on the mechanical properties of the specimens. In this study, the effect of weak saline water on the Young's modulus and the compressive strength increased with the immersion time. The results also indicate an effect of salinity on the post-failure behaviour of brittle rocks: with high saline water, the specimens act in a more ductile manner than those with low salinity water.

The time dependent behaviour of Äspö diorite is retrieved from the Strain Rate Stepping Test, which offers a promising alternative to the other creep testing methods for heterogeneous hard rock samples. The time-to-failure calculations are only understood as indicative at this stage of research. The present assumption of constant confining pressure and temperature in the interpretation limits the practical applicability of the results. Also, for long time-periods other factors, such as chemical effects, are likely to limit the time span that can be predicted.

The third test campaign aimed at developing experimental testing methods for the determination of the subcritical fracture growth parameters under Mode I and II conditions. The results show that the methods proposed can determine these parameters. In this study the constant load experiments on the PTS set-up have shown that time-dependent fracturing behaviour occurs under Mode II loading in laboratory conditions at ambient pressure conditions. This has never been shown before.

Nevertheless, further development work has to be conducted to verify the methods reported here before challenging broader application. The remaining aspects of the experimental procedures are the influence of different water contents, fluid types and temperatures. The number of experiments should be increased to guarantee their statistical representativity.

References

Atkinson, B. K., and Meredith, P. G., *Experimental fracture mechanics data for rocks and minerals*, in Fracture Mechanics of Rock. B. K. Atkinson (ed.), Academic Press, London 1987. pp. 477-525.

Backers, T., *Fracture Toughness Determination and Micromechanics of Rock under Mode I and Mode II Loading*. Doctoral Thesis, University of Potsdam 2005.

Backers, T., Stephansson, O., and Rybacki, E.,. *Rock Fracture Toughness Testing in Mode II – Punch-Through Shear Test*. Int. J. Rock Mech. Min. Sci., 2002(39), 755-769.

Charles, R. J., *Static fatigue of glass*. J. Appl. Phys., 1958(29),1549-1560.

Eloranta, P., Hakala, M., *Laboratory testing of Hästholmen equigranular rapakivi granite in borehole HH-KR6*. Report Posiva Oy, Working Report 99-47 1999. p. 154.

EN 1936, *Natural stone test methods-Determination of real density and apparent density, and of total and open porosity*. European standard. CEN 1999. p. 9.

Evans, A. G., *A method of evaluating the time-dependent failure characteristics of brittle materials - and its application to polycrystalline alumina*. J. Mater. Sci., 1972(7), 1137-1146.

Fairhurst, C. E. and Hudson, J. A., *International Society of Rock Mechanics Commission on Testing Methods, Draft ISRM suggested method for the complete stress-strain curve for intact rock in uniaxial compression*.Int. J. Rock. Mech. Min. Sci. , 1999(36), 279-289.

Feng, X-T., Chen, S., and Li, S., *Effects of water chemistry on microcracking and compressive strength of granite.* Int. J. Rock Mech. Min. Sci., 2001(38), 557-568.

Feucht, L. J. and Logan, J., *Effects of chemically active solutions on shearing behaviour of a sandstone.* Tectonophysics, 1990(175), 159-176.

Hakala, M., Heikkilä, E., *Summary report – Development of laboratory tests and the stress- strain behaviour of Olkiluoto mica gneiss*. Posiva Oy, Helsinki 1997.

ISRM SM., *Suggested methods for determining tensile strength of rock material*. Int. J. Rock Mech. Min. Sci. Geomech. Abstr., 1978(15), 99-103.

ISRM SM., *Suggested methods for determining strength of rock materials in triaxial compression: revised version*. Int. J. Rock Mech. Min. Sci. Geomech. Abstr., 1983(20), 285-290.

ISRM SM., *Suggested methods for determining the fracture toughness of rock*. Int. J. Rock Mech. Min. Sci. Geomech. Abstr., 1988(25), 71-96.

ISRM SM., *Draft ISRM suggested method for the complete stress-strain curve for intact rock in uniaxial compression*. Int. J. Rock Mech. & Min. Sci., 1999(36), 279-289

Jacobsson, L., Bäckström, A., *Uniaxial compression tests of intact rock specimens at dry condition and at saturation by three different liquids: distilled, saline and formation water*. Swedish Nuclear Fuel and Waste Management Company (SKB). IPR-05-33 2005. p.99.

Karfakis, M. G., and Akram, M., *Effecs of chemical solutions on rock fracturing.* Int. J. Rock. Mech. and Min. Sci. & Geomech. Abstr.; 1993; 30(7), 1253-1259.
Lawn, B. R., *An atomistic model for kinetic crack growth in brittle solids*. J. Mat. Sci., 1975(10), 469-480.
Lockner, D., *Generalized law for brittle deformation of Westerley granite*. Journal of Geophysical Research, 1998;103 (B3), 5107-5123.
Malmström, M., Banwart, S., Duro, L., Wersin, P., and Bruno, J., *Biotite and chlorite weathering at 25^o C.* Swedish Nuclear Fuel and Waste Management Company (SKB).TR-95-01 1995. p. 128.
Martin, C. D., and Chandler, N. A., *The progressive fracture of Lac du Bonnet granite*. Int. J. Rock. Mech. Min. Sci. & Geomech. Abstr., 1994; 31(6), 643-659.
Rausell-Colom, J. A., Sweatman, T. R., Wells, C. B., and Norrish, K., *Studies in the artificial weathering of mica*. Experimental Pedology. Hallsworth-Crawford (Editor) Butterworths, London 1994. pp. 40-72.
Wiederhorn, S.M., and Bolz, L. H.,. *Stress corrosion and static fatigue of glass*. J. Am. Ceram. Sci., 1970(153), 543-548.
Weibull, W. A., *Statistical distribution function of wide applicability*. J. Appl. Mech., 1951(18), p. 293.
Wilkins, B. J. S., *Slow crack growth and delayed failure of granite*. Int. J. Rock Mech. Min. Sci. Geomech. Abstr., 1980(17), 365-369.
Wilkins, B. J. S., *The long term strength of plutonic rock*. Int. J. Rock Mech. Min. Sci. Geomech. Abstr., 1987 (24), 379-380.

3. Method and results of using an EPCA approach

Xia-Ting Feng and Peng-Zhi Pan
Institute of Rock and Soil Mechanics, Chinese Academy of Sciences, Wuhan , China

3.1 Introduction

The main purpose of Task B Phase 2a is to model the failure of intact rock and intact rock with a specified fracture in uniaxial compression by a variety of models used by the different research teams in order to see which models have output features in common and which model outputs are highly 'model specific'. In other words, what is common in the different numerical modelling methods and what is not.

The trends and the ability of the different models to capture the observed features will be compared between different research teams. The most important thing is to establish which models can simulate Class II and the other features and which can't.

The intention of Phase 2b is to conduct a numerical exploration and demonstration of whether the full DIANE features of real rock in uniaxial compression can be simulated by the models, i.e. the discontinuous, inhomogeneous, anisotropic and non-elastic nature of the rock. It also needs to explore time dependency as a specific aspect of the non-elastic behaviour.

3.2. A Brief Introduction to EPCA model

All the simulations are conducted by using an Elasto-Plastic Cellular Automata (EPCA) approach (Feng et al., 2006). With this approach, firstly the rock specimen is discretized into a system composed of cell elements. Then a heterogeneous material behaviour is adopted with homogeneous index m, and the elemental seed parameters for the heterogeneous mechanical properties of rock, such as Young's modulus, Poisson's ratio, cohesive strength etc. The mechanical parameters of rocks are assumed to conform to Weibull's distribution whose probability density function can be expressed as (Weibull, 1951),

$$p(x)=\begin{cases}\dfrac{m}{x_0}\left(\dfrac{x}{x_0}\right)^{m-1}\exp\left[-\left(\dfrac{x}{x_0}\right)^{m}\right], x\geq 0\\ 0, x<0\end{cases}. \tag{3.1}$$

where x is the mechanical parameter of the element; the scale parameter x_0 is related to the average of the elemental mechanical parameter, and the parameter, m, defines the shape of the distribution function.

Depending on the initial and boundary conditions, certain loading control methods such as constant strain rate or linear combination of stress and strain (Okubo and Nishimatsu, 1985) etc., are adopted to simulate the loading process of the rock specimen in order to obtain the complete stress-strain curves of the rock failure process.

In each loading step, the cell state is updated by the cellular automata rule of updating (Feng et al., 2006) to obtain the displacement field and stress field. In an EPCA model, the cell state can be defined as,

$$\phi_i^{(k)} = \left\{\{u, v\}, \{t, E, \mu\}, \{f_x, f_y\}, \{\varepsilon_p\}\right\}_i^{(k)}. \tag{3.2}$$

where, u, v are the displacements in x and y directions, respectively. t, E, μ are the thickness, Young's modulus and Poisson's ratio of the cell element, respectively. f_x, f_y are the cell nodal forces in x and y directions, respectively. ε_p is the equivalent plastic strain of a cell element. The cell element obeys the elasto-plastic loading and unloading rule (Xu, 1988).

The calculated stresses are substituted into the modified Mohr-Coulomb criterion to check whether or not cell element yield occurs. If the strength criterion is not satisfied, the external force is increased further. Otherwise, the cell element yields and the corresponding plastic strain produced according to the elasto-brittle-plastic constitutive theory (Fig. 3.1a) (Dems and Mroz 1985, Shen et al., 1995, Zhen et al., 2005).

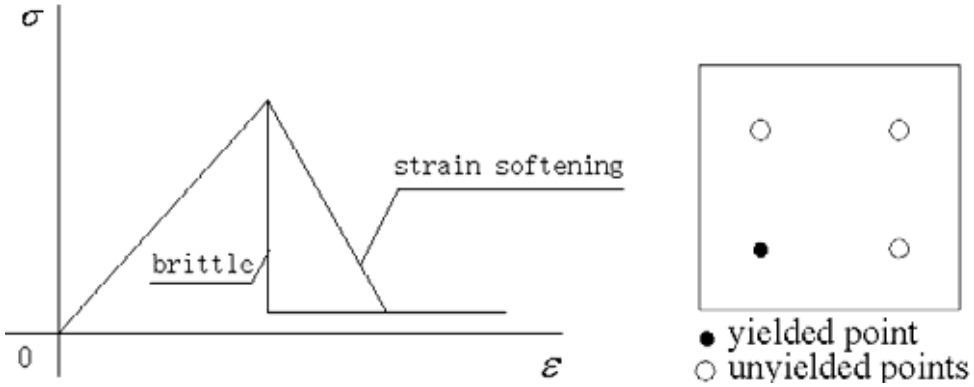

Figure 3.1: a) constitutive relation of cell element: b) The state of Gauss point.

A symbol α, which is named 'softening coefficient', is introduced to describe the post-peak schemes. Then we have,

$$s^{(f)} = (1-\alpha)s^{(r)} \tag{3.3}$$

where, $s^{(f)}$ is the partial stress tensor after stress dropping.

$$0 < \alpha \le 1-\beta. \tag{3.4}$$

From equation (3.4), we can conclude that $\alpha = 1-\beta$ corresponds to the brittle case, while $0 < \alpha < 1-\beta$ corresponds to the strain softening case.

The stress and deformation distributions throughout the domain are then adjusted instantaneously after each rupture to reach the equilibrium state. In the process of stress adjustment, the stress of some cell elements may satisfy the critical value and further

ruptures are caused. The process is repeated until no cell elements are left to yield. On the basis of equilibrium of stress adjustment, further load will be subjected to the system until the macro failure of rock specimen occurs. Thus the EPCA model links the mesoscopic mechanical model to macrostructure failure, which has been regarded as one of the most challenging tasks in the area of brittle failure.

In the EPCA model, since the isoparametric cell element is chosen as the cell element, according to the state of the Gauss point (Fig. 3.1b), each AE (Acoustic Emission) event corresponds to the yield Gauss points of a cell element, and the AE energy release of an element is assumed to be the reduction of elastic strain energy during yield.

In the EPCA model, three control methods can be considered, i.e., stress loading control method, constant strain rate control method and the linear combination of stress and strain control method. However, in order to obtain a Class II curve for rock, only linear combination of stress and strain can be used as the loading control method in the EPCA model (Pan et al., 2006). The governing equation of linear combination of stress and strain can be expressed as (Okubo and Nishimatsu, 1985),

$$\varepsilon - \frac{\sigma}{E'} = C \cdot t \tag{3.5}$$

where E', C are fixed chosen modulus value and the loading rate, respectively.

By using this method, not only Class I but also Class II curves can be obtained (Fig. 3.2).

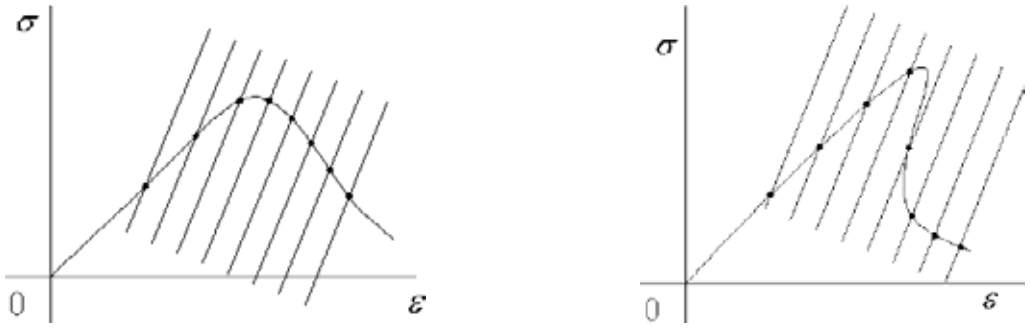

Figure 3. 2: Schematic stress-strain curve of Class I and Class II rock for linear combination of stress and strain loading method.

3.3. Numerical simulations of core tests for Phase 2

3.3.1. Dry laboratory rock under uniaxial compression using constant strain rate control method

The uniaxial compressive numerical test is simplified as a plane stress model and a vertical section is considered. The numerical model is built according to the laboratory tests for dry rock samples conducted (see Chapter 2), i.e. the diameter D=51 mm and the height H=135 mm. Constant strain rate loading control is chosen as the loading control method, considering the same homogeneous index $m = 6.0$, but different elemental seeds i.e., 10 and 15, respectively. Associated flow rule is adopted and the

Mohr-Coulomb criterion is used as the yield criterion. Other mechanical and loading parameters are shown in Table 3.1. In this table the Young's Modulus, Poission's ratio and strength are the measured properties of Äspö diorite samples used in laboratory tests (see Chapter 2), and the other parameters are assumed according to the need of the EPCA model.

Table 3. 1: Mechanical and loading parameters

Parameters	Value	Parameters	Value
Young's Modulus	70000 MPa	Residual coefficient	0.1
Poisson's ratio	0.29	Loading speed	0.005 mm/step
Compressive strength(mean value)	295 MPa	CA iterative precision	1e-7
Tolerance	1%	Softening coefficient	0.9
Homogeneous index	6.0	Random seed	10,15

Fig. 3.3 shows the failure process of a dry rock sample with homogeneous index $m = 6.0$ and elemental seed 15. Due to the softening coefficient, 0.9, corresponding to the brittle case, sudden failure occurs when the rock specimen reaches its peak strength. At the same time, a sudden increment of AE occurs as can be seen from Fig. 3.4 and Fig. 3.5.

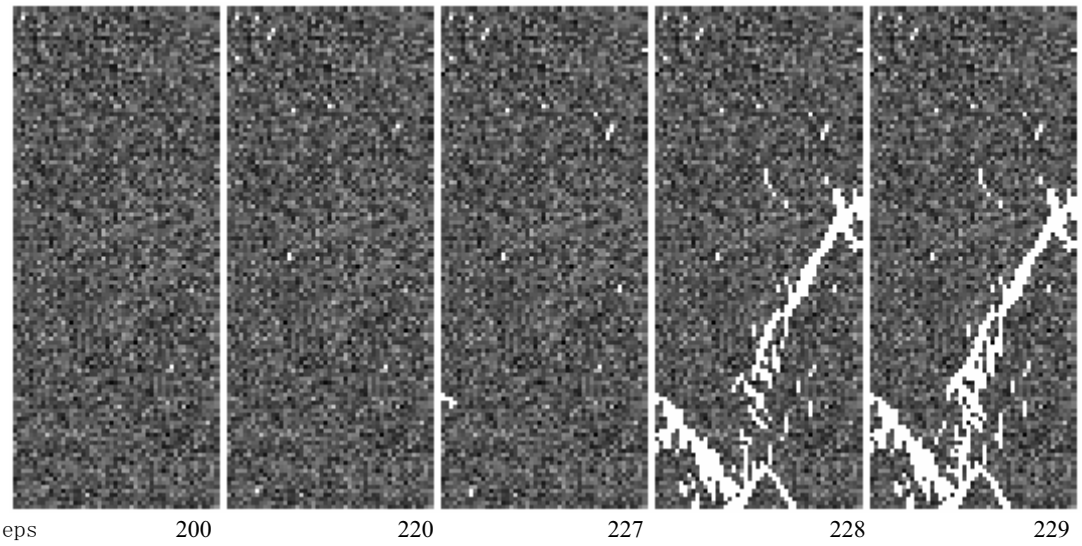

Figure 3.3: Failure process of dry rock sample with $m = 6.0$ and elemental seed 15.

From Fig. 3.6, in the pre-peak strength, the rate of increase of axial strain is larger than that of radial or lateral strain. But after the peak strength, with the rapid dropping of axial stress due to the formation of the shearing band, a sudden increment of radial strain and volumetric strain occurs.

Fig. 3.7 shows the final modes of rock specimen with homogeneous index $m = 6.0$ and different elemental spatial distribution i.e., random seed =10 and 15, respectively. It can be concluded that different elemental spatial distributions will lead to different failure modes, which explains why the failure modes of rock specimens from the same rock mass are different in experiment.

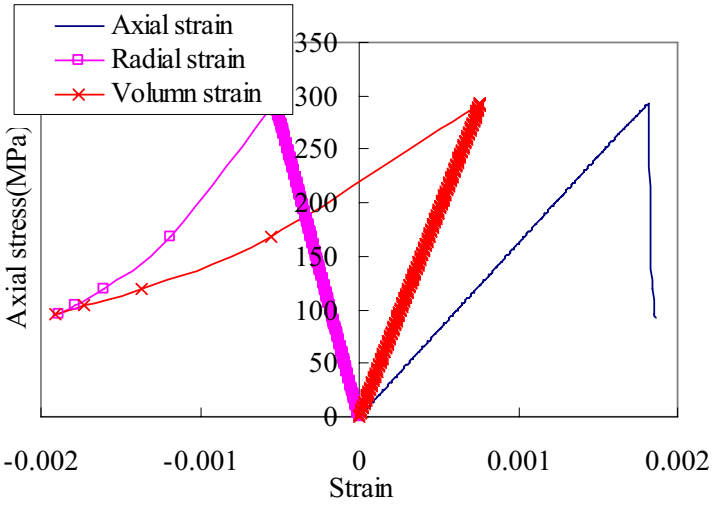

Figure 3.4: Axial strain, radial strain and volumetric strain-stress curves with $m = 6.0$ *and elemental seed 15.*

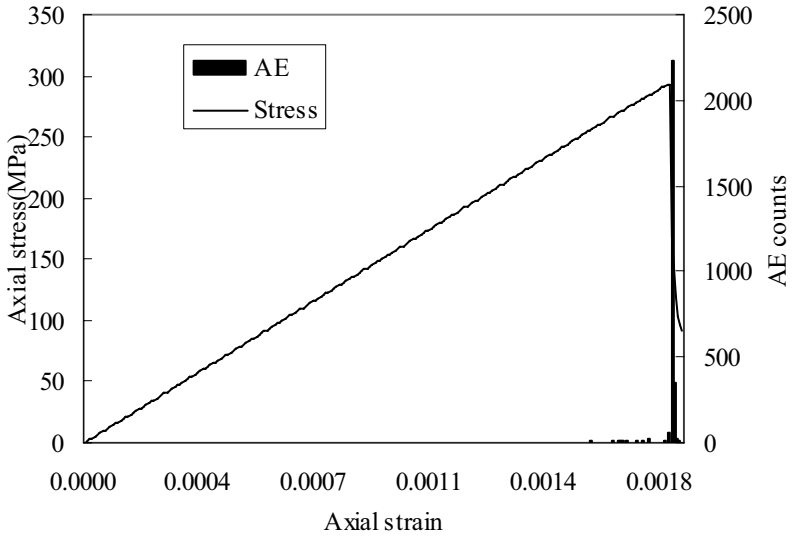

Figure 3.5: Complete stress-strain and AE curves with $m = 6.0$ *and elemental seed 15.*

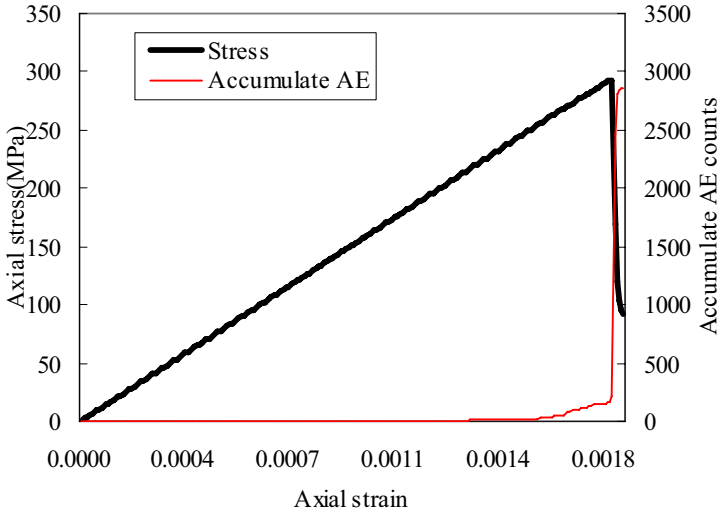

Figure 3.6: Complete stress-strain and accumulative AE curves with $m = 6.0$ *and elemental seed 15.*

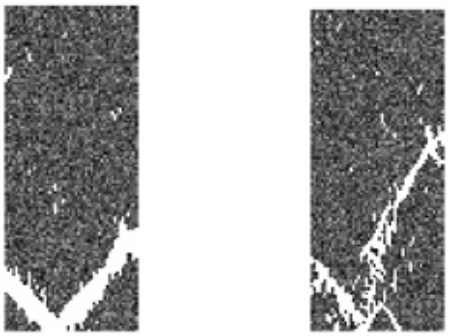

(a) seed=10 *(b) seed=15*

Figure 3.7 Final failure modes of dry rock samples with $m = 6.0$ but different elemental seeds.

3.3.2. Saline laboratory rock under uniaxial compression using linear combination of stress and strain control method

The uniaxial compressive numerical test is simplified as a plane stress model and a vertical section is considered. The numerical model is built according to the laboratory tests for saline laboratory rock samples conducted by Jacobsson and Bäckström (2005), i.e. the diameter D=51 mm and the height H=127 mm. The linear combination of stress and strain is used as the loading control method, considering the same homogeneous index $m = 6.0$, but different elemental spatial distributions i.e., random seeds are 10 and 15, respectively. With $E / E' = 0.5$, the mechanical and loading parameters are shown in Table 3.2. In this table, similarly the Young's Modulus, Poission's ratio and strength are obtained from the measured data (See Chapter 2) and other parameters are assumed according to needs of the EPCA model. The Drucker-Prager criterion is chosen as the yield criterion. The boundary conditions used for obtaining Figs. 3.9 and 3.10 are that the lower end of the model is fixed and the upper end is loaded using the linear combination of stress and strain control method following equation (3.5)

Table 3.2: Mechanical and loading parameters

Parameters	Value	Parameters	Value
Young's Modulus	68000 MPa	Residual coefficient	0.1
Poisson's ratio	0.3	CA iterative precision	1e-7
Compressive strength(mean value)	234 MPa	Softening coefficient	0.05
Tolerance	1%	Random seed	10, 15
Homogeneous index	6.0	C	3.9e-5
E / E'	0.5		

Figure 3.8 shows the final failure mode of saline rock with different elemental spatial distributions but the same homogeneous index. Due to the difference in elemental spatial distribution, the final failure modes of the two saline rocks are different. However, no significant difference in the macro-strength can be seen in the complete stress-strain curves (Fig. 3.9). Under the selected loading and mechanical parameters, both rocks present Class II behaviour. From the acoustic emission curves (Figs. 3.10 and 3.11), it can be concluded that, as the strain snaps back, there are still many AE counts produced, which means that the fractures still propagate.

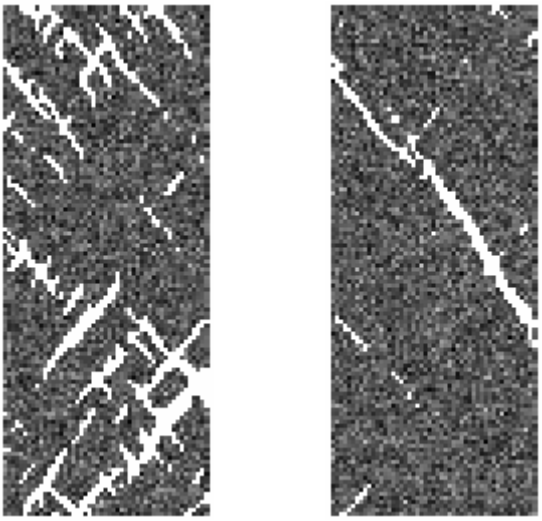

(a) Seed=10 *(b) seed=15*

Figure 3.8: Failure modes with different elemental seeds.

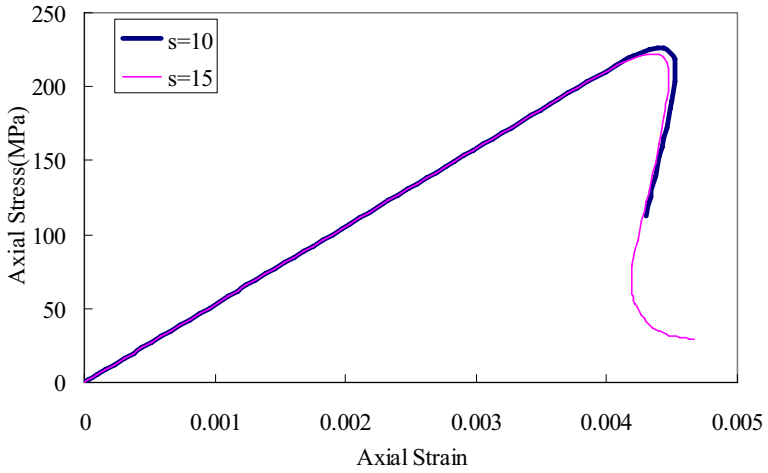

Figure 3.9: Complete stress-strain curves with different seeds.

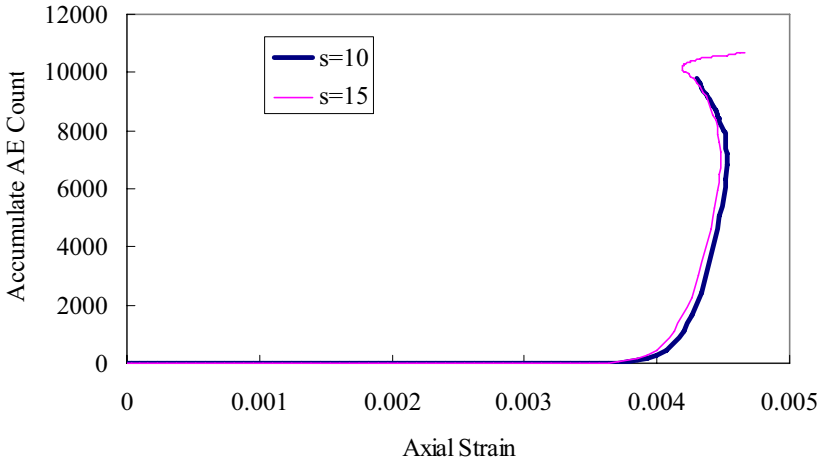

Figure 3.10: Accumulate AE-strain curves with different seeds.

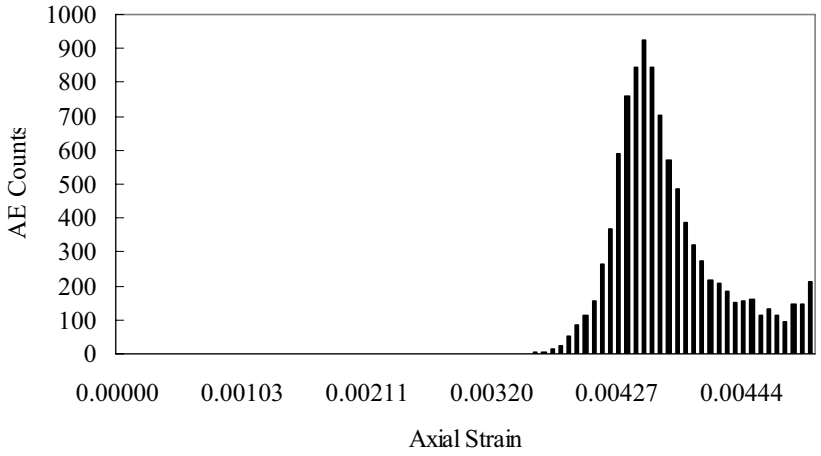

(a) Seed = 10

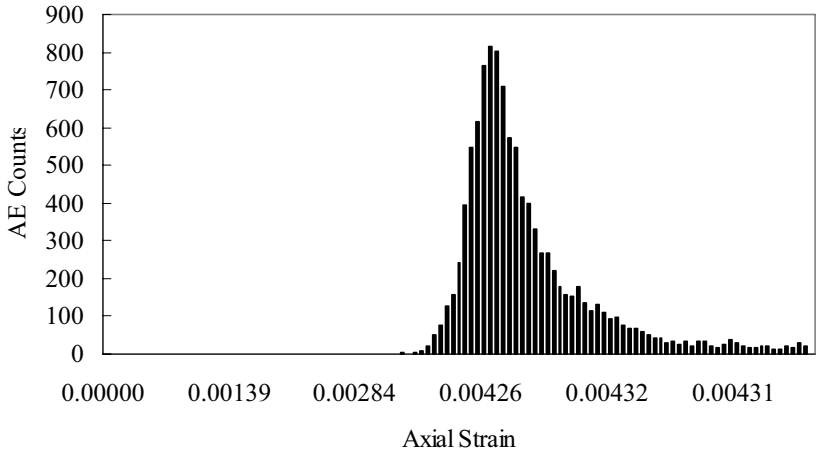

(b) Seed=15

Figure 3.11: AE-strain curves with different seeds.

3.3.3. Pre-fabricated crack propagation simulation

In this section, in order to show the ability to simulate discontinuous features of real rock under uniaxial compression, two simulations with either a single pre-fabricated crack or double pre-fabricated cracks (Fig. 3.12) are conducted.

a) Single crack case

The uniaxial compressive numerical test is simplified as a plane stress model and a vertical section is considered. The numerical model is built according to the laboratory tests for dry samples conducted in the laboratory (see Chapter 2), i.e. the diameter D=51 mm and the height H=125 mm. In the centre of the rock specimen, there is a single crack with the length of 15 mm and the dip angle of 45 degrees. The pre-fabricated crack is represented by weak elements, whose Young's modulus is 0.1 MPa. Constant strain rate loading control method is chosen as the loading control method, considering homogeneous index $m = 6.0$, and random seed =15. The Mohr-Coulomb criterion with a tension cut-off is adopted as the criterion. The mechanical and loading parameters are

shown in Table 3.3. In this model, the crack is assumed and the Young's Modulus of the crack is 0.1MPa.

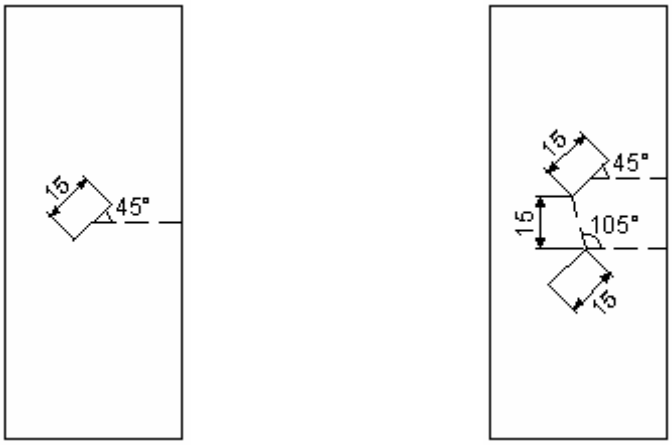

(a) Single crack *(b) double cracks*

Figure 3.12: Pre-fabricated crack models.

Table 3.3: Mechanical and loading parameters of rock matrix. The Young's Modulus, Poission's ratio and strength are measured data and other parameters are assumed according to the need of the EPCA model.

Parameters	Value	Parameters	Value
Young's Modulus	68000 MPa	Residual coefficient	0.1
Poisson's ratio	0.3	Loading speed	0.001 mm/step
Tensile strength (mean value)	20 MPa	CA iterative precision	1e-7
Tolerance	1%	Softening coefficient	0.9
Homogeneous index	6.0	Random seed	15
Compressive strength (mean value)	295 MPa		

As shown in Fig. 3.13, microcracks initiate around the tips of the pre-fabricated crack and then a macrocrack forms. The macroscopic cracks at the two tips of the pre-fabricated crack propagate almost parallel to the loading direction but in zigzag paths in the case of heterogeneous rock. With the increase of axial stress, more microcracks in other parts of the sample initiate and finally they propagate almost parallel to the loading direction

Fig. 3.14 shows the relation of axial strain, radial strain and volumetric strain-stress. From Fig.s 3.15 and 3.16, corresponding to the microcrack propagation, there is a certain number of AE counts produced.

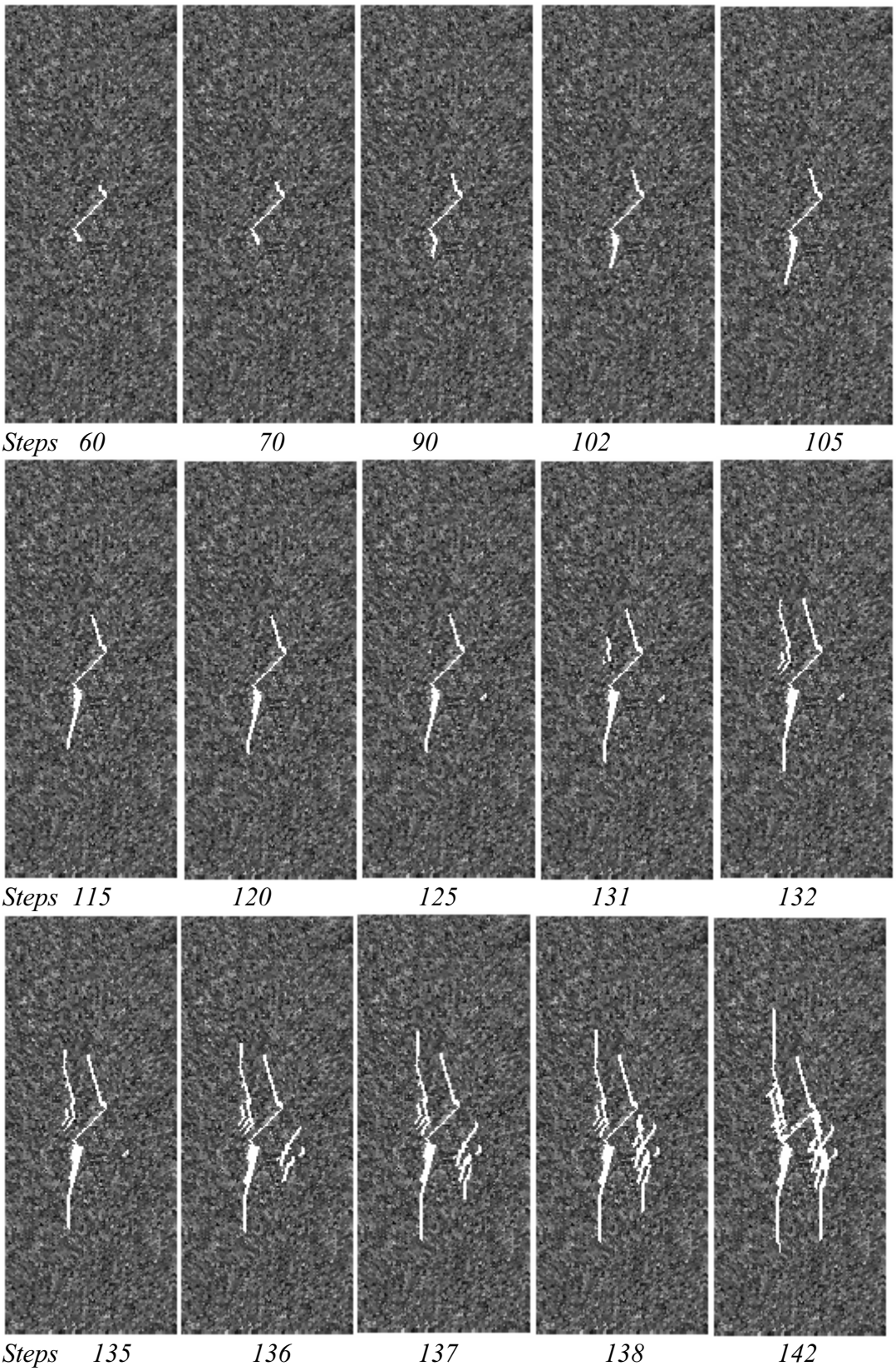

Figure 3.13: Crack propagation process of dry rock model.

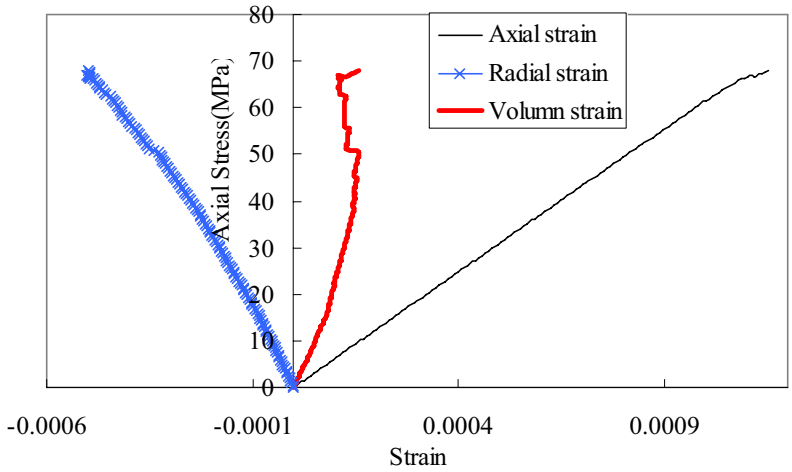

Figure 3.14: Axial, radial and volumetric strain-stress curves.

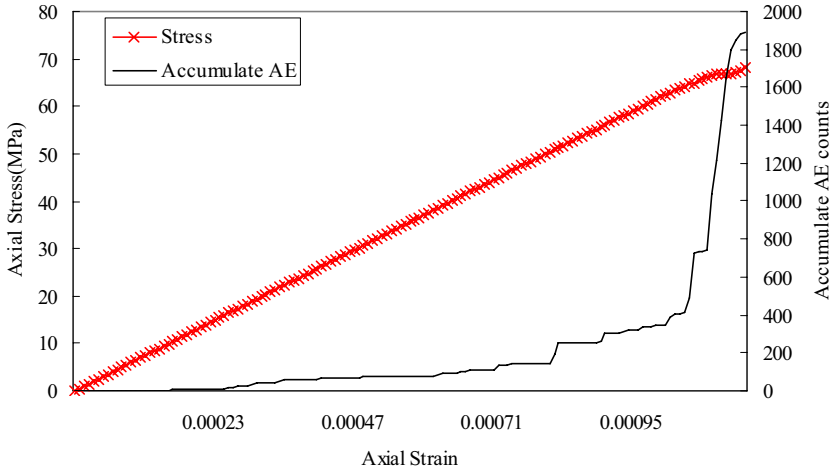

Figure 3.15: Stress and accumulate AE curves.

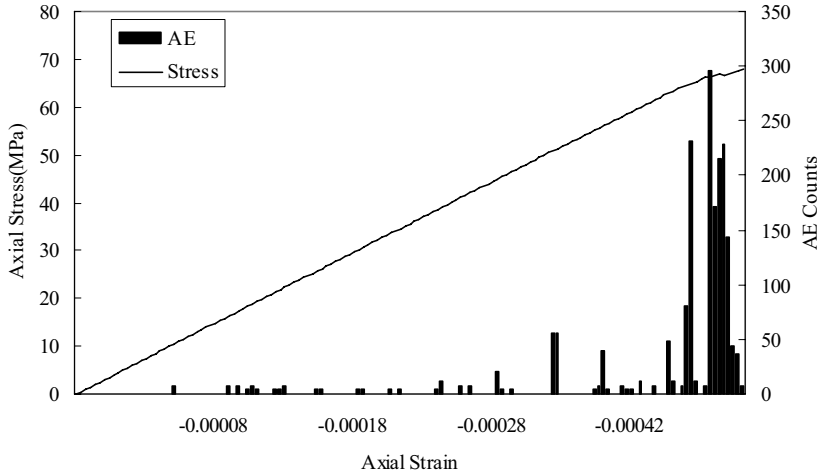

Figure 3.16: Stress and AE curves.

b) Double cracks case

The uniaxial compressive numerical test is simplified as a plane stress model and a vertical section is considered. The numerical model is built according to the laboratory tests for dry samples conducted in the laboratory (see Chapter 2), i.e. the diameter $D = 51mm$ and the height $H = 125mm$. In the rock specimen, there are two pre-fabricated cracks. The cracks are assumed and weak elements are used to represent the cracks with Young's Modulus of 0.1MPa. Constant strain rate loading control method is chosen as the loading control method, considering homogeneous index $m = 6.0$, and random seed =15. Mohr-Coulomb criterion with tension cut-off is adopted as the criterion. The mechanical and loading parameters are shown in Table 3.4.

Table 3.4: Mechanical and loading parameters of rock matrix (The Young's Modulus, Poission's ratio and strength are measured (see Chapter 2) and other parameters are assumed according to need of the EPCA model.)

Parameters	Value	Parameters	Value
Young's Modulus	68000MPa	Residual coefficient	0.1
Poisson's ratio	0.3	Loading speed	0.002mm/step
Tensile strength(mean value)	20MPa	CA iterative precision	1e-7
Tolerance	1%	Softening coefficient	0.9
Homogeneous index	6.0	Random seed	15
Compressive strength (mean value)	295MPa		

The micro-cracks initiate from tips of the pre-fabricated fractures. When step 45 is reached, the crack propagating from the lower pre-fabricated fracture meets the upper pre-fabricated fracture. With increasing load, cracks in other parts of the specimen initiate, propagate and coalesce. They develop almost parallel to the loading direction (Fig. 3.17).

Figure 3.18 shows the relation of axial strain, radial strain and volumetric strain-stress. A prominent increase of radial strain and volumetric strain is found during the propagation of cracks. From Fig. 3.19, corresponding to the microcrack propagation, there are a certain number of AE counts produced.

3.4. Conclusions

The most important feature of the EPCA model is that it can be used to perform research on rock failure process while taking rock heterogeneity into consideration. By introducing the linear combination of stress and strain control method, EPCA models can simulate not only Class I, but also Class II behaviour of rocks. From the simulations, some conclusions can be derived.

(1) In an EPCA model, the discontinuous, inhomogeneous and non-elastic nature can be simulated. The anisotropic feature will be developed in the near future to model the full DIANE features of real rock in uniaxial compression.

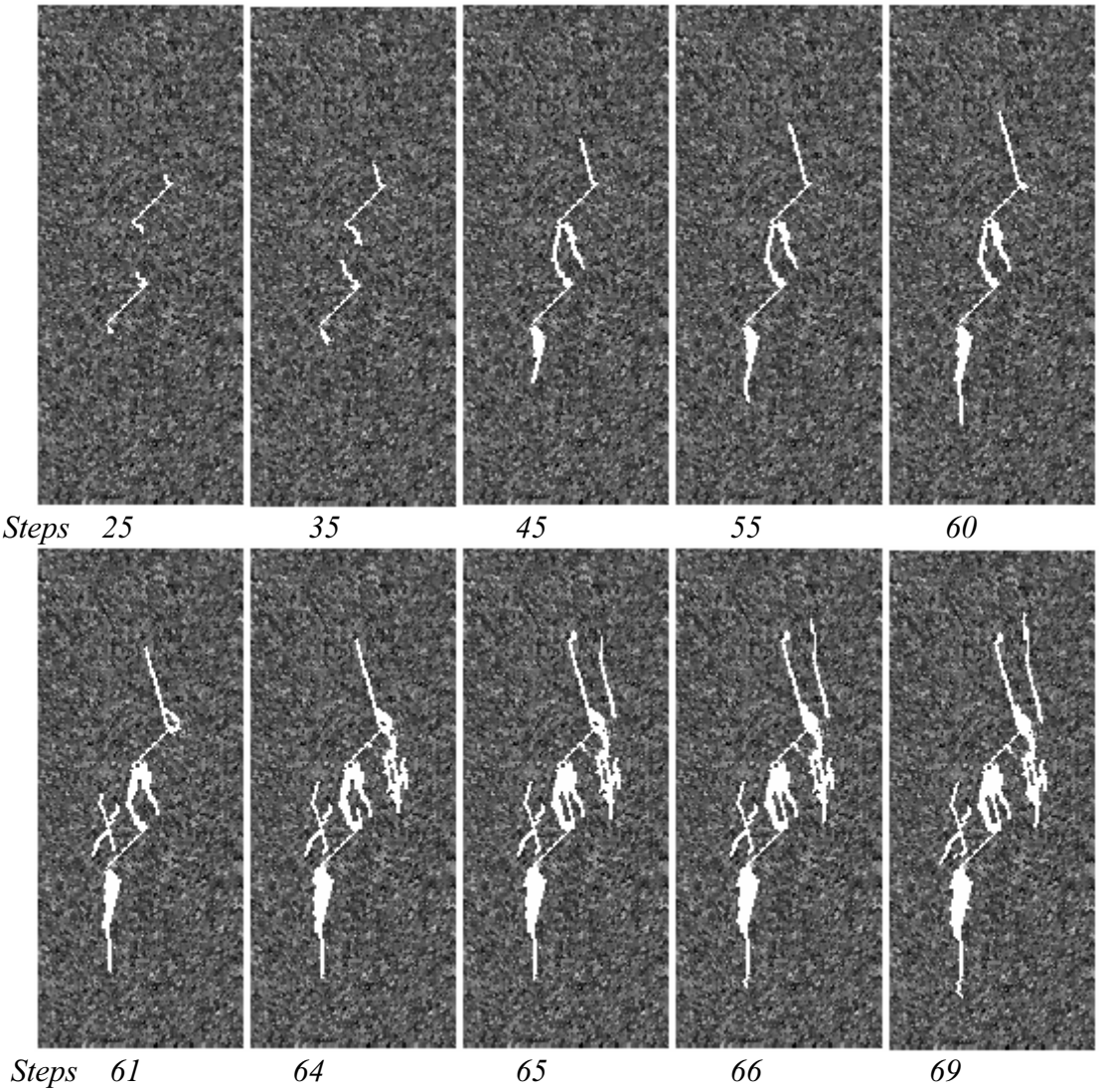

Figure 3.17: Double crack propagation process of dry rock model.

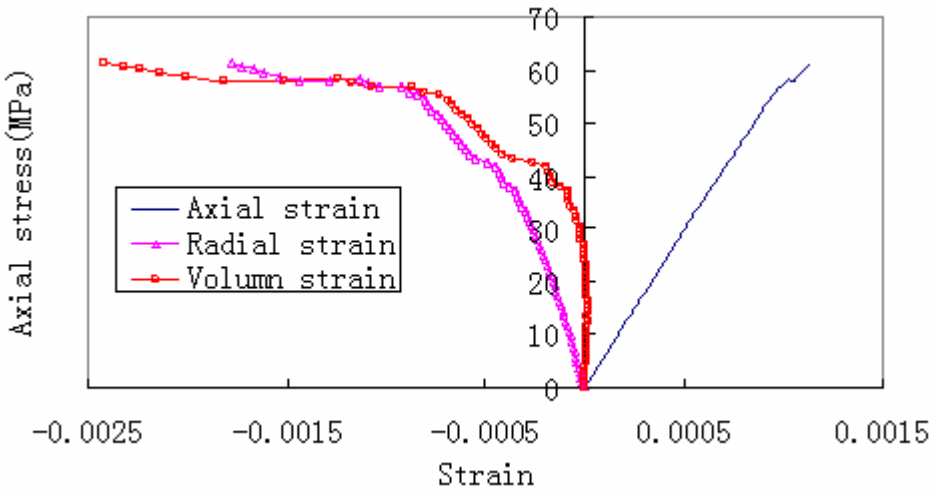

Figure 3.18: Axial, radial and volumetric strain-stress curves.

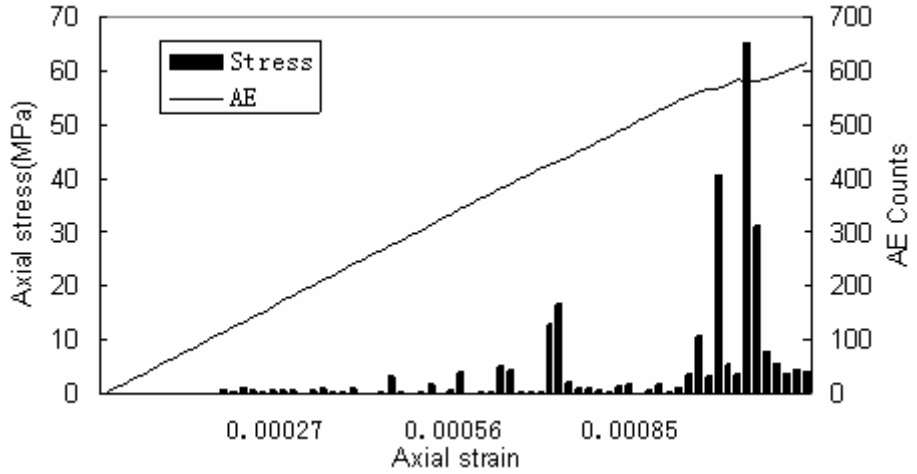

Figure 3.19: Stress-strain and AE curves.

(2) The failure mode and macro stress-strain behaviour depends strongly on the homogeneity of rocks. Different elemental spatial distribution will lead to different failure modes, which explains why the failure modes of rock specimens from the same rock mass are different in experiments.

(3) By using the linear combination of stress and strain loading control method, not only Class I but also Class II curves can be simulated. However, whether the rock behaves as Class I or Class II is decided by many factors such as loading control parameters, homogeneous index and the yield criteria etc.

(4) In order to simulate the failure process of rocks, we need to select appropriate material parameters, such as homogeneous index and elemental spatial distribution property etc., according to the real mechanical property of rocks.

(5) It is difficult to validate the homogeneity parameters used in modelling against the measured properties with acceptable accuracy. In the simulations, we have tried to use different homogeneity parameters *m* to make sure that the macro uniaxial compressive strength approximately equals that of the measured data. The seed number determines the spatial distribution of heterogeneity. It has little influence on the uniaxial compressive strength, but great influence on the final failure mode of rocks.

References

Dems K, Mroz Z. *Stability condition for brittle plastic structure with propagation damage surface*. J. Struct. Mech. 1985, 13(1): 85-122

Feng X T, Pan P Z, Zhou H. *Simulation of rock microfracturing process under uniaxial compression using elasto-plastic cellular automata*. Int J. Rock Mech. and Min. Sci. 2006 (in press)

Okubo S, Nishimatsu Y. *Uniaxial compression testing using a linear combination of stress and strain as the control variable*. Int. J. Rock Mech. Min. Sci. & Geomech. Abstr, 1985, 22(5) : 323－330.

Pan P Z, Feng X T, John A Hudson. *Simulations on Class I and Class II curves by using the linear combination of stress and strain control method and elasto-plastic cellular automata* . Int J. Rock Mech. and Min. Sci. 2006 (in press)

Weibull W. *A statistical distribution function of wide applicability*. J. Appl. Mech. 1951: 293-297.

Xu Bingye. *Plastic mechanics*. Beijing: Higher Education Press. 1988. (in Chinese)
Shen Xinpu，Cen Zhangzhi，Xu Bingye. *The characteristics of elasto-brittle-plastic softening constitutive theory and its numerical calculation*. Journal of Tsinghua University (Sci. & Tech)，1995，35(2)：22−27. (in Chinese)
Zheng H，Liu D F，Lee C F，Ge X R. *Principle of analysis of brittle-plastic rock mass*. Int. J. of Solids and Struc，2005，42：139−158.

4. Numerical simulation of tests of Äspö diorite core samples

Akira Kobayashi
Kyoto University, Japan

4.1 Problem setting for Class II behavior

JAEA team uses a continuum model considering the damage mechanics. In addition to conventional damage mechanics, the volume change due to damage development is implemented into the model. This model is called the damage expansion model in this report. The parameters are objectively identified from the results of unconfined compression tests (See Chapter 2). The damage is increased by the additional strain energy, and is not changed during the unloading process.

On the other hand, the Class II behavior is the result of the unstable fracture development in the post peak region. Wawersik (1968) pointed out that the energy must be extracted from the rock to prevent its violent collapse if the rock failure is unstable. He suggested the lateral displacement control to get the Class II behavior of stress-strain relation. The lateral displacement monotonically increases during Class II behavior and its rate is controlled to prevent the abrupt failure. Then the Class II curve for the axial stress–axial strain relation can be monitored. This is because the fracture is growing at the rate of extracting the energy from rock. Thus, the lower failure stress than the previous one is monitored when the stress is loaded again after extracting the energy. This means that the excessive energy is added to the rock before extracting the energy and the appearance of the effect of the excessive energy takes time. If the fracturing corresponding to the added energy occurs simultaneously, the abrupt failure will be monitored before extracting the energy.

The above consideration is based on the concept of the energy movement of rock as a homogeneous element. However, the actual behavior is not homogeneous. Fig. 4.1 shows a photograph of rock failure after an unconfined compression test. It is clear that the fracturing occurs very locally and that the critical fractures are very limited. This means that the added energy is consumed very locally. The remaining part adjoining to the fracture remains sound. This is because the energy consumption of the remaining part is very small. Fig. 4.2 shows the example of the axial stress – axial strain relation and volumetric strain–axial strain relation of an unconfined compression

test of the granite. These were measured by using the strain gauges and the load cell at the bottom of the specimen. The volumetric strain is obtained from the circumferential strain at the center of the specimen. In this test, the axial displacement was monotonically changed at a given rate to shorten the specimen. Although the specimen was collapsed by a few major fractures as shown in Figure 4.1, the strain measurement was successfully carried out because the fracture did not cross the strain gauges. It can be seen from axial stress–strain curve that the measured part was released after peak during continuous shortening of the specimen. At the same time, it can be found from the volumetric strain–axial strain relation that the fracture was growing because the specimen expanded continuously after the peak. This means that the energy input from the test apparatus was mainly consumed by fracture extension and that the energy of the measured part was also extracted for fracture growth. In this process, the fracture is stable because the energy is added to promote the further failure. On the other hand, the part adjoining the growing fracture shows the energy release state. The movement of energy is carried out in the specimen body.

Figure 4.1: Photograph of rock failure after unconfined compression test.(Äspö diorite rock core; photograph taken in the SP Lab, Borås, Sweden)

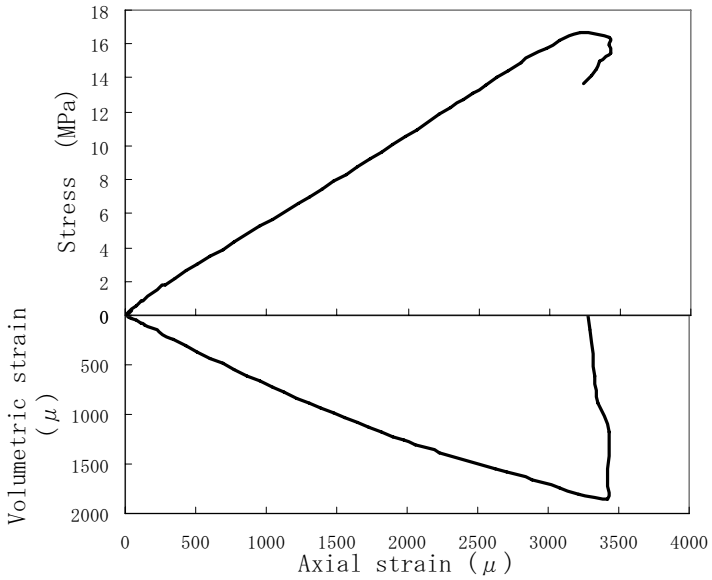

Figure 4.2: Example of stress-axial strain curve and volumetric strain –axial strain curve of unconfined compression test of granite with strain gauges. The positive strain shows the compression for both axial and volumetric strain.

The concept by Wawersik needs a new constitutive model. Moreover, the validation of the model has to be discussed for rational mechanics. On the other hand, the localization of energy consumption in the body can be discussed on the basis of conventional mechanics. Although the latter concept is not the same as the one of Class II by Wawersik, the observed behaviour is similar. In this report, the latter concept is discussed by using the damage expansion model.

4.2 Damage expansion model

4.2.1 Fundamental theory

In damage mechanics, the change in mechanical behavior due to the growth of damage (cracks) in material is considered (Lemaitre 1992). This behaviour is expressed by means of the damage variable D. The damage expansion model is based on damage mechanics theory. In the model, the total strain ε_{ij} is assumed to be decomposed into the elastic strain ε^{e}_{ij} and the isotropic expansive strain ε^{v}_{ij} as

$$\varepsilon_{ij} = \varepsilon^{e}_{ij} + \varepsilon^{v}_{ij} \tag{4.1}$$

where the expansive strain is a negative value. For the isotropic damage evolution, the total stress σ_{ij} – strain ε_{ij} relation is expressed as

$$\sigma_{ij} = (1-D)\left\{\left(\lambda\varepsilon_{kk}\delta_{ij} + 2\mu\varepsilon_{ij}\right) - \frac{1}{3}\varepsilon^{v}_{kk}(3\lambda + 2\mu)\delta_{ij}\right\} \tag{4.2}$$

where D is the damage variable, λ and μ are Lamé's constants. The expansive strain ε^{v}_{kk} due to damage progress is equal to $3\varepsilon^{v}_{11}$ because ε^{v}_{ij} is isotropic. The equivalent damage conjugate force Y_{eq} in relation to D is described as

$$Y_{eq} = K_d D^{n_d} + B_0 \tag{4.3}$$

where K_d and n_d depend on damage evolution, B_0 is the initial damage potential. Y_{eq} in relation to ε^{v}_{kk} is assumed to be

$$Y_{eq} = K_v\left(-\frac{1}{3}\varepsilon_{kk}^{v}\right)^{n_v} \tag{4.4}$$

where K_v represents the gradient of Y_{eq} – $(-\varepsilon_{kk}^{v}/3)^{n_v}$ curve and n_v is a scaling factor of the volumetric strain due to damage progress. In this report, K_d, n_d, B_0, K_v and n_v are called the damage parameters. When Y_{eq} is equal to $B+B_0$, the damage variable increases (Murakami and Kamiya 1997). B is the difference between the present damage potential Y_{eq} and the previous damage potential B_0

$$F\left(Y_{ij}, B\right) = Y_{eq} - (B_0 + B) = 0 \tag{4.5}$$

in which the equivalent damage conjugate force Y_{eq} is shown as

$$Y_{eq} = \sqrt{\frac{1}{2}Y_{ij}Y_{ij}} \tag{4.6}$$

where the damage conjugate force Y_{ij} is given as

$$Y_{ij} = -\frac{1}{2}\left(\lambda\varepsilon_{kk}^{e}\delta_{ij} + 2\mu\varepsilon_{ij}^{e}\right)\varepsilon_{ij}^{e} \tag{4.7}$$
$$(i = 1,2,3,\ j = 1,2,3,\ \text{no sum.})$$

4.2.2 Damage parameter identification

The damage parameters are determined by Equations (4.3) and (4.4), and the test results.

The expansive strain and damage variable are calculated from the test result. The expansive strain is calculated with following equation

$$\frac{1}{3}\varepsilon_{kk}^{v} = \frac{\varepsilon_{22} + \nu_0\varepsilon_{11}}{1+\nu_0} \tag{4.8}$$

where ε_{11} is the axial strain, ε_{22} is the tangential strain, and ν_0 is the Poisson's ratio at initial loading. The damage variable D is evaluated with axial stress σ_{11}, axial elastic strain ε^{e}_{11} and maximum Young's modulus E_0 while the damage variable is zero, given

by

$$D = 1 - \frac{\sigma_{11}}{E_0 \varepsilon_{11}^e} \tag{4.9}$$

The equivalent damage conjugate force Y_{eq} is given for the unconfined loading condition as

$$Y_{eq} = \sqrt{\frac{1}{2}\left(\frac{1}{2} E_0 \varepsilon_{11}^e \varepsilon_{11}^e\right)^2} \tag{4.10}$$

Then, Y_{eq}-D and $Y_{eq} - (\varepsilon^v_{kk}/3)$ relations obtained from the above process are fitted by Equations (4.3) and (4.4). Fig. 4.3 shows the process of fitting. The horizontal axis is first adjusted with n_d and n_v to make the test results a line in the $Y_{eq} - D^{nd}$ and $Y_{eq} - (\varepsilon^v_{kk}/3)^{nv}$ space. Then, the gradient of each line is obtained as K_d and K_v as shown in Fig. 4.3. B_0 in Equation (4.3) is also given from Fig. 4.3 (b).

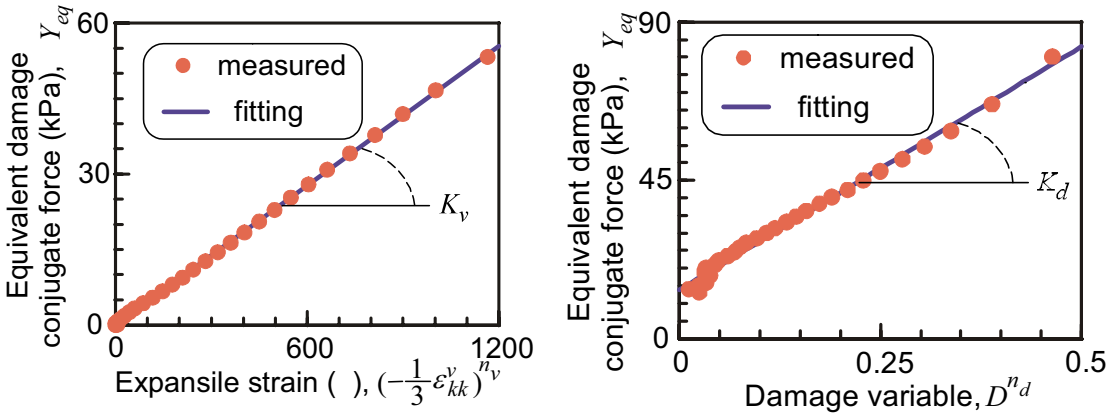

(a) *Fitting of K_v and n_v* (b) *Fitting of K_d and n_d*

Figure 4.3: Process to obtain the damage parameters

4.3 Localization of energy consumption

To investigate the effect of localization of the energy consumption, the unconfined compression test is simulated by using the tentative properties. Table 4.1 indicates the properties used in the simulation. In this simulation, the expansion due to damage development is not considered. Figure 4.4 shows the finite element mesh used for the

simulation. To introduce the heterogeneous energy consumption, the initial defect is set at the top of the specimen as shown in Fig. 4.4. This represents the disturbance of the edge due to cutting. At the region where the thickness is 1 mm, the initial damage variable D_0 of 0.3 and initial damage potential B_0 of 484 kPa are assumed. The other part has no initial damage. The bottom of the specimen has a roller condition and the top boundary has the prescribed displacement condition. For calculation of the strain, the axial displacements at two points on the surface of the specimen are used. The location of the two points is shown in Fig. 4.5. Three different distances are applied for the strain calculation, i.e., 36 mm, 80 mm and the top and bottom boundaries as shown in Fig. 4.5. The stress is obtained with the average equivalent nodal stress at the top boundary.

Table 4.1: Parameters used in the simulation using tentative parameters.

E(GPa)	n_d	K_d(MPa)	B_0(kPa)
6.80	0.24	1.36	76.2

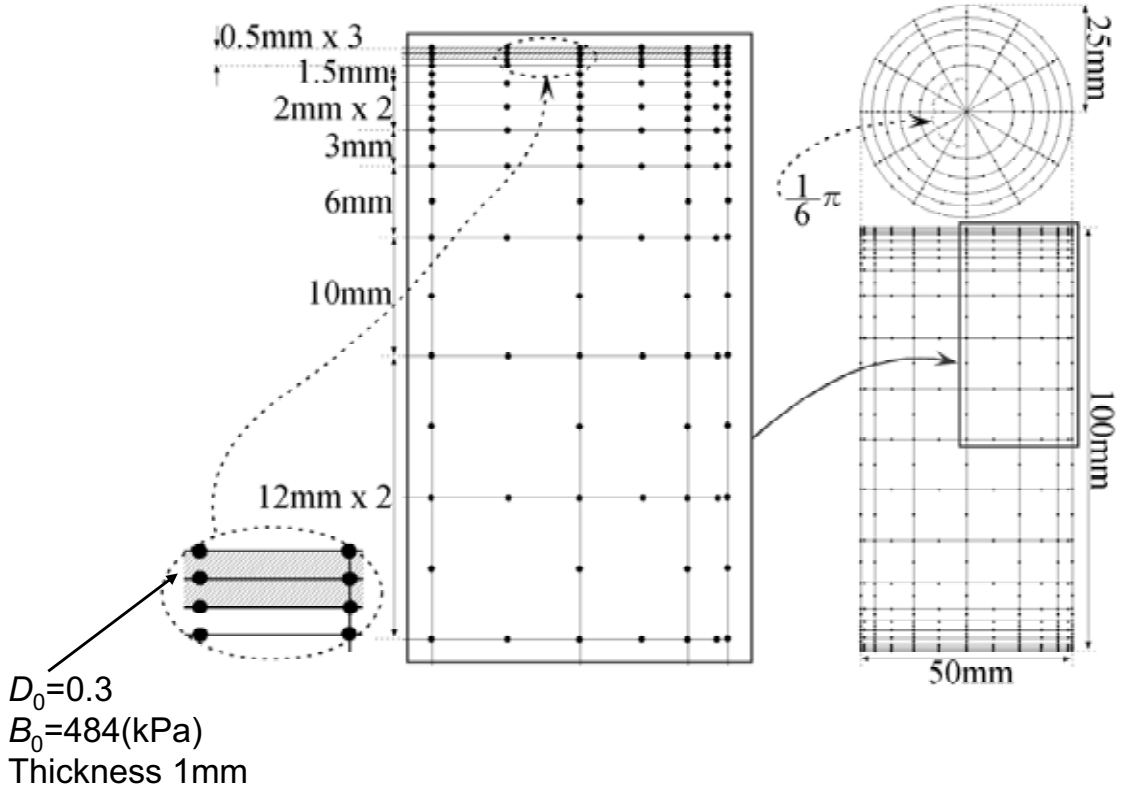

Figure 4.4: Finite element mesh for the examination of localization of energy consumption.

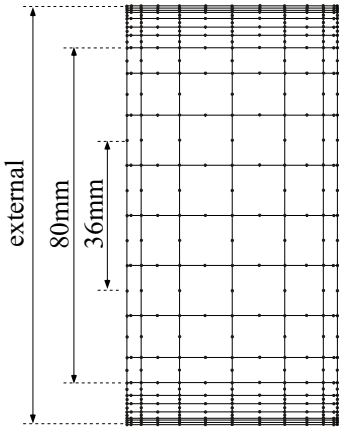

Figure 4.5: Location of strain measurement.

The simulated results are shown in Fig. 4.6. The measurement at the top and bottom boundaries, named 'external' in the figure, shows the infinite modulus, while the measurements at distances of 36 mm and 80 mm show the energy release state which is similar to the results observed with strain gauges shown in Fig. 4.2. Fig. 4.7 indicates the change in the distribution of the stress in the axial direction. During the loading process, the stress distribution becomes inhomogeneous gradually, as shown in (1) and (2) of Fig. 4.7. At the peak stress shown in (3), the low stress parts occur near the top boundary. It should be noticed that the lowest value shown in the figure is changed. Then, the almost zero stress occurs at the state of (4). By this zero stress at the upper region, the inner part becomes the location of the stress release and then the strain of the inner parts is reduced. The zero stress parts are introduced by the development of damage.

It can be seen from the above simulation that external work is consumed to develop a damage zone at the upper part and that the strain energy of the inner part is consumed for the development of the damage at the upper part. Such phenomena would happen for the results shown in Fig. 4.2.

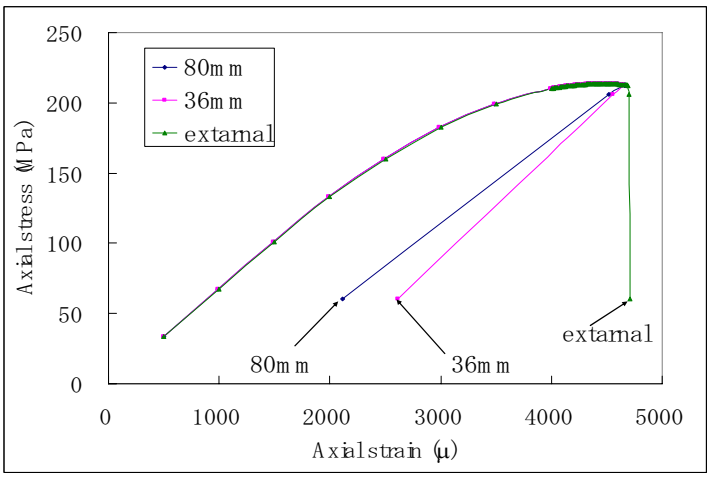

Figure 4.6: Simulated axial stress – axial strain relation.

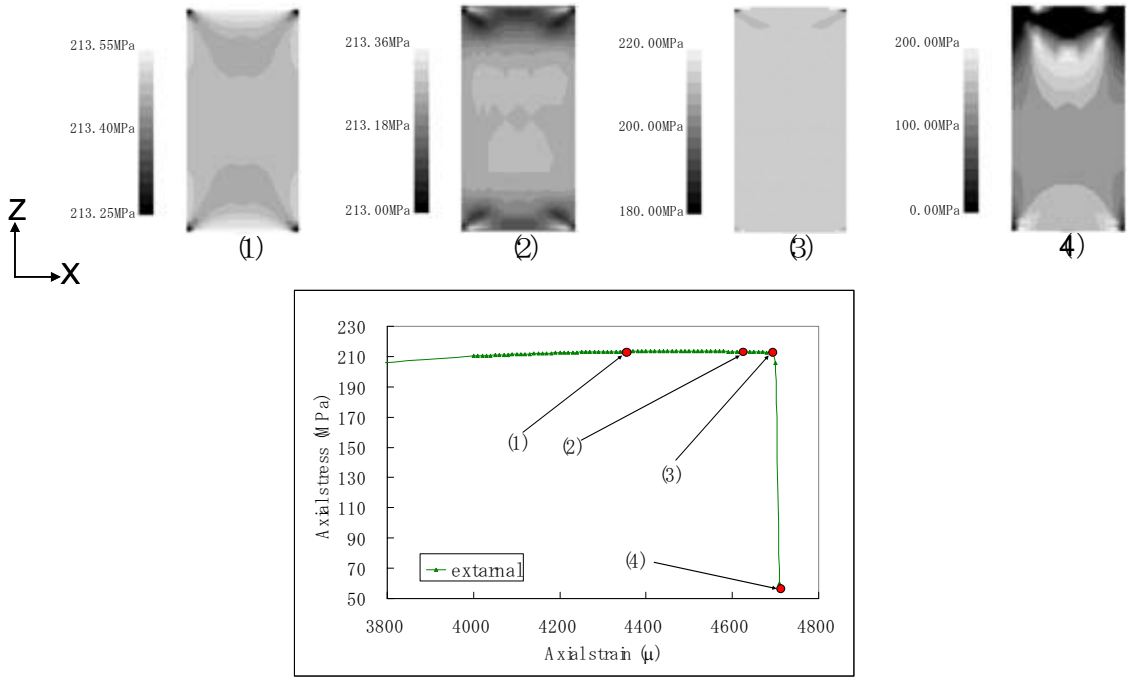

Figure 4.7: Change in distribution of stress in axial direction.

4.4 Examination of chemically degraded rock

4.4.1 Change in damage parameters

The stress-strain curve for chemically degraded rock was obtained by Jacobsson and Bäcksträm (2005). The damage parameters can be derived by applying the objective method mentioned in the section 4.2.2 to the stress-strain relations. The samples submerged in distilled and saline water for 90 days are examined to investigate the effect of the chemical degradation. This is because the behaviour of the sample preserved in the formation water was very similar to the one in the saline water.

The identified parameters are shown in Table 4.2. It can be seen that K_d and n_d become large and K_v becomes small. n_v increases a little. While K_d becomes large, n_d is also increased. Therefore, the peak strength is not expected to change so drastically by chemical degradation. On the other hand, since K_v becomes small and n_v increases, the brittle behaviour, sharp peak, and abrupt increase of volumetric strain may be intensified by degradation. However, the strain at the failure may not be changed so much because of increased K_d and decreased K_v.

Moreover, since B_0 becomes small, the development of damage will occur at an early stage. This may introduce an early failure, leading to a lower strength.

Table 4.2. Damage parameters for chemically degraded rock

	Distilled	Saline		Distilled	Saline
K_d	1.2MPa	1.7MPa	B_0	225 KPa	180 KPa
K_v	141MPa	106MPa	E_0	57 GPa	60GPa
n_d	0.5	0.8	ν_0	0.2	0.23
n_v	0.8	0.95			

4.4.2 Conditions of FEM simulation

To examine the effect of the chemical degradation of rock in detail, the simulation based on the proposed damage mechanics is carried out with a 3-D finite element method and the development of the damage is investigated in a similar way to the method in the section 4.3. The initial damage variable D is set at 0.01 for the element of 1mm thickness at the top and bottom of the specimen. By imposing the forced displacement, the unconfined compression test is simulated. The strain is calculated at locations having the distance of 50 mm on the surface of the specimen.

The damage parameters used for the simulation are shown in Table 4.2. In addition, based on the results of 90 days submergence, intensified damage parameters are assumed to investigate the effect of further chemical degradation. The intensified damage parameters are K_d =2.0KPa, K_v =70MPa, n_d =1.0, n_v =1.1 and B_0 =135 KPa, respectively. These values may correspond to more chemically degraded rock conditions.

4.4.3 Calculation results

Figure 4.8 shows the calculated stress-strain relations. While the actual data show a small strength in the case of saturation with distilled water, the strength is expected to be decreased by chemical degradation as shown in Fig. 4.8. This is probably because of the effect of the decreased B_0.

Figure 4.9 shows the distribution of the damage variable D and axial stress for each case. The number corresponds to the one shown in Fig. 4.8, at the stages just before peak and after softening of respective cases. In this figure, the black color for the damage variable shows a large amount of damage and the black color for axial stress indicates a large compression value. It can be seen that the location with little damage has a small compression stress while a large compression stress occurs at the location adjacent to a large damage area. After softening, the high damage area is developed from the stage just before peak strength. When there is no chemical damage (case of

distilled water), the damage is developed in the inner area of the specimen. On the other hand, if the chemical damage is intensified, the damage is focused on the edge of the specimen. This influence is probably the reason for the crack propagation from the surface of the chemically damaged specimen.

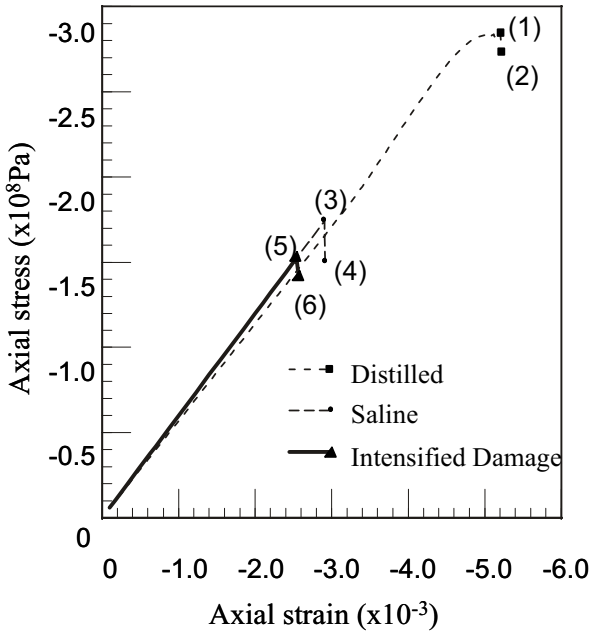

Figure 4.8. Calculated stress-strain relations.

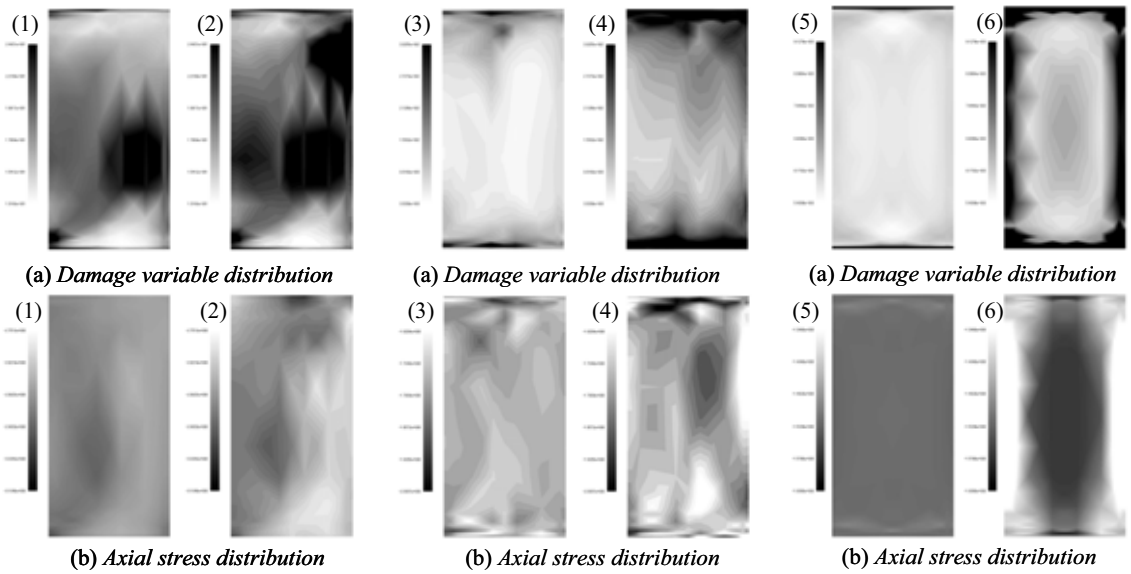

Figure 4.9: Simulation results for chemically damaged rock.

4.5 Conclusions

The concept by Wawersik is constructed by considering the unconfined compression test as an element test. On the other hand, the examination described in this report is fundamentally the initial-boundary-value problem. If we adopt the concept by Wawersik and continuum mechanics, we have to establish a constitutive law explaining the unstable damage development in the post peak region, which will be anisotropic and time dependent. The treatment introduced here is a method to avoid such a difficulty, while the problems related to the initial defect and the measurement location remain to be solved. If the axial displacement at the boundary is controlled to keep the average volumetric strain at some rate, the ability to reproduce the Class II behavior may be examined. However, such a simulation is very troublesome and its meaning is doubtful. The important thing for an engineering problem is the resolution of the degree of localization of strain and the up-scaling method of the effect of the localization.

The method introduced in this report does not have a high degree of resolution for localization of strains. However, there will not be so many problems for up-scaling of the effect in comparison with the discontinuous method.

References

Lemaitre, J., *A course on damage mechanics.* Berlin: Springer-Verlag.1992.

Murakami, S. and Kamiya, K., *Constitutive and damage evolution equations of elastic-brittle materials based on ir-reversible thermodynamics.* Int. J. Mech. Sci., 1997; 39(4): 473-486.

Wawersik, W.R., *Detailed analysis of rock failure in laboratory compression tests*, PhD thesis, University of Minnesota. 1968.

5. Numerical simulation of core tests - a particle mechanics approach

Tomofumi Koyama and Lanru Jing
Royal Institute of Technology, Stockholm, Sweden

5.1 Introduction

5.1.1 Background and motivation

The damage mechanisms and failure processes of rocks have been important issues in the field of rock mechanics, especially when the effects of the EDZ (excavation induced damage zone) on the fluid flow and radioactive nuclide transport processes for nuclear waste repositories are concerned. During the evolution of the EDZ, there are several processes operating, involving initiation, growth, coalescence and localization of microcracks and final transformation of material-structural failure mechanisms, or bifurcations. The EDZ phenomenon of microcracking and its development in the near-field of a rock excavation, caused by a change in the local stress field, therefore, becomes one important subject since the continuity of such microcrack-prone EDZs along the axis of the tunnels of the repository might become conduits for easier nuclide transport.

It is well-known that the micro-cracks and their growth in rocks are affected by the moisture content and chemical behaviour of the fluids in rocks. As a result, the mechanical behaviour and failure processes of rock will be changed. Some results obtained from laboratory experiments show that the strength of rocks decreases under saturated conditions with/without chemical solution (Seto *et al*., 1998; Feng *et al*., 2001). However the basic chemical mechanism involved in this strength weakening of rocks is still unclear.

A great number of numerical models have been developed to simulate the damage and failure processes of rocks and they can be categorized into continuum-based and discontinuum-based approaches. The continuum approach, such as the Finite Element Method (FEM), aims to capture the deformation and failure processes by specially developed constitutive models, such as elasto-plastic/elasto-viscoplastic models (e.g. Adachi *et al*., 2005) and damage mechanics models (e.g. Golshani *et al*., 2005). This approach may have two drawbacks (Cundall, 2001): 1) the constitutive laws tend to become more and more complicated with many parameters that may be difficult to measure in laboratory tests and 2) simulation of fracture initiation and propagation processes are difficult challenges.

The particle mechanics approach, as one branch of the general discontinuum approach, can treat fracture initiation and growth directly at micro- or macro-scopic levels, with much simpler assumptions on constitutive behaviours of the rock matrix and fractures, and far fewer numbers of parameters. The most well known code for the particle mechanics approach is the Particle Flow Code (PFC) (ITASCA, 2003; Potyondy and Cundall, 2004) and PFC has been used to simulate many rock mechanics problems at both laboratory and field scales (e.g. Wang *et al*., 2003; Aoki *et al*., 2004; Tannant and Wang, 2004; Al-Busaidi *et al*., 2005).

There may exist three controversial issues for particle mechanics models, especially for rock mechanics applications. One is how to decide microscopic parameters that cannot be measured directly during the mechanical experiments. The second is what model sizes should be selected for reliable simulations, and the third is how representative the particle sizes should be. The last two issues are actually subsets of the first one that is most fundamental.

Due to the impossibility of direct measurement of micro-mechanical properties of rocks (such as contact stiffness and strength at the grain boundaries) in the laboratory, back-calculation techniques are commonly applied through numerical calibrations. To obtain micro-mechanical parameters that will reproduce or approximate adequately the macroscopic behaviour of rocks, a series of numerical calibration simulations of some usually small scale laboratory experiments of rock samples are required when using the particle mechanics approach. The measured macroscopic mechanical properties, most typically Young's modulus, Poissons's ratio and uniaxial compressive strength, are used as the measured macroscopic parameters, which are compared with equivalent values of these parameters derived from particle models with identical boundary conditions, through an iterative trial-and-error process (see Section 5.2.3). Thus the microscopic parameters obtained are unique to the particle mechanics code applied and are therefore subjective to the basic assumptions of the approach, most significantly model and particle sizes, contact models, and initial conditions (such as packing configurations).

The remaining two issues, the sizes of particles and models, are interrelated. However, there has been no commonly accepted standard for addressing these two related issues. For most of the applications, such as those mentioned in the literature above, the sizes of models and particles are determined not according to material behaviour but to the engineering needs or computer memory limitations, often without checking the impact on the final results. Therefore they are still largely unresolved issues.

It is well known that many geological materials, typically crystalline rocks, exhibit scale dependency in terms of strength and deformability, due to the differences in local micro-structures. Hence the investigation of Representative Elementary Volume (REV) size is important in justifying the applicability of the equivalent continuum approach. A REV is defined as the minimum size of a sampling domain beyond which the characteristic properties of the sampling domain remain constant. In this regard, for calibration simulations for establishing micro-mechanical parameters of particle mechanics codes, the measured mechanical properties must be obtained from rock samples that are not less than a REV size. Otherwise the measured macroscopic properties themselves are not representative. Since the numbers of the particles in a model are also determined by the model size, therefore the derived micro-mechanical parameters depend on both model and particle sizes. The two issues should therefore be addressed simultaneously.

5.1.2 Objectives

The objectives are: 1) evaluation of the REV size and equivalent microscopic mechanical properties of the Äspö diorite rock, considering the effect of different particle size distributions, 2) evaluation of the equivalent micromechanical properties of the Äspö diorite rock samples saturated with saline formation water and distilled water, or dry samples, and 3) predictive simulation of rock core samples' complete stress-strain curves under uniaxial compression.

5.2 Numerical method: Particle mechanics approach

5.2.1 Particle Flow Code (PFC)

The particle mechanics code applied is the Particle Flow Code (PFC^{2D}) (ITASCA, 2003; Potyondy and Cundall, 2004), which simulates the mechanical behaviour of a rock material represented as an assemblage of many small rigid circular particles bonded together (Fig. 5.1). The movement and interaction of each particle is calculated using the central finite difference methods as applied in the distinct element method (DEM). For the models of contacts, both linear and non-linear (Hertz) contact models with frictional sliding can be used. The linear contact model, which was used in this study, provides an elastic relation between the relative displacement and contact force of particles.

The basic contact model in the PFC code (contact force-displacement relation) is the linear point contact between two particles (Fig. 5.1b), relating contact normal force component, F^n, contact overlap, U^n, increment of shear force, ΔF^s and displacements, Δu_s, given by

$$\begin{cases} F^n = K^n U^n \\ \Delta F^s = -k^s \Delta U^s \end{cases} \tag{5.1}$$

where K^n and k^s are the contact normal and shear stiffness with unit Pa/m, respectively, and the frictional strength of the contact is given by

$$F^s \le \mu F^n \tag{5.2}$$

where μ is the friction coefficient between particles.

Point contact models in equation (5.1) can only consider relative motions between individual particles. However, when a group of bounded particles needs to be considered as a whole, cemented contacts including both contact forces and torques are needed (Fig. 5.1a and c). In such a case, the relations between the above incremental quantities become

$$\begin{cases} \Delta \overline{F}^n = \overline{k}^n A \Delta U^n \\ \Delta \overline{F}^s = -\overline{k}^s A \Delta U^s \end{cases} \tag{5.3}$$

and

$$\begin{cases} \Delta \overline{M}^n = -\overline{k}^s J \Delta \theta^n \\ \Delta \overline{M}^s = -\overline{k}^n I \Delta \theta^s \end{cases} \tag{5.4}$$

where $\overline{F}^n$, $\overline{F}^s$, $\overline{M}^n$ and $\overline{M}^s$ are the components of force and torques (moments) about the centre of the cement contact zone, $\overline{k}^n$ and $\overline{k}^s$ are normal and shear bond stiffness per unit area, θ^n and θ^s are the components of rotation angle, and A, I and J are the area, moment of inertia and polar moment of inertia of the bond cross-section,

respectively. The strength of the cement contact is then written

$$\bar{\sigma}^{\max} = \frac{-\bar{F}^n}{A} + \frac{\left|\bar{M}^s\right|\bar{R}}{I} < \bar{\sigma}_c \tag{5.5}$$

$$\bar{\tau}^{\max} = \frac{\left|\bar{F}^s\right|}{A} + \frac{\left|\bar{M}^n\right|\bar{R}}{J} < \bar{\tau}_c \tag{5.6}$$

where $\bar{R}$ is the radius of the cement zone (Fig. 5.1c), $\bar{\sigma}_c$ and $\bar{\tau}_c$ are tensile and shear strength of the cement contact, respectively.

Young's moduli for particle contact, E_c and particle bondage $\bar{E}_c$ are defined to relate the contact and bond stiffness as follows

$$E_c = \frac{k_n}{2t} \quad (t=1 \text{ in 2D}) \tag{5.7}$$

$$\bar{E}_c = \bar{k}_n\left(R^{(A)} + R^{(B)}\right) \tag{5.8}$$

where $R^{(A)}$ and $R^{(B)}$ are particle radii in contact (Fig. 5.1b and c).

In the PFC code, cement contacts as expressed in (5.3-5.6 and 5.8) above are called parallel bonds. A parallel bond uses a set of elastic springs uniformly distributed over a rectangular cross-section lying on the contact plane and centred at the contact point. These springs act in parallel with the linear point-contact springs. Relative motion at the contact causes an incremental force and moment to develop due to the parallel bond stiffness.

The micro-crack initiation and propagation can be expressed as a progressive breakage of contact bonds. The crack pattern is automatically determined without any remeshing and can be observed directly during the simulation. Heterogeneity and weak planes can easily be considered in this code. Further details including basic theory can be seen in ITASCA (2003) and Potyondy and Cundall (2004).

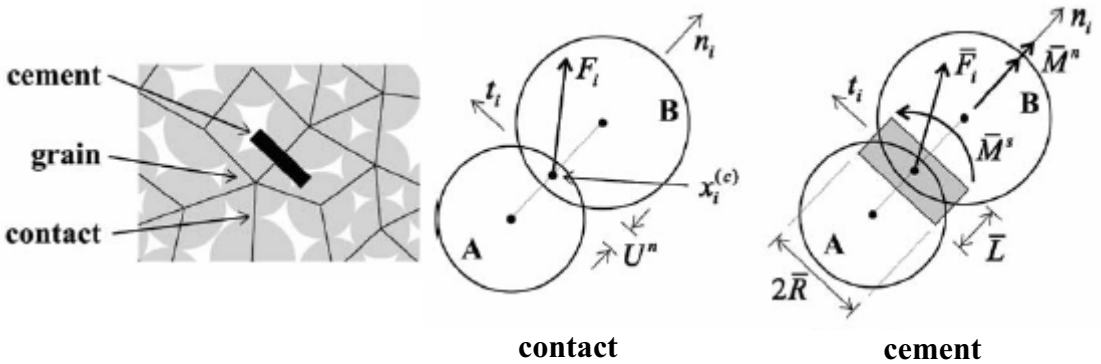

Figure 5.1. The force-displacement relation for bonded particles system (after Potyondy and Cundall, 2004).

5.2.2 Experimental data from laboratory uniaxial compressive tests

A series of uniaxial compressive tests were carried out using rock core samples obtained from a tunnel in Äspö Hard Rock Laboratory (HRL), Sweden (Jacobsson and Bäckström, 2005). The set of test results was used to calibrate the micro-mechanical parameters for PFC^{2D} models, to evaluate the REV and particle size effects and finally to simulate the evolution of micro-structural variations of crack patterns and particle system geometry with the development of stress-strain curves as commonly observed in rock mechanics testing.

5.2.3 Numerical calibration of microscopic mechanical parameters of the Äspö diorite

A typical PFC^{2D} model requires the following micro-mechanical parameters for the system characterization: 1) particle radius, 2) stiffness of the particle contacts, 3) friction coefficient between particles and 4) normal and shear strength for bonds. Since these micro-mechanical parameters cannot be measured directly during laboratory experiments, numerical calibration is required to back-calculate them using measured values of some commonly measured intact rock properties, such as Young's modulus, Poisson's ratio and uniaxial compressive strength (UCS). Figure 5.2 shows a particle mechanics model of a Äspö diorite sample (of about 5 cm × 12 cm in size) with 8898 particles. The horizontal (upper and lower) boundaries were moved slowly to simulate the uniaxial compression test. The axial stress and strain are derived from the calculated contact forces and particle displacement, respectively, at the horizontal boundaries and selected reference particles respectively. During the calibration, to reduce the number of unknown microscopic parameters, the following assumptions were made: 1) minimum particle radius is fixed to 350 μm, which is assumed to represent the grain size distribution of rock minerals when the actual grain size distribution is not available, 2) all particles have the same density equal to the density of rock core sample measured during the laboratory experiment, 3) the values of Young's modulus for particle contact and parallel bond are set equal. 4) stiffness ratios of particle contact and parallel bond are set as the same, 5) both parallel bond normal and shear strength were given deterministically, even though these values can be given stochastically.

Tables 5.1 and 5.2 show the lists of the microscopic parameters adopted in this study to characterize the microscopic behaviour of the diorite rock and the calibration results, respectively. Here three different particle size ratio distributions, called case I, II and III, were considered for REV studies (see Fig. 5.3c and section 5.3.1). The results show that the derived equivalent micro-mechanical parameters in all three cases generated equally acceptable values for the measured macroscopic properties of Young's modulus, Poisson's ratio and the uniaxial compressive strength. They can, therefore, serve as basic sets of microscopic parameter values for further study on the impact of model and particle size, prior to the predictive modelling on rock failure mechanisms.

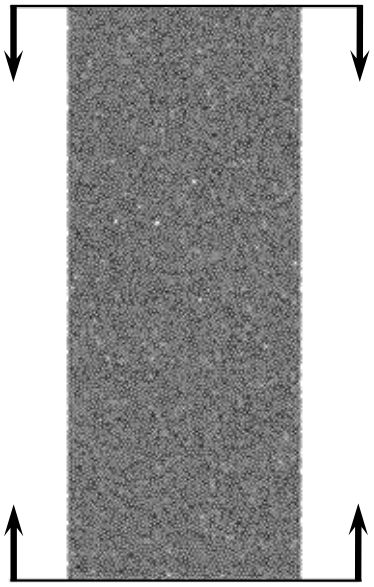

Figure 5.2. The synthetic material of Äspö diorite with 8898 particles and uniaxial compressive testing environment for PFC^{2D}.

Table 5.1. Microscopic parameters of PFC^{2D} model used in this study.

	Case I	Case II	Case III
Ball Density [kg/cm^3]	2670	2670	2670
Minimum ball radius, R_{min} [mm]	0.35	0.35	0.35
Ball size ratio, R_{max}/R_{min}	1.5	2.0	3.0
Number of balls	8898	6179	3476
Ball-ball contact Young's modulus, E_c [GPa]	70	71	70
Ball stiffness ratio, k_n/k_s	4	4	4
Young's modulus of parallel bond, $\overline{E}_c$ [GPa]	70	71	70
Parallel bond stiffness ratio, λ	4	4	4
Particle friction coefficient, μ	0.5	0.5	0.5
Parallel bond normal strength, mean, $\overline{\sigma}_c$ [MPa]	502	537	540
Parallel bond normal strength, std. dev, $\overline{\sigma}_c$ [MPa]	0	0	0
Parallel bond shear strength, mean, $\overline{\tau}_c$ [MPa]	125.5	134.25	135
Parallel bond shear strength, std. dev, $\overline{\tau}_c$ [MPa]	0	0	0

Table 5.2. Calibration results.

	Case I	Case II	Case III	Tested data
Sample size (Diameter [mm]/length [mm])	50.8/125.4	50.8/125.4	50.8/125.4	50.8/125.4
Young's modulus, E [GPa]	71.07	70.69	69.68	70
Poisson's ratio, ν	0.290	0.293	0.304	0.29
Uniaxial compressive strength, q_u [MPa]	294.24	293.91	295.71	295

5.3 Numerical analysis of REV size and representative particle size distributions

5.3.1 Methodology – Stochastic REV approach

Figure 5.3 shows the schematic view of the stochastic procedure of bonded particle model realizations of 20 different sizes for establishing the REV size of the Äspö diorite, progressively increasing from 1 cm × 1 cm to 10 cm × 10 cm as square-shaped models. Figure 5.3a shows five of them as examples of particle system geometry varying in size (and number of particles), with three different ranges of particle size (Case I, II and III). Their locations are generated randomly as a Poisson process. For each model size, twenty different realizations were generated (Fig. 5.3b) and in total 200 stochastic particle models are created for the study. The values of the microscopic parameters (see Tables 5.1 and 5.2) are determined through the calibration of Äspö diorite samples tested in the laboratory (Jacobsson and Bäckström, 2005).

Figure 5.4 shows the bi-axial testing boundary condition for particle models. A numerical servo-control is applied for the two vertical boundaries to keep a constant (horizontal) confining stress, σ_x =5 MPa. The upper and lower horizontal boundaries move slowly and σ_y are calculated from the contact force at these boundaries. It should be noted that the peak strength is evaluated in terms of the maximum value of σ_y and not the differential stress, σ_y-σ_x in this study.

The numerical bi-axial tests were performed to calculate the equivalent values of the same three macroscopic properties of Young's modulus, Poisson's ratio and peak strength, whose variation with sample size is used as an indicator for the REV size.

5.3.2 Study of the sample size effect by multiple realization

Figure 5.5 shows the results for the calculated values of Young's modulus, Poisson's ratio and peak strength from the twenty stochastic realizations with different model sizes, using the Case I set of micro-mechanical parameters. With a side length of 2 cm, the most drastic reduction in variation can be observed, especially in Young's modulus and peak strength (Fig. 5.5a and c). Their respective variations become smaller with increasing model size and become almost constant after about 5 cm of the model size.

To facilitate the stochastic REV analysis, for the side lengths of 1, 2, 3, 5, 7 and 10cm, the number of particle system realizations was increased to 100 to derive the statistical range of the target macro-mechanical properties, using the same Case I micro-mechanical parameters. The frequency histograms of three macro-properties from the 100 random particle models with a side length of 5 cm are created, with three of them shown in the left column of Fig. 5.6. From these histograms, the calculated macro-mechanical properties were fitted approximately to normal distribution curves, as shown in the right column of Fig. 5.6, together with similar curves for sample sizes of 1, 2, 3, 7, and 10 cm. The results show that the calculated values of all three macro-mechanical properties are more concentrated around the mean values with increasing model size. The mean values increase slightly with increasing model size but do not show significant changes after 7 cm of model side length, indicating that model size reaches a REV at 7 cm × 7 cm.

The different indications of REV values from Figs. 5.5 and 5.6 indicate that purely

visual examination for REV size determination is subjective, although it may not affect final results significantly for engineering applications. To reduce the impact of such subjective determination of REV size, in this study a coefficient of variation is defined as the ratio of the standard deviation to the mean value of the respective macro-mechanical properties, as a measured to determine the REV size, depending on the desired resolution of the final results. The calculated coefficients of variation for Young's modulus, Poisson's ratio and peak strength were plotted, Fig. 5.7, for the Case I set of micro-mechanical parameters. This shows decreasing coefficients of variation for all three mechanical properties with the increasing model size.

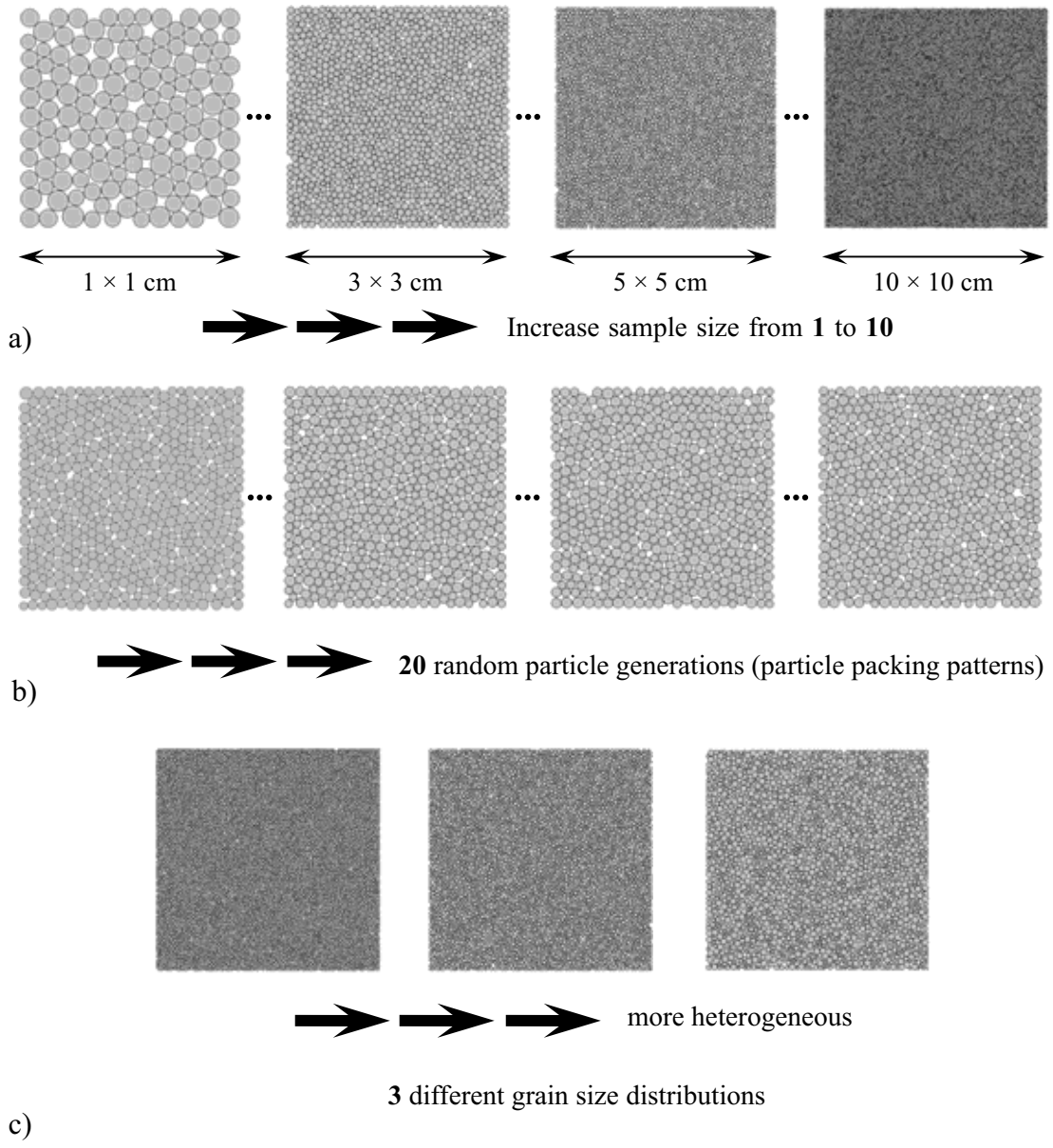

Figure 5.3. The schematic view of the stochastic procedure of bonded particle model generation. The particles were generated in a) a square domain with side lengths varying from 1 cm to 10 cm and b) twenty models are randomly generated for each model size. A total of 200 models are used in the scale dependency investigation, and c) three different grain size distributions were considered to investigate the effect of grain size heterogeneity on the REV size.

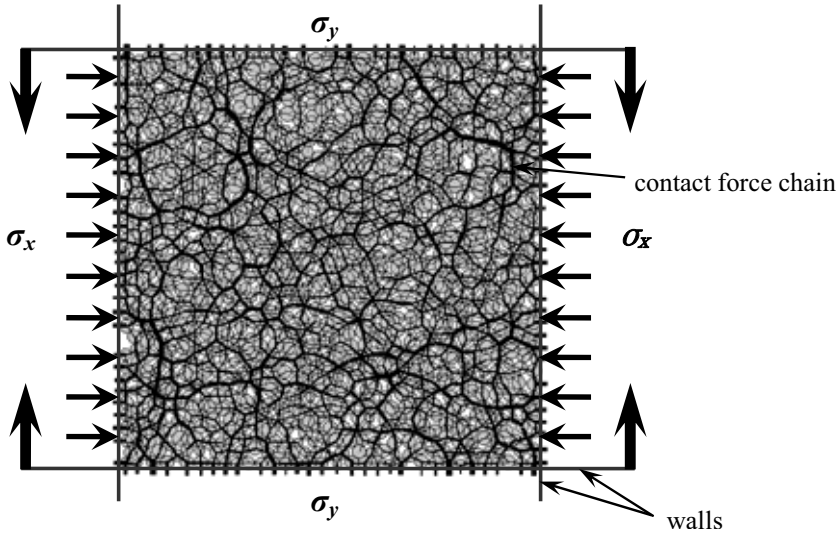

Figure 5.4. Numerical simulation for bi-axial test in PFC^{2D}. It should be noted that σ_x is kept constant by the servo-control mechanism and σ_y is calculated from the contact force during the movement of horizontal walls.

5.3.3 Particle size effect on the results of REV size

To investigate the effect of particle size on the REV size, the particles were given uniform distributions in particle radii ranging from 350 μm to 525 μm for Case I, from 350 μm to 700 μm for Case II and from 350 μm to 1.05 mm for Case III, respectively, representing the range of grain size distributions of the Äspö diorite. It should be noted that the minimum particle size was fixed for the purpose of simplicity in this study. The particle system becomes more heterogeneous (Fig. 5.3c) from Case I to Case III. On changing the particle size, the micro-mechanical parameters should be recalibrated to establish corresponding values of the macro-mechanical properties in order to examine the effect of the particle size. Hence calibration results for Case II and Case III are also shown in Tables 5.1 and 5.2.

Similar figures to Figs. 5.5 and 5.6 can be drawn for Case II and III and the coefficient of variation can be also calculated, but to avoid repetition are not presented. Fig. 5.8 shows the comparison of the coefficient of variation of macroscopic mechanical properties as a function of model size for the three different particle size distributions. From this figure, it can be seen that the coefficients of variation for mechanical properties decrease with the increase in model size for all cases, but increase with particle size. Therefore, for engineering applications, compromise needs to be made about model size and particle size with a chosen acceptable variation coefficient. Table 5.3 shows the REV sizes with different (chosen) acceptable variations for the three particle size distribution cases (I, II and III). Acceptable variation can be chosen differently for the different needs of engineering applications. However, without such a controlling measure, the reliability of particle models may become an unknown factor affecting the reliability of the results. For rock engineering applications, a 5% criterion is usually adequate. The size of cylindrical rock core samples of Äspö diorite tested for this study is about 5 cm in diameter and 12 cm in height. This means that the size of the core satisfies the REV size requirement with an acceptable variation of 5 %, using the Case I microscopic parameter list in Table 5.1.

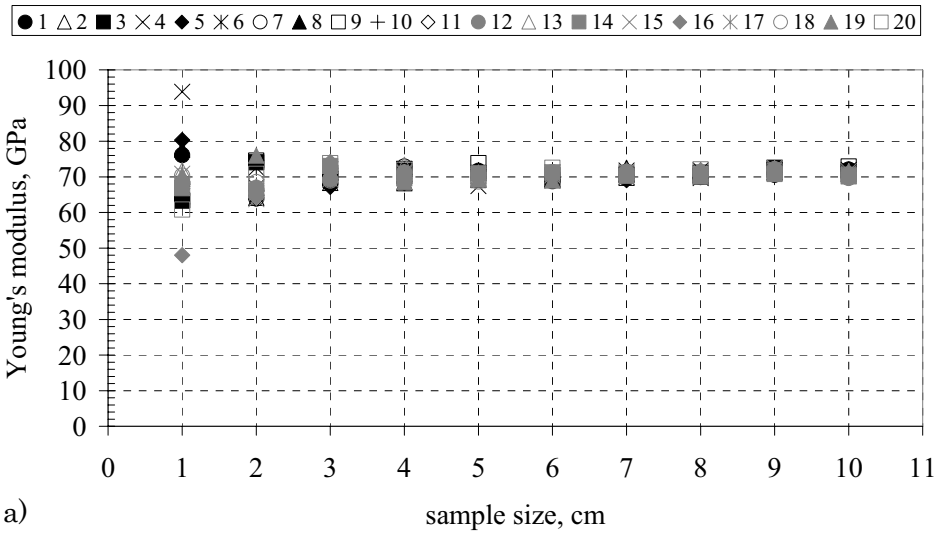

a)

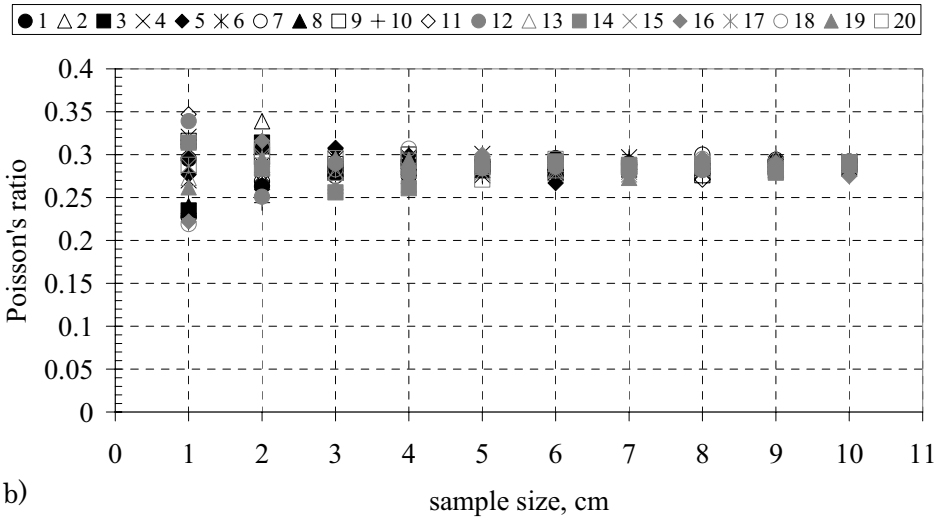

b)

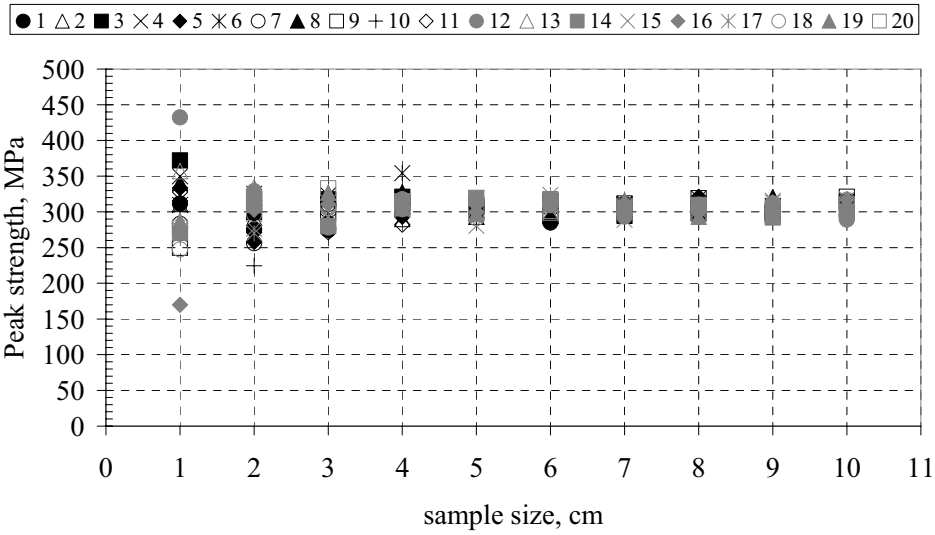

c)

Figure 5.5. Results of calculated macroscopic mechanical properties from 20 realizations. a) Young's modulus, b) Poisson's ratio and c) peak strength.

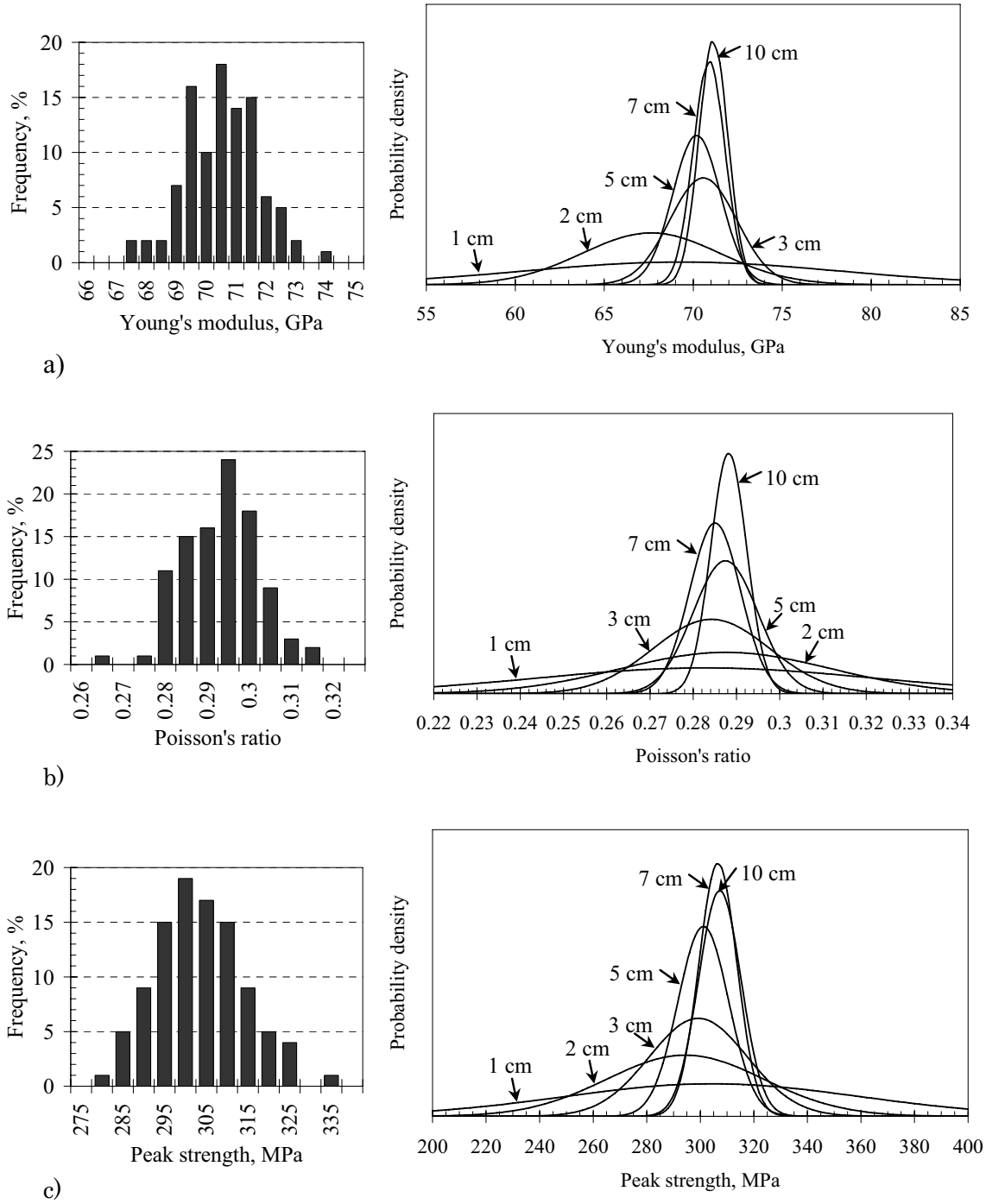

Figure 5.6. Frequency histograms of calculated mechanical properties using PFC with a side length of 5 cm from 100 realizations and the probability density functions of mechanical properties at different model sizes, a) Young's modulus, b) Poisson's ratio and c) peak strength.

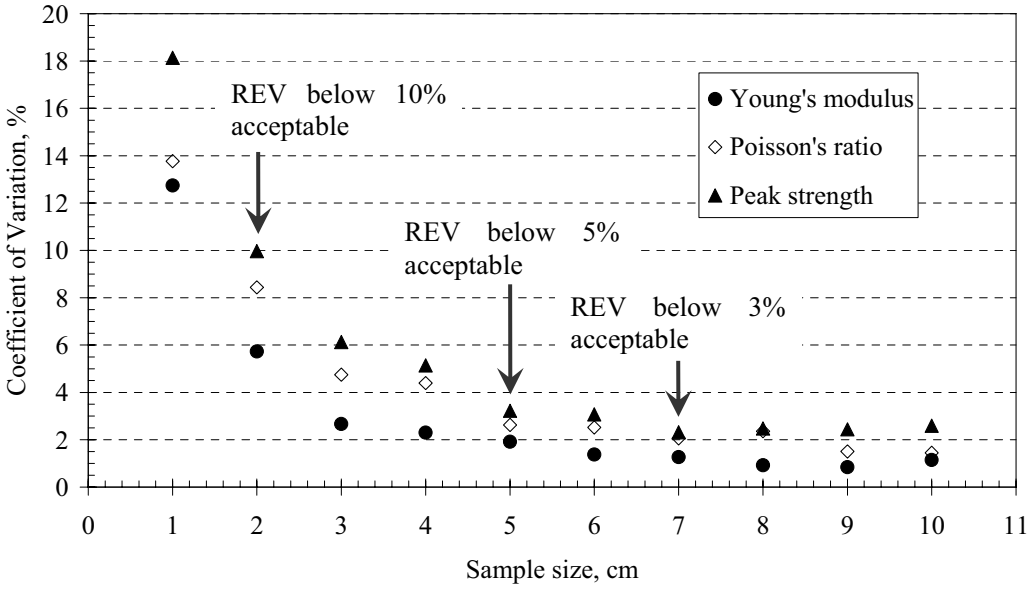

Figure 5.7. The coefficient of variation of macroscopic mechanical properties (Young's modulus, Poisson's ratio and peak strength) as a function of sample size (case I).

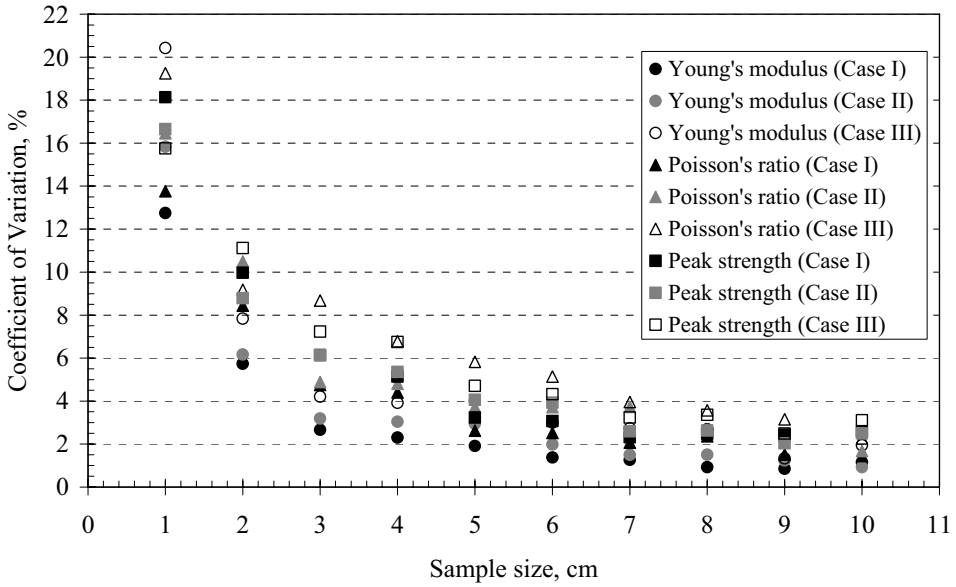

Figure 5.8. Comparison of the coefficient of variation of macroscopic mechanical properties in terms of ball size ratio (R_{max}/R_{min}) (1.5 for CaseI, 2.0 for Case II and 3.0 for Case III).

Table 5.3. REV determination based on coefficient of variation

	Acceptable variation, %	Mechanical REV for Case I	Mechanical REV for Case II	Mechanical REV for Case III
Coefficient of variation	10	2 cm × 2 cm	3 cm × 3 cm	3 cm × 3 cm
	5	5 cm × 5 cm	5 cm × 5 cm	7 cm × 7 cm
	3	7 cm × 7 cm	8 cm × 8 cm	> 10 cm × 10 cm

5.4 Simulating tests of Äspö diorite core samples

5.4.1 Experimental data

To investigate the effect of fluids on the mechanical properties of intact rock, a series of laboratory uniaxial compressive tests were performed using diorite rock samples obtained from Äspö Hard Rock Laboratory in Sweden in a dry condition and in the following three different liquid saturation cases: 1) distilled water, 2) saline water and 3) formation water. The number of samples is five for each saturation condition and in total 20 samples were tested. The details of sample preparation, testing conditions and results are reported in Jacobsson and Bäckström (2005).

5.4.2 Simulating tests of samples with different fluid saturation

In this study, all the 20 diorite sample tests were simulated for calibration of micro-mechanical parameters to investigate the effect of chemical fluids on the mechanical properties of rocks, using the calibration method as introduced in section 5.2.3. It should be noted that no fluid was present during these calibrations.

Tables 5.4 and 5.5 show the calibration results and the list of microscopic parameters for the selected six samples (with different saturation conditions) adopted in this study to characterize and compare the microscopic behaviour of the diorite rock with different fluid saturation conditions, respectively. The micromechanical parameters obtained from the calibrations for all samples are also compared in Fig. 5.9. Table 5.4 lists the measured and derived equivalent macro-mechanical properties, which were calibrated using the list of micro-mechanical parameters as shown in Table 5.5. These calibrated micro-mechanical parameters can then be used for predictive simulations of rock failure. By comparing micro-mechanical parameters, as shown in Fig. 5.9, the values of microscopic parameters vary even under the same saturation condition and this variation is interpreted as a result of the difference in the micro-structures of the rock samples. However this variation becomes more significant for the rock samples saturated by distilled water or saline formation water. This may be due to the chemical effects of fluids on the mechanical properties of rocks, especially the Young's modulus for contact and bond and bond strengths. The reduction of the uniaxial compressive strength with fluids observed during the laboratory experiments may be interpreted as chemical weakening of the contact bond's normal and/or shear strength. However, a clear trend cannot be observed for the effect of salinity and saturation time on the micro-mechanical parameters in these results.

5.5 Predictive simulations of complete stress-strain curves of Äspö diorite core samples

Complete stress-strain curves for rock samples under uniaxial compressive tests are important for understanding failure mechanisms of the rock. Due to practical difficulties, geometrical and mechanical changes of the samples cannot be readily visualized and examined during such tests without stopping the tests and disturbing the samples.

Table 5.4. Calibration results for selected samples

	Dry_18	Saline_ 13	Distilled 40_24	Distilled 90_07	Formation 40_30	Formation 90_20
Sample size (Diameter [mm] / length [mm])	50.8/ 125.4	51.0/ 127.1	50.8/ 125.5	50.8/ 125.3	50.7/ 127.8	50.8/ 128.1
Young's modulus[GPa]	71.07 (70)	67.96 (68)	71.94 (72)	68.06 (68)	72.77 (73)	67.08 (67)
Poisson's ratio	0.290 (0.29)	0.298 (0.3)	0.337 (0.34)	0.310 (0.3)	0.300 (0.3)	0.322 (0.33)
Uniaxial compressive strength [MPa]	294.24 (295)	235.27 (234)	279.26 (279)	275.10 (275)	297.74 (298)	264.47 (264)
Brazilian tensile strength [MPa]	61.12 (-)	53.66 (-)	61.42 (-)	59.62 (-)	61.03 (-)	65.03 (-)
Unconfined crack initiation strength [MPa]	227.36 (-)	182.18 (-)	209.97 (-)	200.13 (-)	215.93 (-)	185.84 (-)

Values: PFC^{2D}model (lab. experiment)
Minus sign in the round bracket means that measurement was not performed.
Dry_ and Saline_ + Sample number, and Distilled_ and Formation_+ saturation days + sample number

Table 5.5. Microscopic parameters of PFC^{2D} model for selected samples

	Dry_ 18	Saline_ 13	Distilled 40_24	Distilled 90_07	Formation 40_30	Formation 90_20
Ball Density [kg/m^3]	2670	2670	2670	2660	2680	2660
Minimum ball radius [mm]	0.35	0.35	0.35	0.35	0.35	0.35
Ball size ratio	1.5	1.5	1.5	1.5	1.5	1.5
Number of balls	8898	9055	8905	8891	9501	9090
Ball-ball contact Young's modulus [GPa]	70	74	85	73	76	79
Ball stiffness ratio	4	5	6	5	4.5	6
Young's modulus of parallel bond [GPa]	70	74	85	73	76	79
Parallel bond stiffness ratio	4	5	6	5	4.5	6
Particle friction coefficient	0.5	0.5	0.5	0.5	0.5	0.5
Parallel bond normal strength, mean [MPa]	502	485	630	550	567	628.5
Parallel bond normal strength, std. dev [MPa]	0	0	0	0	0	0
Parallel bond shear strength, mean [MPa]	125.5	97	105	110	126	104.75
Parallel bond shear strength, std. dev [MPa]	0	0	0	0	0	0

In this study, predictive numerical simulations of uniaxial compressive tests for Äspö diorite core samples are performed. The basic assumption about the test condition in the modelling is that the samples undergo monotonic uniaxial compression with controlled monotonic increase of axial strain without unloading or addition of lateral strain constraints, such as is normally required to test the existence of Class II behaviour of rocks. The reason for choosing such a test process is that the actual data about the lateral constraint condition of the Äapö diorite core samples during the cyclic uniaxial compression tests was not available at the time when this predictive simulation was performed. Since the tested Äspö diorite samples exhibited Class II-like behaviour, the PFC simulations presented in this chapter attempted to investigate the possibilities of Class I behaviour under monotonic axial strain control through numerical modelling.

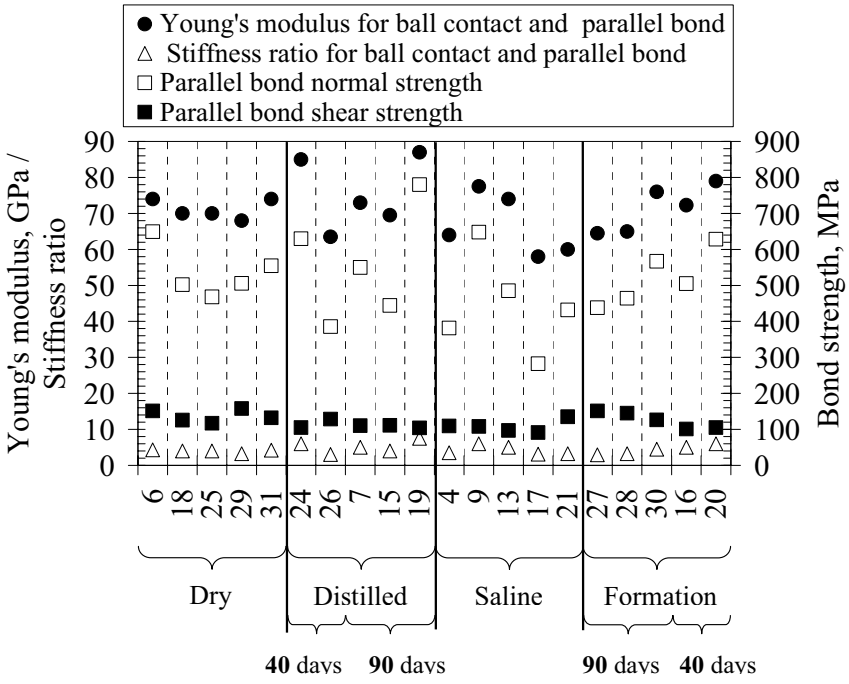

Figure 5.9. Comparison of calibrated micro-mechanical parameters for PFC^{2D} model among different saturation conditions.

Figure 5.10 shows the complete stress-strain curves for all samples at dry and different fluid saturation (distilled, saline and formation water) conditions, when monotonic increase of the axial strain condition was assumed. Typical Class I behaviour was generated, in sharp contract with the Class II-like behaviour shown in Chapter 2. Figure 5.11 shows the predicted progressive evolutions of micro-cracks and contact force distributions for one of the dry samples and samples saturated with formation water for 90 days at different axial strain and stress levels (0.3 % strain, peak stress and 0.6 % strain). Micro-cracks are initiated at about 70% of the peak stress at an axial strain of about 0.3 %, as proposed in Martin and Chandler (1994), and continued to increase, grow and coalescence at local places over the whole sample, while the contact forces (in the vertical direction) remain continuously and uniformly distributed until the peak stress is reached. Up to this point, although local failures occurred, the sample as a whole is remains intact with uniformly mobilized bearing capacities at almost all its elements. This behaviour changed suddenly when the peak stress was passed. The number of crack initiations increases rapidly and localized at specific locations into continuous shear bands, corresponding to an even more localized distribution of contact force chains, indicating a sudden loss of load bearing capacitiy by a large part of the sample, thus the decrease of the vertical load. The trend continues until the rock core sample breaks down completely into several individual structural pieces and the contact force is completely lost. The formation of multiple shear-band-like localization zones appeared to be the main behaviour of damage and failure. Because in practice it is very difficult to obtain a visualized observation of the mesoscopic behaviour of the Äspö diorite samples tested in the laboratory, it is not possible to compare the qualitative validity of this modelled behaviour.

The prediction indicates that when monotonic uniaxial strain control is applied, Class I behaviour with multiple shear-bands, is also one of the possible stress-strain behaviours of the Äspö diorite.

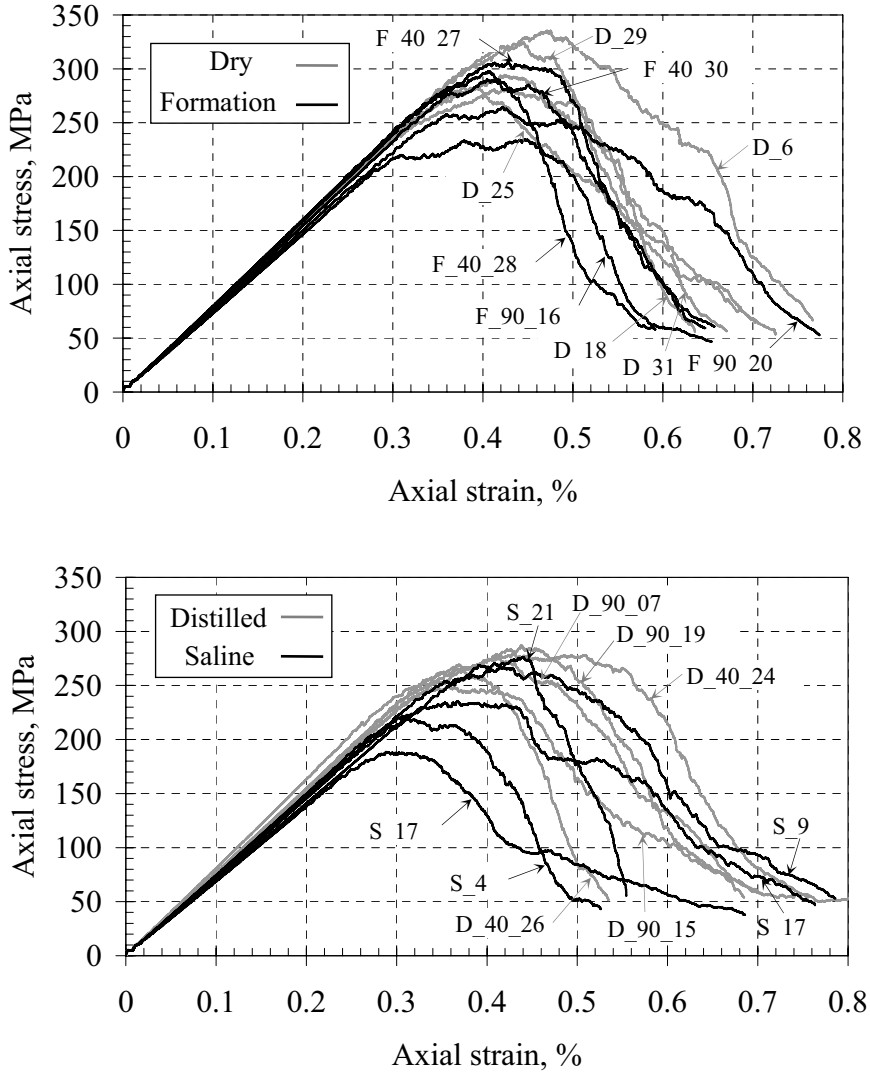

Figure 5.10. The complete stress-strain curves for Äspö diorite samples with different saturation conditions and their comparison.

5.6 Discussion

A number of issues about rock sample testing and result interpretation need to be further discussed:

a) Rock sample testing

ISRM (International Society for Rock Mechanics) suggested the standard method for obtaining the complete stress-strain curves in uniaxial compression (Fairhurst and Hudson, 1999), recommending that test specimens should be right circular cylinders having a height-to-diameter ratio of between 2.0 and 3.0 and a diameter preferably of not less than approximately 50 mm. The diameter of the specimen should be at least 20 times the largest grain in the rock microstructure.

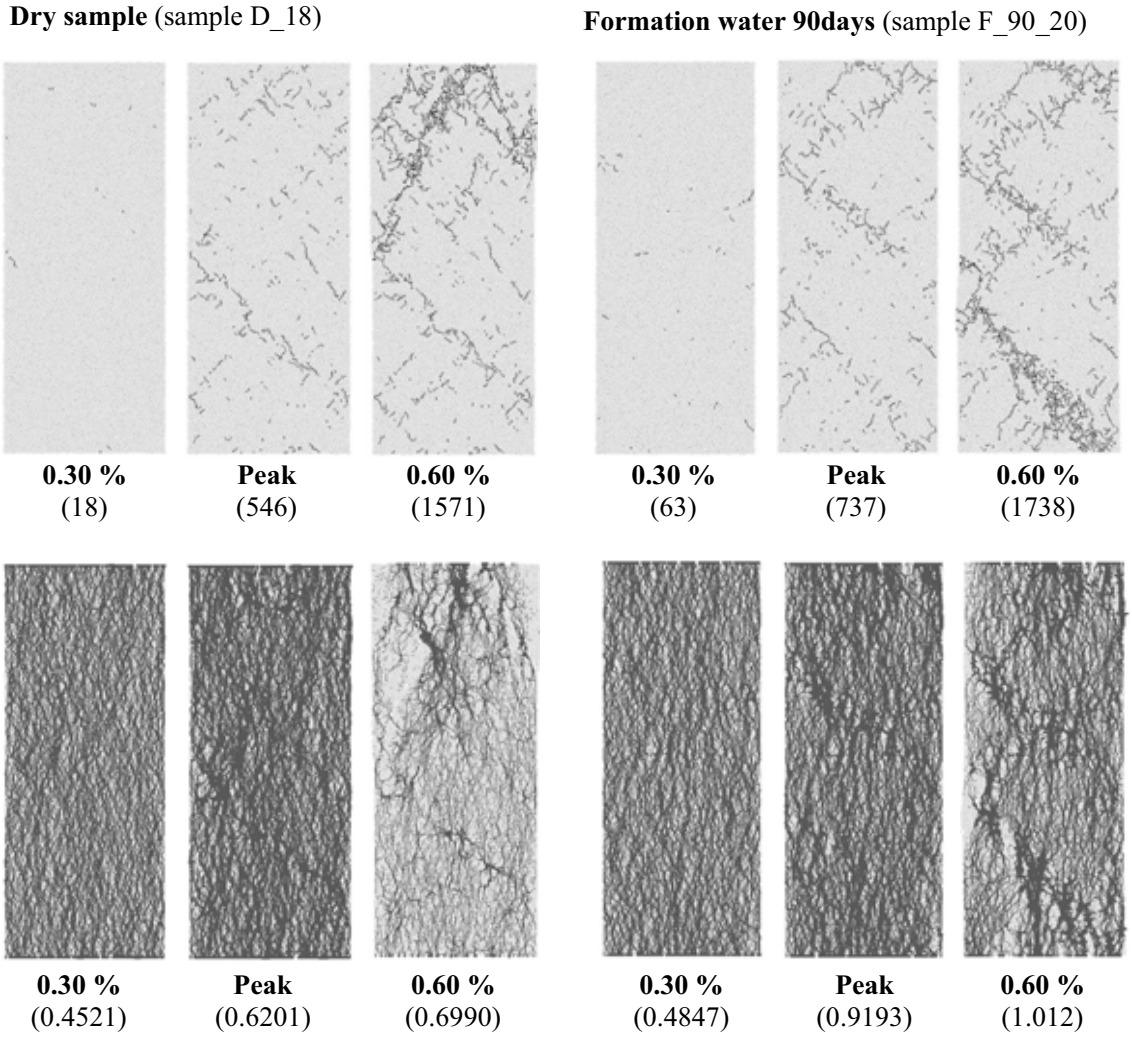

Figure 5.11. The fracture evolution (first row) and contact force distribution (second row) at before peak (0.3% strain), peak and after peak (0.6% strain) for the samples at dry condition and at saturation by formation water for 90days, respectively. The values in the round brackets are number of the micro-cracks and maximum contact force (unit: MN), respectively.

The REV size investigation using particle mechanics models in this study shows that for the diorite at Äspö, Sweden, the REV size can be chosen as 5 cm with a 5 % of acceptable variation. This REV size coincides with the minimum specimen size suggested by ISRM with the ratio of the sample diameter over largest grain size more than 30. Hence, the minimum size of specimen suggested by ISRM is acceptable. Since the REV size will increase with more heterogeneous rocks with large grain size distributions, larger specimens should be prepared for the laboratory uniaxial compressive test so as to keep the same acceptable variation level. For example, the REV sizes for Case III in this study are 7 cm and more than 10 cm with 5% and 3 % of acceptable variation, respectively. In practice, the minimum rock core sample diameter is sometimes taken as a standard dimension without realizing that this may or may not be adequate, depending on the actual grain size distributions.

On the other hand, many particle mechanics application models do not consider the

importance of particle size on the results and the calibrated micromechanical parameters. The approach is often used for models of tens or hundreds of metres, or even kilometres, scale with large diameter particles without checking whether such simplifications can represent adequately the physical behaviour of the rocks. Due to the very nature of the particle mechanics methods, they are more suitable for microscopic or quasi-microscopic scale studies rather than large scale and quantitative engineering applications that require more comprehensive and systematic system characterization and parameterization.

(2) Rock failure mechanism

The predicted Class I behaviour of the Äspö diorite samples indicates that both Class I and Class II behaviour may be possible, depending on specific testing processes and lateral boundary control methods, as shown by this prediction and the actual cyclic normal compression testing results presented in Chapter 2.

3) Modelling the rock behaviour

The sudden change in rock behaviour around the peak stress on a complete stress-strain curve, from material behaviour before the peak into the structural behaviour after the peak, is an important subject in rock mechanics. Both continuum-based and discrete element-based numerical approaches have been applied to modelling such behaviour changes. Strain softening, strain localization and general damage mechanics approaches have been successful modelling tools, but with considerable computational cost spent on system geometry re-configuration to maintain the material continuity and displacement consistency conditions. When continuous shear bands are formed and large displacement discontinuity occurs along and across such bands, maintaining material continuity and displacement consistency along and across the shear bands is difficult when continuum models are applied. System re-configuration about the element connectivity topology in and around the shear bands has to be undertaken. This is especially difficult when the complete breakdown of the rock is present. The discrete particle models can simulate both the equivalent stress-strain behaviour and complete system breakdown without requiring fundamental changes to material models or system re-configuration, but have limitations in computing power for large scale engineering applications. Therefore, hybrid approaches, using the discrete particle models for small but representative scale simulations for deriving REV size and representative material models and parameters that can be adopted by the continuum-based approaches for large scale applications, could be a more realistic modelling approach.

4) Chemical effect

From this study, a clear trend cannot be observed for the effect of salinity and saturation time on the micro-mechanical parameters in these calibration results. This is due to the lack of proper testing and evaluation of chemical effects on the limited number of the diorite samples and different waters (distilled, saline and formation waters) both before and after the testing. Longer-term experiments and careful monitoring of geochemical variations of both the rock samples and fluids before and after the testing are necessary to observe the chemical effects on the mechanical properties of intact rocks.

5.7 Summary and Conclusions

In this study, equivalent microscopic mechanical properties of an intact rock and the effect of different model sizes and particle size distributions are systematically investigated, and the microscopic failure process of rock following a complete stress-strain curve during the uniaxial compressive test with monotonic increase of axial strain was simulated using a particle mechanics approach. The findings obtained from this study are summarized as follows.

- The variation of the calculated mechanical properties decreases significantly as the size of the particle models increase, which justifies the existence of a REV of 5 cm with 5 % acceptable variations.
- The particle size distribution affects the determination of REV size. The REV size increases as the particle size distribution becomes more heterogeneous.
- The 5 cm minimum diameter suggested by ISRM for rock specimens for uniaxial compression tests of rock is reasonable for the Äspö diorite studied in this paper. However, care should be taken when testing different rocks of different grain size distributions.
- For large engineering applications using particle mechanics approaches, care should be taken over the effects of the particle system model size and the particle size distributions on the calibrated particle contact models and parameters, since they cannot be directly measured. Blind adoption of model size and particle diameters without proper examination of their impacts on the system behaviour may lead to unknown uncertainty in the results and its implications.
- Particle mechanics approach can easily simulate the complex bifurcation process in pre-and-post peak stress behaviour of intact rocks with ready visualization of the whole process of crack initiation, growth, coalescence, localization and complete breakdown, without requiring continuous system re-configuration such as is required when the continuum-based modelling approaches are used, since material continuity and displacement consistency conditions are not necessary in the discrete particle models. On the other hand, extending this approach for large scale engineering applications requires equally extensive system characterization and parameterization works for realistic modelling and uncertainty evaluation. Hybrid discrete-continuum models are recommended to overcome the disadvantages of both approaches.
- The weakening of rock strength due to the effect of fluids can be expressed as a weakening of the contact bond.
- Existence of both Class I and Class II behaviour of Äspö diorite rock is possible.

In this study, the micro-mechanical parameters were calibrated using only the elastic part of stress-strain curve obtained from the experiments (Young's modulus, Poisson ratio and uniaxial compressive strength) and all simulations for the rock core sample breakdown under uniaxial compression presented in Section 5.5 are predictive (see Fig. 5.10). The PFC approach can be applied to simulate both Class I and Class II behaviour.

The grain/particle size distribution is sensitive to the REV size. In this study, the minimum/maximum particle radii were assumed due to the lack of data for actual grain size distributions of the tested samples, which requires special testing techniques, such as SEM with thin section analysis (Hallbauer *et al*. 1973).

Acknowledgement

The work performed is financed by Swedish Nuclear Power Inspectorate (SKI).

References

Adachi, T., Oka, F. and Koike, M. *An elasto-viscoplastic constitutive model with strain-softening for soft sedimentary rocks*. Soils and Foundations, 2005; 45(2): 125-133.

Al-Busaidi A, Hazzard JF and Young RP. 2005. *Distinct element modeling of hydraulically fractured Lac du Bonnet granite*. J Geophys Res, 110:B06302, doi:10.1029/2004 JB003297.

Aoki, K., Mito, Y., Mori, T., Morioka, H. and Maejima, ?. *Evaluation of behavior of EDZ around rock cavern by AE measurement and DEM simulation using bonded particle model*. In: Contribution of Rock Mechanics to the New Century, Proc 3rd Asian Rock Mech Symp, eds. Ohnishi Y and Aoki K, Millpress, Rotterdam, p. 327-333. 2004.

Cundall, P. A. *A discontinuous future for numerical modeling in geomechnics?* Geotech Eng, 2001; 149(1): 41-47.

Golshani, A., Okui, Y., Oda, M. and Takemura, T. *A micromechanical model for brittle failure of rock and its relation to crack growth observed in triaxial compression tests of granite*. Mechanics of Materials, 38(2006): 287-303.

Hallbauer, D. K., Wagner, H. W. and Cook, N. G. W. 1973. *Some observations concerning the microscopic and mechanical behaviour of quartzite specimens in stiff, triaxial compression tests*. Int J Rock Mech Min Sci & Geomech. Abstr., 10(1973), 713-726.

Itasca Consulting Group. *PFC^{2D} User's manual, Ver.3.0*, Minneapolis, Minnesota. 2003.

Jacobsson, L. and Bäckström, A. *Äspö Hard Rock Laboratory, DECOVALEX, Uniaxial compression tests of intact rock specimens at dry condition and at saturation by three different liquids: distilled, saline and formation water.* International Progress Report, IPR-05-33, Swedish Nuclear Fuel and Waste Management Co (SKB). 2005.

Martin, C. D. and Chandler, N. A. *The progressive fracture of Lac du Bonnet Granite*. Int J Rock Mech Min Sci Geomech Abstr., 1994; 31(6):643-659.

Potyondy, D. O. and Cundall, P.A. *A bonded-particle model for rock.* Int J Rock Mech Min Sci, 2004; 41(8): 1329-1364.

Seto, M., Vutukuri, V. S., Nag, D. K. and Katuyama, K. *The effect of chemical additives on the strength of rock*. JSCE Journal of Geotechnical and geoenvironmental Engineering, 1998;603/III-44:157-166 (in Japanese)

Tannant, D. D. and Wang, C. *Thin tunnel liners modeled with particle flow code*. Engineering Computations, 2004;21(2/3/4): 318-342.

Wang, C., Tannant, D. D. and Lilly, P. A. *Numerical analysis of the stability of heavily jointed rock slopes using PFC2D*. Int. J. Rock Mech. Min. Sci., 2003;40(3): 415-424.

6. Numerical simulation of core tests using FRACOD

M. Rinne and B. Shen
Fracom Ltd, Finland.

6.1 Introduction

FRACOD is a two-dimensional computer code which is based on the Displacement Discontinuity Method (DDM) principles (Crouch, 1976). A rock discontinuity (grain boundary, crack, joint, fracture etc.) is simulated by using DDM elements for opposite surfaces of the discontinuity. The model predicts the explicit fracturing process including fracture initiation, fracture sliding/opening and fracture propagation. Both shear and tensile failures are considered (Shen et al. 2005).

6.1.1 Fracture initiation

Fracture initiation starts from microcrack formation. With increasing stress the microcracks coalesce and finally form macro-fractures. FRACOD considers the intact rock as a flawless and homogeneous medium. Rather than describing the micro-scale process in a structure, it focuses on whether a macro-fracture will form at a given location and stress state. When the tensile stress at a given point exceeds some predefined portion of the tensile strength of the intact rock, a potential failure surface will be implemented in the model and it takes the direction perpendicular to the tensile stress. For shear failure, cohesion and friction angle are used to define the potential failure plane according to the Mohr-Coulomb criterion. Intact rock strength properties are usually applied for these new discontinuities. When the local stress exceeds the strength of such a plane, it will slip or open and its cohesion drops to zero. After a local failure we call such a discontinuity a newly initiated crack.

It is known that fracture initiation starts at a stress level far below the ultimate short-term strength and increases with stress. FRACOD uses a probabilistic approach to simulate fracture initiation. It is assumed that, at a candidate location, the probability of a fracture initiation depends upon the stress/strength ratio (σ/σ_m):

$$p = 0; \qquad if\left(0 \le \frac{\sigma}{\sigma_m} \le a\right) \tag{6.1}$$

$$p = \frac{1}{(1-a)^2}\left[\frac{\sigma}{\sigma_m} - a\right]^2; \qquad if\left(a \le \frac{\sigma}{\sigma_m} \le 1.0\right) \tag{6.2}$$

$$p = 1.0; \qquad if\left(\frac{\sigma}{\sigma_m} > 1.0\right) \tag{6.3}$$

where p = probability of fracture initiation; σ/σ_m = ratio of the stress to strength and a= fracture initiation level.

6.1.2 Fracture state

The normal and shear displacement of the existing and new fractures are predicted and recorded during the failure process. The state of each crack (joint) element can be determined using the Mohr-Coulomb failure criterion:

(1) open joint: $\sigma_n > 0$
(2) elastic joint: $\sigma_n < 0, \mid \sigma_s \mid < c + \mid \sigma_n \mid tan\phi$
(3) sliding joint: $\sigma_n < 0, \mid \sigma_s \mid \geq c + \mid \sigma_n \mid tan\phi$

where a compressive stress is taken to be negative and c is cohesion. If the joint has experienced sliding, $c = 0$. The code is recently modified to predict the fracture aperture using the normal displacement of the fractures.

6.1.3 Fracture propagation

In rock masses both tensile (mode I) and shear failure (mode II) are common. The original G-criterion by Griffith has been improved and extended by Shen and Stephansson (1993) who suggested a fracture propagation criterion, named the F-criterion. It involves both mode I and mode II fracture propagation. According to the F-criterion, in an arbitrary direction (θ) at a fracture tip there exists an F-value, which is calculated by

$$F(\theta) = \frac{G_I(\theta)}{G_{Ic}} + \frac{G_{II}(\theta)}{G_{IIc}} \tag{6.4}$$

where G_{Ic} and G_{IIc} are the critical strain energy release rates for mode I (tensile) and mode II (shear) fracture propagation. $G_I(\theta)$ and $G_{II}(\theta)$ are strain energy release rates due to the potential mode I and mode II fracture growth of a unit length. If the maximum F value reaches 1.0, fracture propagation will occur. The direction of fracture propagation will correspond to the direction where F reaches the maximum value. The sum of normalized G-values is used to determine the failure load and its direction. G_I and G_{II} can be expressed as follows (Fig. 6.1): if a fracture grows a unit length in an arbitrary direction and the new fracture opens without any surface shear dislocation, the strain energy loss in the surrounding body due to the fracture growth is G_I. Similarly, if the new fracture has only a surface shear dislocation, the strain energy loss is G_{II}.

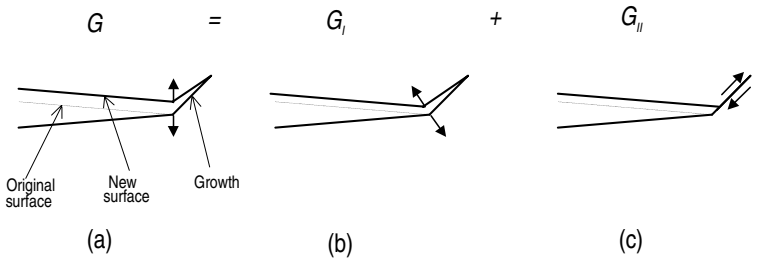

Figure 6.1. Definition of G_I and G_{II} for fracture growth. (a) G, the growth has both open and shear displacement; (b) G_I, the growth has only open displacement; (c) G_{II}, the growth has only shear displacement.

6.1.4 Fracture propagation using DDM

The key step in using the F-criterion is to determine the strain energy release rate of mode I (G_I) and mode II (G_{II}) at a given fracture tip. As G_I and G_{II} are only the special cases of G, the task is then how to use DDM to calculate the strain energy release rate G. The G-value, by definition, is the change in the strain energy of a linear elastic body when the crack has grown one unit of length. Therefore, to obtain the G-value the strain energy must first be estimated. By definition, the strain energy, W, in a linear elastic body is

$$W = \iiint_v \tfrac{1}{2}\sigma_{ij}\varepsilon_{ij}dV \tag{6.5}$$

where σ_{ij} and ε_{ij} are the stress and strain tensors, and V is the volume of the body. The strain energy can also be calculated from the stresses and displacements along its boundary

$$W = \tfrac{1}{2}\int_s (\sigma_s u_s + \sigma_n u_n)ds \tag{6.6}$$

where σ_s, σ_n u_n, u_s are the stresses and displacements in tangential and normal directions along the boundary of the elastic body. Applying eq. (6.6) to the crack system in an infinite body with far-field stresses in the shear and normal direction of the crack, $(\sigma_s)_0$ and $(\sigma_n)_0$, the strain energy, W, in the infinite elastic body is

$$W = \tfrac{1}{2}\int_0^a \left[\left(\sigma_s - (\sigma_s)_0\right)D_s + \left(\sigma_n - (\sigma_n)_0\right)D_n\right]da \tag{6.7}$$

where a is the crack length, D_s is the shear displacement discontinuity and D_n is the normal displacement discontinuity of the crack. When DDM is used to calculate the stresses and displacement discontinuities of the crack, the strain energy can also be written in terms of the element length (a^i) and the stresses and displacement discontinuities of the ith element of the crack.

$$W \approx \frac{1}{2}\sum_i \left(\overset{i}{a}(\overset{i}{\sigma}_s - (\overset{i}{\sigma}_s)_0)\overset{i}{D}_s + \overset{i}{a}(\overset{i}{\sigma}_n - (\overset{i}{\sigma}_n)_0)\overset{i}{D}_n\right) \tag{6.8}$$

The G-value can be estimated by

$$G(\theta) = \frac{\partial W}{\partial a} \approx \frac{\left[W(a+\Delta a) - W(a)\right]}{\Delta a} \tag{6.9}$$

where $W(a)$ is the strain energy governed by the original crack while $W(a+\Delta a)$ is the strain energy governed by both the original crack, a, and its small extension, Δa (Fig.6.2). Both W(a) and W(a+Δa) can be determined by using DDM and eq. 6.9.

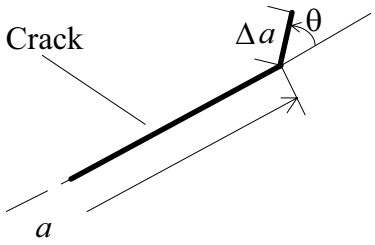

Figure 6.2. A 'fictitious' element is introduced to the tip of the original crack with the length Δa in the direction ϕ.

6.2 Laboratory tests and parameters

Intact rock and fracture properties of Äspö diorite have been defined in the laboratory and reported by Staub et al. (2004), Jacobsson and Bäckström (2005), Backers (2006) and Antikainen (2006). All samples have been taken from the Äspö HRL. The material properties obtained in the laboratory have been applied as input parameters to model the stress–strain response in uniaxial and triaxial compression tests. A set of typical parameters applied in modelling is listed in Table 6.1.

Table 6.1. Input data for numerical simulation of core tests.

PARAMETER	**VALUE AND UNIT**
INTACT ROCK	
Young's modulus	68.0 GPa
Poisson's ratio	0.24
Cohesion	31 MPa
Friction angle	49°
Tensile strength	14.8 MPa
Crack initiation strength (for UCS)	121 MPa
FRACTURES	
Size of a newly initiated crack	3.125 mm
Fracture toughness mode I	3.21 MPa $m^{1/2}$
Fracture toughness mode II. Confinement: 0/5/10/ 15/ 20/ 30 and 50 MPa	4.6/ 7.1/ 8.8/ 10,0/ 10.9/ 11.9/ and 12.7 $MPam^{1/2}$
New crack stiffness: Kn and Ks	26976 GPa/m
Friction angle	49.0°
Cohesion, before and after sliding	31 MPa, 0MPa
Dilation angle	5°
Initial fracture aperture	10μm
Residual fracture aperture	1μm

Considering the post-peak axial deformation behaviour, rock types are classified into Class I and Class II (Fig. 6.3, Wawersik 1968). For class I, fracture propagation is stable, in the sense that additional work must be done on the sample for each incremental decrease in load-carrying ability. For class II, failure is unstable or self-sustaining: to control fracture, elastic energy must be extracted from the material.

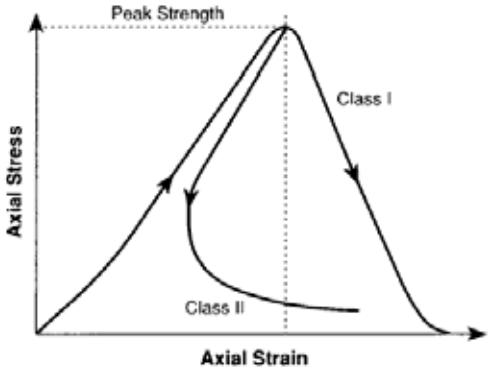

Figure 6.3. Rock types are classified into Class I and Class II in view of the post-peak axial deformation behaviour (Wawersik, 1968).

Uniaxial (UCS) and triaxial compression tests were carried out with a digitally servo-controlled MTS 815 rock mechanics test system at Helsinki University of Technology (HUT). Test specimens were prepared and tested according to the ISRM suggested method. Compression tests were started with axial load control and changed to radial strain rate control after -0.01% radial strains but before crack initiation stress. This enables control of the post failure phase even for Class II behaviour. Because of the radial strain rate control, the axial loading rate decreases to zero and changes sign at the peak strength (Fig. 6.4).

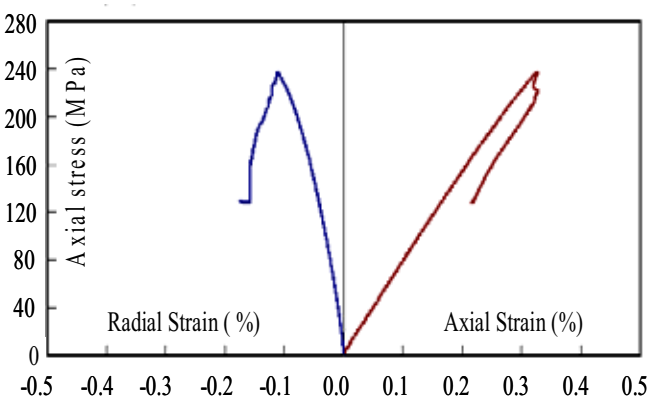

Figure 6.4. Typical stress-strain curve from a uniaxial compression test of Äspö diorite (Staub et al. 2004).

In FRACOD models the fracture toughness and the crack length are the most important factors defining the level of stress at which the crack starts to propagate. Fracture toughness of Äspö diorite has been determined using the ISRM suggested method for mode I, and the Punch-through Shear Test for model II (Backers, 2003). According to these tests, mode II fracture toughness increases with increasing confining pressure and shows an asymptotic rise to a maximum value.

In practice it is not possible to precisely determine the crack length and orientation of the most critical crack from a rock sample. Numerical sensitivity analyses have been made with varying crack lengths. The smaller the crack, the higher the stress needed to trigger fracture propagation. In this study a crack length of 3.125 mm has been used as a crack initiation length. The size of an initiated crack is equivalent to that of the largest flaws in the material, which under increasing load, will be the earliest to reach the critical stress intensity for fracture propagation.

6.3 Intact rock model

The stress and strain changes can be monitored at any point of the numerical model during the loading–unloading process. In this study the stress is monitored on the top of the sample. The radial response is monitored at four locations of the vertical boundary (Fig. 6.5). Applying axial strain on the top boundary increases the stress. Axial strain of ($2x10^{-6}$ m or 0.0016%) was applied in each small step, which is equivalent to about 1 MPa stress increase in the elastic region.

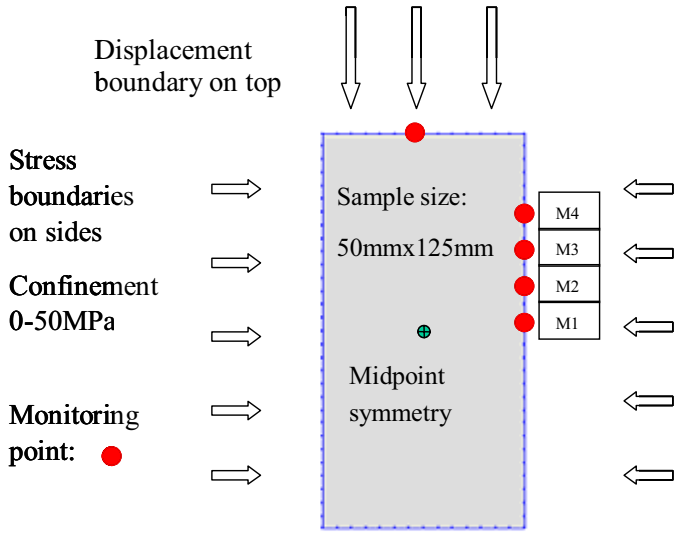

Figure 6.5. Loading configuration for FRACOD^{2D} core test simulations.

Five calculation cycles were used for every loading step to detect possible fracture propagation. The same monotonic axial "loading rate" was applied throughout the calculations. To demonstrate the Class II behaviour, reversal axial strain was applied during unstable fracture propagation.

6.3.1 UCS model

The modelling work was aimed at simulating the general stress-strain behaviour observed in uniaxial compressive strength (UCS) tests of Äspö diorite. Here the fracture initiation is set to start at a stress level of 121 MPa of uniaxial loading, as a typical value for Äspö diorite (FI), see Fig. 6.6.

The number of fracture initiations increases with stress increase. Stable fracture propagations (SF) start at a stress of 225 MPa. When the strain is increased to a level equivalent to the axial stress of 232 MPa (peak strength), unstable fracture propagations (UF) occur. After this moment, the sample moves into the post-peak stage, and failure continues at constant axial strain, resulting in decrease of axial stress.

The progressing failure is detected as increasing radial strain even if the axial strain is kept constant (see Fig. 6.7.). To simulate the Class II behaviour, unloading was started after passing the peak strength using a similar size of strain increments but in the opposite direction as was used for loading. Five calculation cycles were applied for each unloading increment during the unstable phase of fracture propagation.

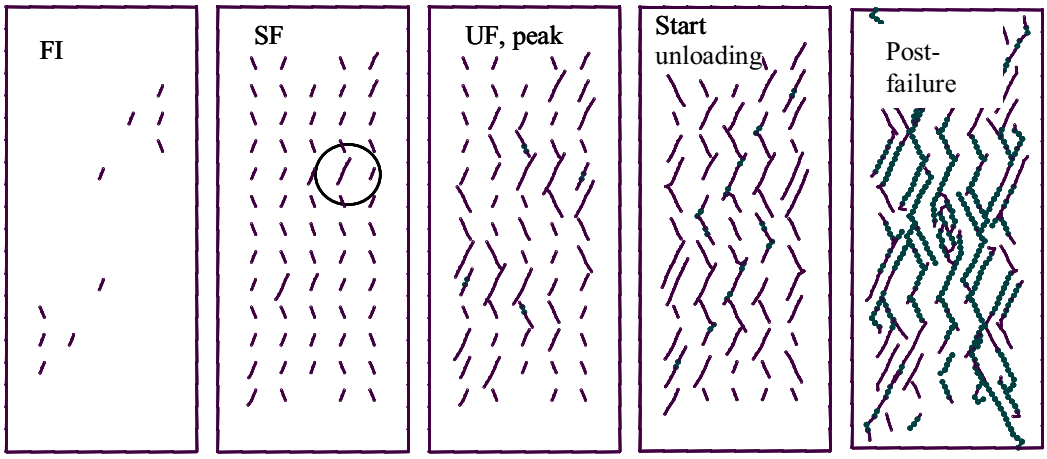

Figure 6. 6. Failure pattern according to FRACOD calculations. Dots mark an open fracture. (FI) fracture initiation, (SF) stable fracture propagation, (UF) unstable fracture propagation.

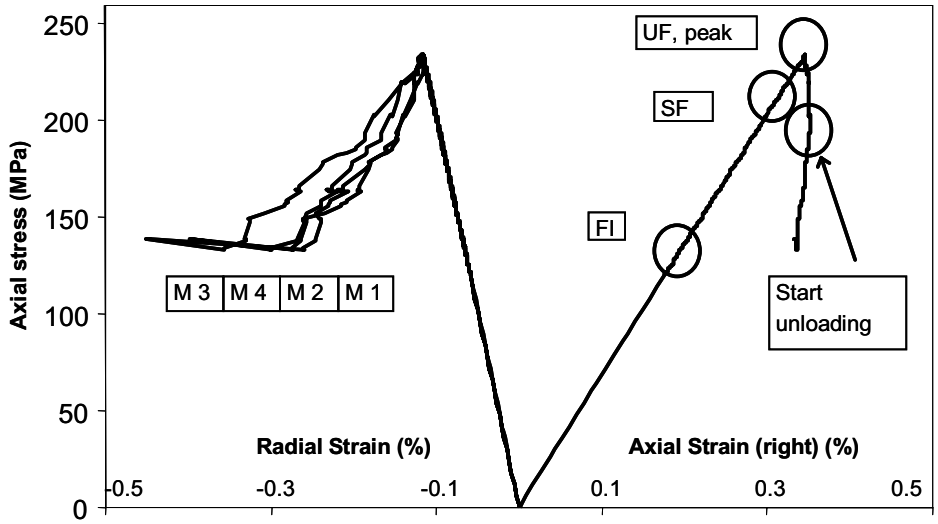

Figure 6.7. Modelled Class II behaviour of Äspö diorite.

6.3.2 Triaxial models

The effect of confinement on peak strength was modelled using similar parameters and loading increments as described for the UCS model with an exception that a monotonic axial strain loading were applied all the way through the test, that is, no unloading at the peak. The confinement was applied to the sample before axial loading. Confinements of 5, 10, 15, 20, 30 and 50 MPa were modelled and associated fracture toughness values as shown in Table 1 were used.

In the triaxial models the stress level needed for crack initiation increases linearly with increasing confinement because constant cohesion, friction angle and a constant portion (73%) of the Mohr-Coulomb strength criterion have been applied. The stress level to trigger fracture propagation shows an asymptotic behaviour (Fig. 6.8b). Efforts to simulate individual laboratory tests were made. Fig. 6.9 presents a model aiming to replicate accurately the stress-strain response of both axial and radial strain.

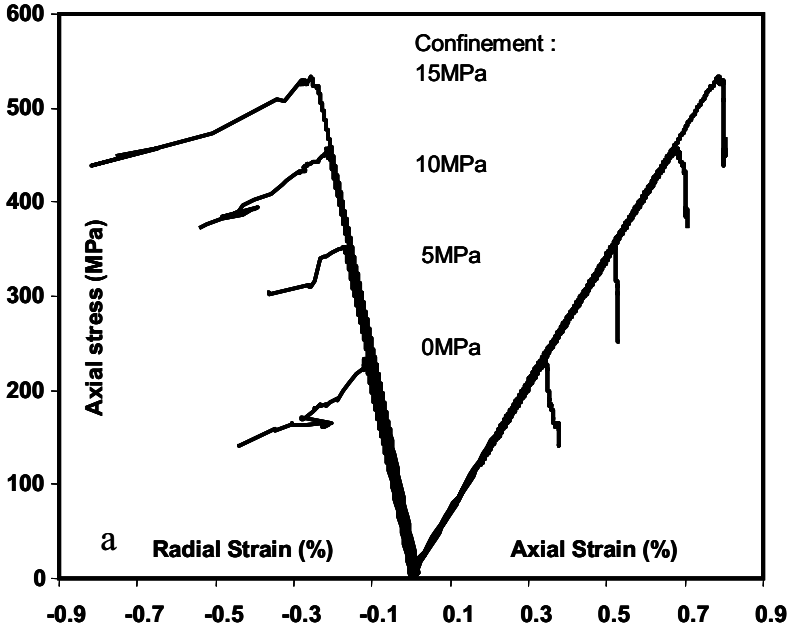

(a)

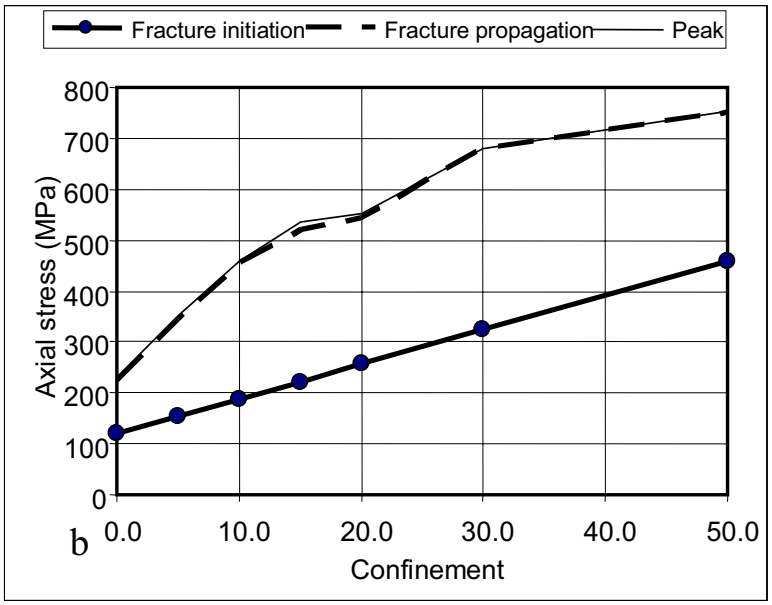

(b)

Figure 6.8. a): Stress strain curves for confined models using monotonic axial loading rate. b): Calculated effect of confinement on fracture initiation, propagation and peak strength.

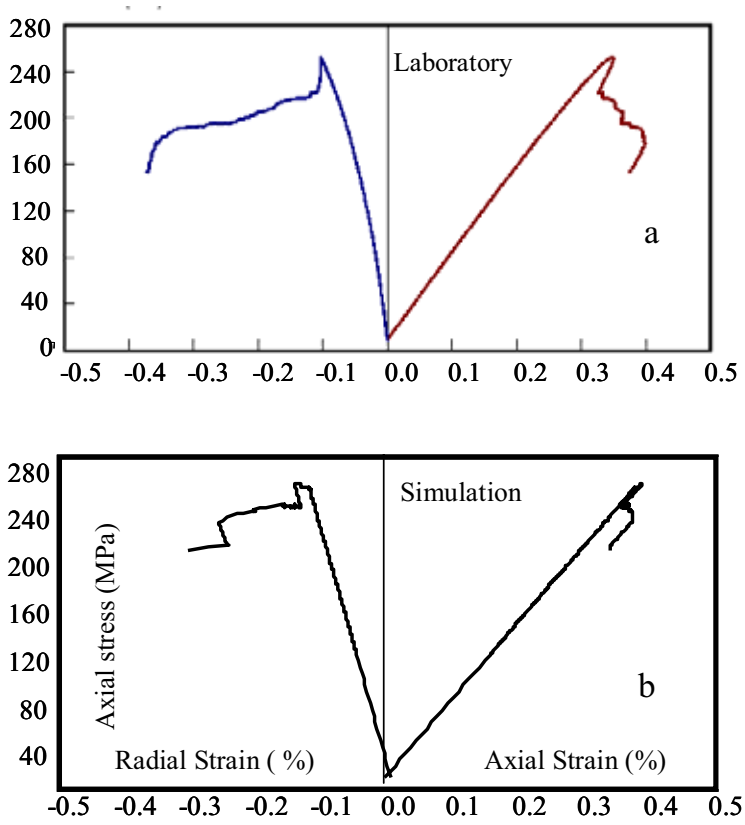

Figure 6.9. a): Radial strain controlled triaxial compression test with 7 MPa confinement (Staub et al., 2004). b): FRACOD simulation.

6.4 Pre-existing fractures and inhomogeneities

A rock sample always contains inhomogeneities which have accumulated in the rock during its geological history. Sample preparation is also believed to introduce damage in the sample. Some preliminary modelling of the effect of pre-damage in rock has been made.

In FRACOD models the effect of heterogeneity can be considered by adding discontinuities like cracks with different orientations, sizes and properties. A number of material regions, for example rock types with different strength and deformation properties, can also be included in the model.

Fig. 6.10 presents the modelled failure pattern of an inclined crack under uniaxial and bi-axial load. a) Pre-defined fracture. b) Tensile fracture propagation. c) Sample splitting. d) Shear movement. e) Aperture and f) Displacements at failure. These particular models are made for demonstrative purpose and the applied material parameters are not Äspö diorite specific. Different material parameters have been applied for the unconfined and confined model.

When an isolated fracture, with a small angle to the major load is modelled, a wing crack will form and the failure takes place in tension (Fig. 6.11b and Fig. 6.12a). Relatively small confinement seems to restrain tensile fracture propagation and favour shear failure when the parameters for Äspö diorite are used.

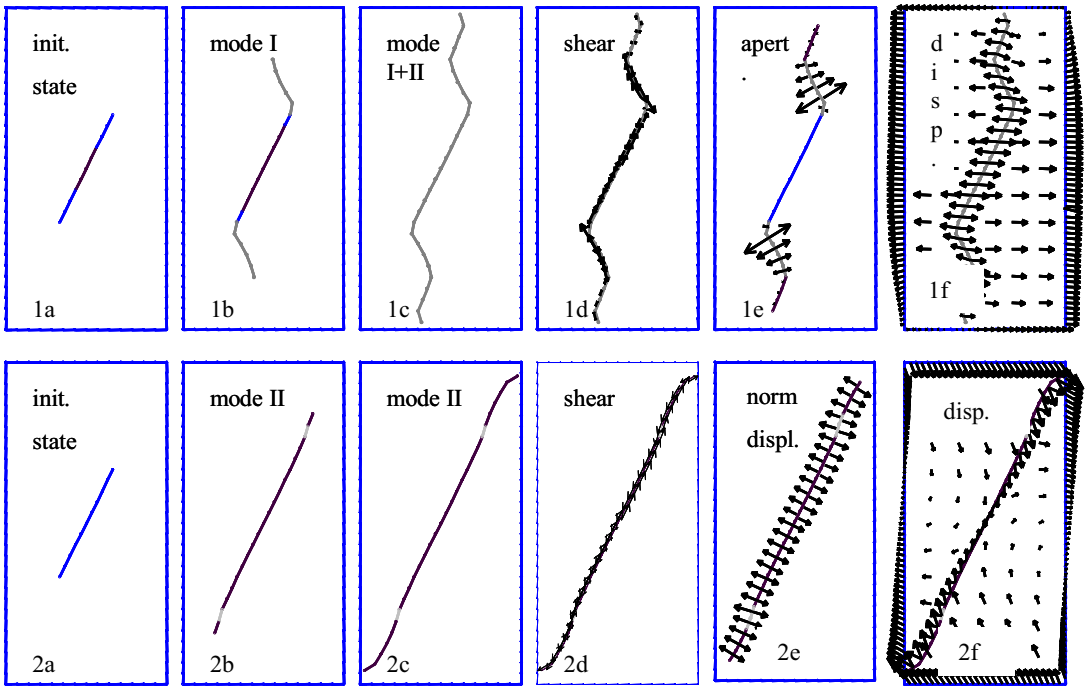

Figure 6.10. Modelled failure pattern in uniaxial load (1 a-f) and with 5MPa confinement (2 a-f).

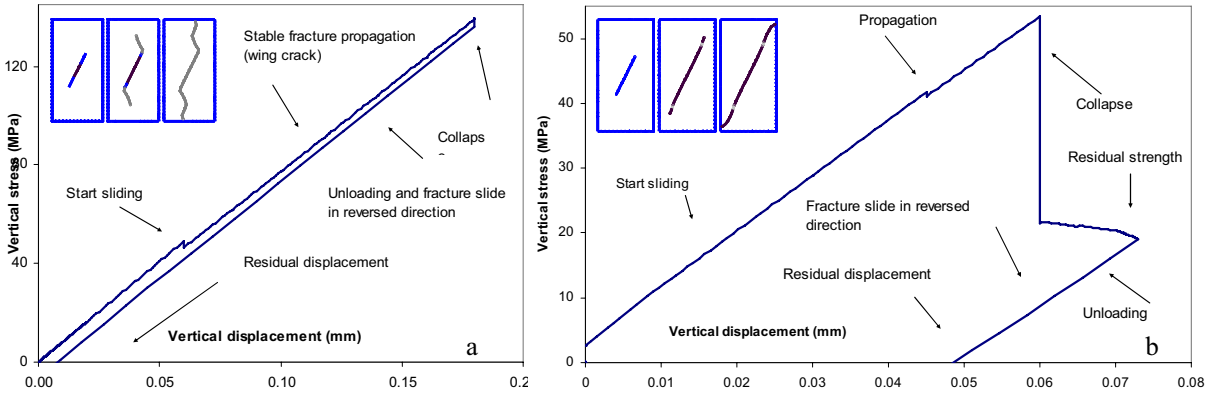

Figure 6.11 Modelled loading – unloading behaviour of an inclined pre-existing crack in compression a): Uniaxial compression. b); Confinement (5MPa).

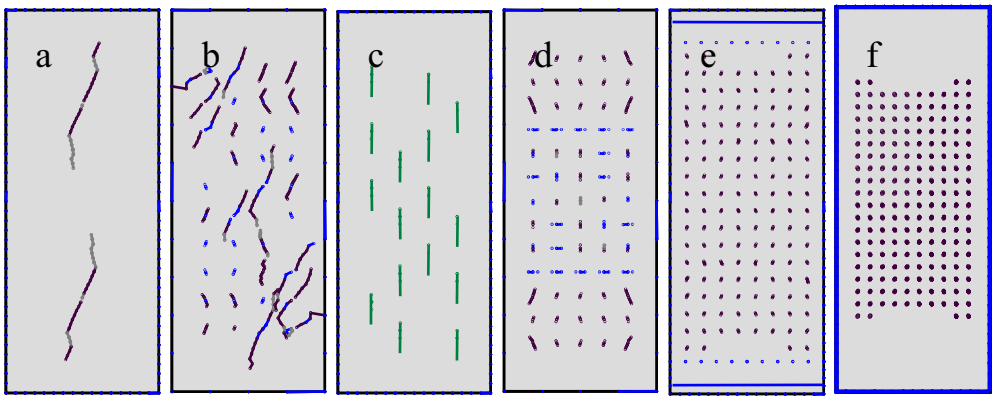

Figure 6.12. Pre-damage introduced in the model.

The rock will remember, at least to some extent, its loading history. Pre-damage can be implemented in the model by defining various geometries and fracture properties for individual fractures (a, b, c in Fig.6.12). Flaws can also be introduced by applying a short term shock load in different directions (model d, e and f in Fig.6.12). The model in Fig.6.12e with horizontal fractures at the top and bottom aims to simulate the stiffness of the loading system.

To study the progressive failure in the laboratory, the so-called damage controlled test can be conduced (Martin, 1997). The minimum value of load to increase the damage in rock is tracked by cycling the load. The locus of damage is a path of the critical stress strain point defined for each loading ramp separately. To test the capacity of the code to model such loading unloading-reloading processes, Äspö rock properties were used for an initially intact specimen. Simulated loading-unloading stress-strain curves are presented in Fig. 6.13. The effect of pre-damage, crack density and loading history will be studied more carefully.

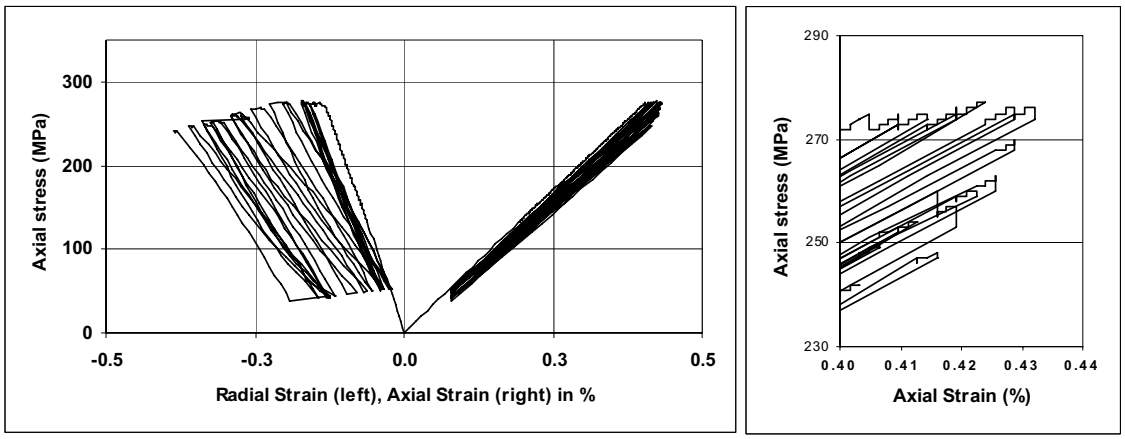

Figure 6.13. Simulated cyclic loading stress-strain curves using Äspö diorite parameters reveals the Class II behaviour.

6.5 Loading rate and time dependency

6.5.1 The conceptual creep model

Classical fracture mechanics postulates that a fracture tip which has a stress intensity factor equal to the material's critical fracture toughness, K_{Ic}, will accelerate when propagating to speeds approaching the elastic wave speed in a medium. However, when the time aspect is considered, fractures can grow at stress intensities significantly below the critical values. This process is termed subcritical fracture growth and propagation velocities can vary over many orders of magnitude as a function of stress intensity. The actual time-dependence of crack growth is due to rate-controlled processes acting at the tips of cracks, where stress concentration exists.

Theoretical studies have been made, aiming to formulate a conceptual model for time dependent mechanical effects on compressed rock mass. Two approaches were investigated. First, a concept based on time-dependent strength reduction utilising the Mohr-Coulomb criterion was evaluated (Rinne, 2004)). This approach aims to model the time-effect by considering the time dependent cohesion reduction and mobilization

of the friction angle in stressed rock. It was concluded that this concept could be used to model the time dependent loosening of rock matrix and to model delayed slip of rock joints. Difficulties were foreseen in laboratory tests to define the long term loading effect on the critical parameters.

The second approach was based on subcritical crack growth principles (Atkinson and Meredith, 1987). It utilises the relation between stress intensity at the crack tip and the crack growth rate (Fig. 6.14). This concept was chosen to be the platform for further studies. One major advantage of this approach over the first one is that there are well established methods to monitor and to characterize subcritical crack growth in the laboratory. In addition, the chemical effects can be considered by including the effects on the subcritical parameters A and n (See eq. 6.10).

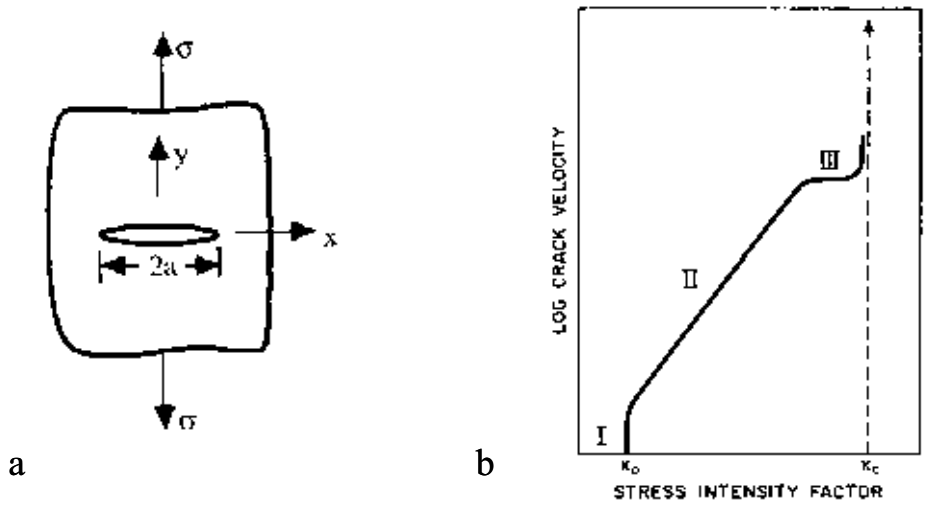

Figure 6.14. a): An infinite plate containing a crack under uniaxial tensile loading. b): Schematic crack velocity/normalized stress intensity factor diagram for subcritical crack growth in rock undergoing stress corrosion. K_0 is the stress corrosion limit. Crack velocity in region II is controlled by the stress corrosion reactions (Atkinson and Meredith, 1987).

An analytical solution was established for the relation between crack length and time. The concept is based on a formula presented by Charles (1958), who stated that most experimental data can be fitted into an expression for subcritical velocity of the form:

$$v = AK^{n} \tag{6.10}$$

where v is the crack velocity, A is a constant, K is the stress intensity factor and n, the stress corrosion or crack propagation factor.

Assuming that the maximum propagation velocity v_{max}, occurs when $K=K_c$, (K_c =critical stress intensity at failure), and by replacing the stress intensity factor K with

$$K = \sigma\sqrt{\pi \times a} \tag{6.11}$$

where σ is the far-field stress and a is the crack half length, we get:

$$v = v_{\max}\left(\frac{\sigma\sqrt{\pi \times a}}{K_c}\right)^n \tag{6.12}$$

The constant crack length must be replaced by an effective crack length:

$$a_{eff}(t) = a_0 + \int_0^t v(t)dt \tag{6.13}$$

By integration we finally get an expression for the crack length at a certain time by:

$$a(t) = \left\{(-n/2+1)\left(\mathrm{v}_{\max}\left(\frac{\sigma\sqrt{\pi}}{K_c}\right)^n \times t + \frac{a_0^{-n/2+1}}{-n/2+1}\right)\right\}^{\frac{1}{-n/2+1}} \tag{6.14}$$

6.5.2 Implementation of the conceptual model into FRACOD

The advantage of FRACOD for fracture creep modelling is that it takes into account existing joints in the rock mass. The model predicts the locus and the direction of creep deformation and creep fracturing in the macro scale. All parameters can be directly measured by laboratory tests and they all have physically sound meanings, derived directly from Linear Elastic Fracture Mechanics (LEFM) and subcritical crack growth theory.

The conceptual model for rock creep has been implemented into the code (Shen, 2005). As a first step, improvement was made to save the stress/ displacement history. The code is now capable of monitoring the stress/displacement history at any point and following the loading path. This aspect has already been used to model the failure of rock samples subjected to uniaxial and triaxial load and to compare the stress/ strain response with laboratory experiments as described in the previous section. Major code modifications have been directed to couple a time marching algorithm and the creep-fracturing concept in the code.

Fig. 6.15 shows the process by which FRACOD simulates creep fracture growth. After the length and the direction of the subcritical crack growth are determined, FRACOD will add new tip elements to the original crack tips. This iteration process will be continued until a designated time is reached or an unstable crack growth is detected (Shen 2005).

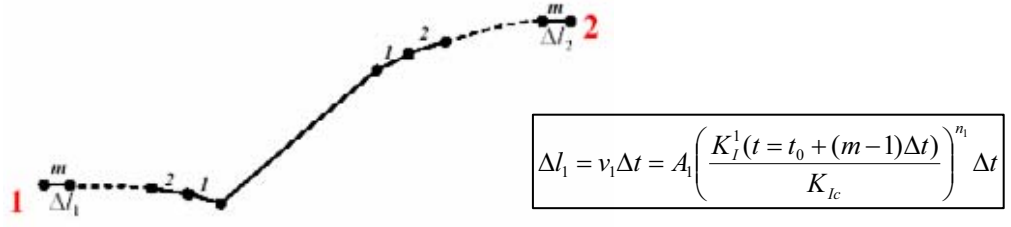

Figure 6.15. Step-by-step process of a creep fracture growth simulated by FRACOD.

6.5.3 Creep code testing

The improved FRACOD code will be used for analysis of creep-fracturing in EDZ using the site specific material properties and rock conditions at Äspö HRL. Preliminary test calculations with the updated creep code have been made. Prior to real data from creep laboratory tests, the accuracy of the numerical approximation have been studied and compared with analytical solutions.

The code testing was initially conducted using tensile failure models. The accuracy of the stress intensity at the fracture tip has been studied using a simple tensile crack model as presented in Fig. 6.16. A crack (l = 0.01m) is loaded perpendicular to a far-field tensile stress of 10MPa. Fig. 6.16a displays the effect of model accuracy on the stress intensity.

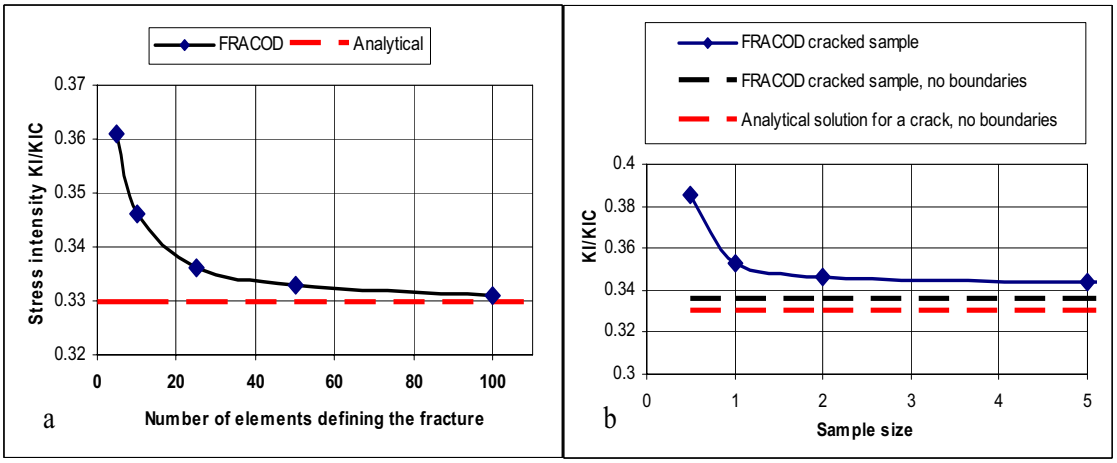

Figure 6.16. a) Model accuracy vs. number of elements in the fracture. b) Stress intensity at the crack tip vs sample size.

The laboratory tests are usually made on fairly small rock samples. The effect of the sample size on stress intensity at the crack tip has been studied using constant crack geometry and varying numerical sample size. The loading configuration is the same as in the previous example, except that the models have finite boundaries. Sample size 1 stands for the standard sample (0.125 m x 0.05 m), sample size 2 has double the length and diameter compared to 1, and so on. Here 25 elements define the fracture and the calculation accuracy. A sample boundary close to a crack tip increases the stress intensity. The size effect becomes significant when the sample dimensions are close to the crack size (Fig. 6.16b).

The accuracy of the time-to-failure (TTF) approximation has been evaluated. A small inaccuracy in the K_I/K_{IC} ratio prior to creep leads to remarkable errors in the TTF approximations. Accuracy of TTF calculations also depends on the resolution of the applied time steps (Fig. 6.17).

The subcritical crack parameters applied here (v_{max}=500 m/s, n=20) are rough estimates and the results can only be used for the purpose of code testing. True factors for Äspö rocks have been defined recently by laboratory tests (Backers, 2006) and additional modelling based on real data will be made.

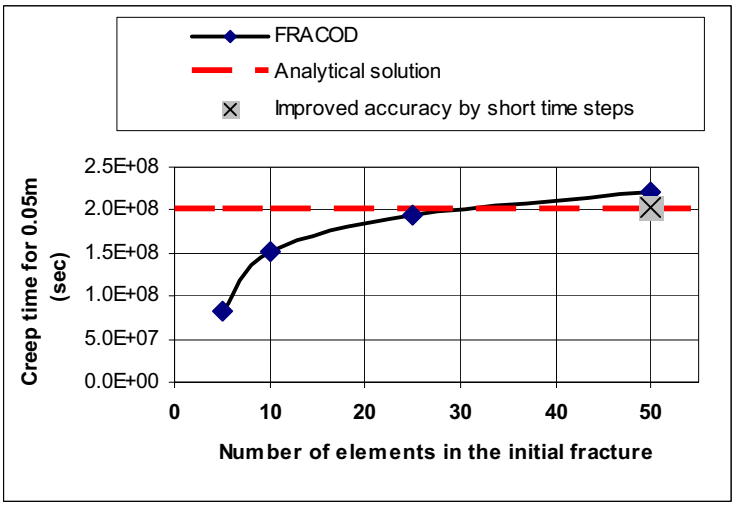

Figure 6.17. Accuracy of time-to-failure approximation.

The capacity of the code to model the stress relaxation caused by creep fracturing is presented in Fig. 6.18. A constant tensile strain has been applied on the top of the numerical sample resulting in an initial tensile stress of 10 MPa. The sample size is 0.125 m x 0.05 m and the initial crack length of the horizontal pre-crack is 0.02 m. The failure takes place after a creep time of about 8 hours.

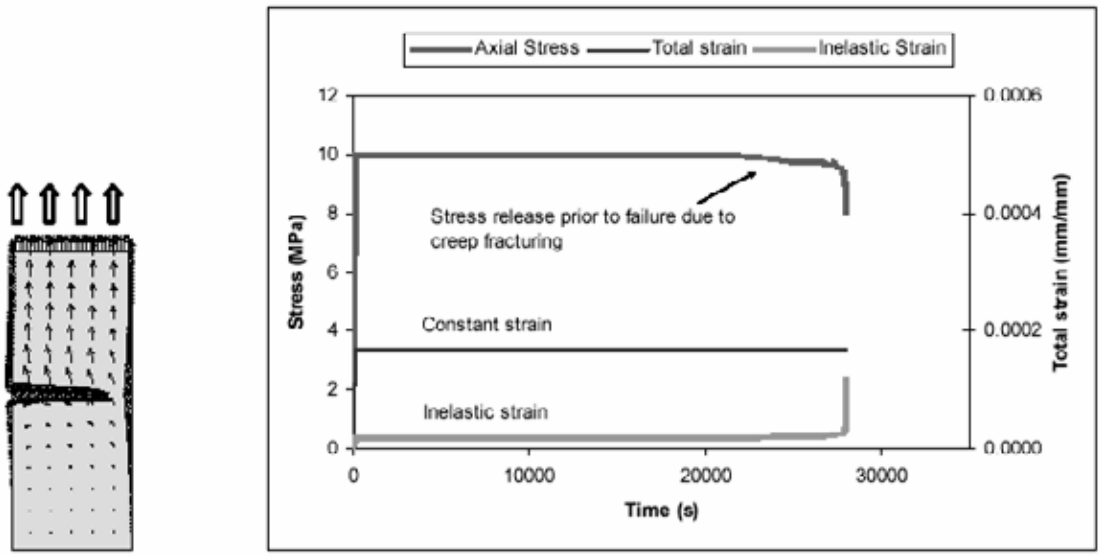

Figure 6.18. Modelled tensile stress release caused by sub-critical crack growth in a sample with a pre-existing horizontal crack under constant strain.

In laboratory compression tests it has been observed that the peak strength of rock is greatly affected by the loading rate (Hakala and Heikkilä, 1997). The strain steps in the previous UCS and triaxial models were not related to time and therefore the true loading rate has not yet been properly simulated. To model the actual loading rate the velocity of growing fractures has to be linked with loading. In the following examples we consider the rock failure as a time dependent fracture process involved in the subcritical

crack growth. Fig. 6.19 shows a model of a short term compression strength test using a typical loading procedure and average properties of Äspö diorite.

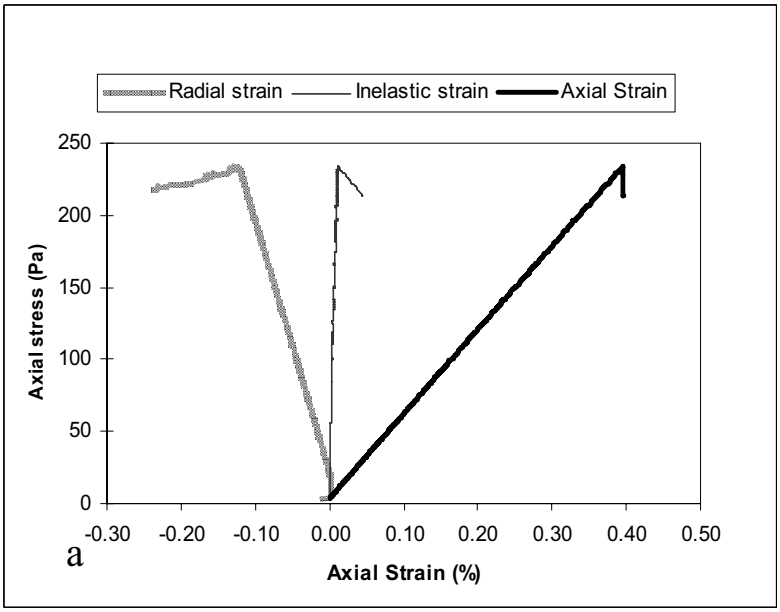

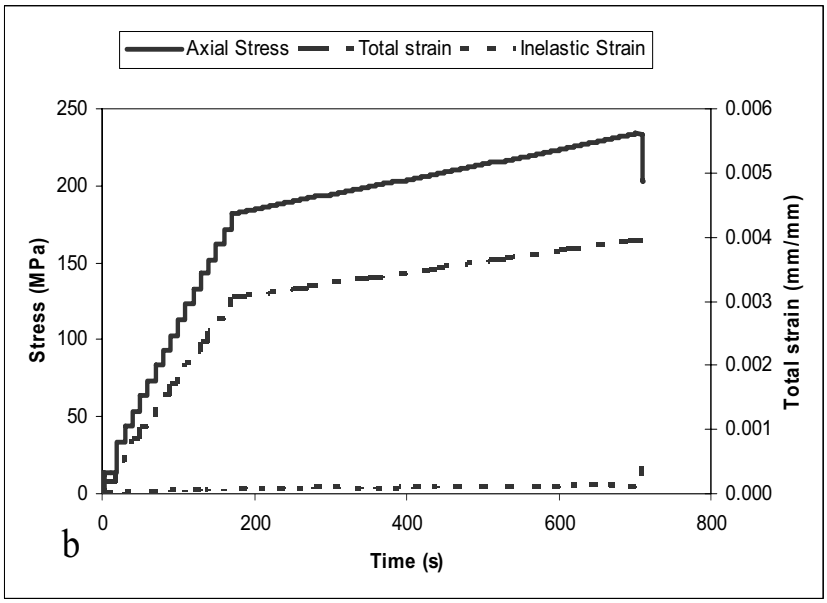

Figure 6.19. Numerical short term strength test using a typical loading procedure and average properties of Äspö diorite. a): Stress strain curve. b): Stress and axial strain vs. time. After the initial fast loading (up to 182 MPa), the load is increased constantly about 0.1MPa/s. Peak strength is reached at 234 MPa. Confining pressure 7 MPa.

The laboratory creep test on Äspö diorite is in progress and the preliminary results have been reported in section 2.3: uniaxial, Brazilian and strain rate stepping testing of Äspö diorite. Fig. 6.20 presents a preliminary strain stepping test simulation using the actual Äspö specific data as reported in section 2.4: development of an experimental method to determine the subcritical crack growth parameters A and n of Äspö diorite. Strain stepping tests will be modelled carefully in the next phase of this project.

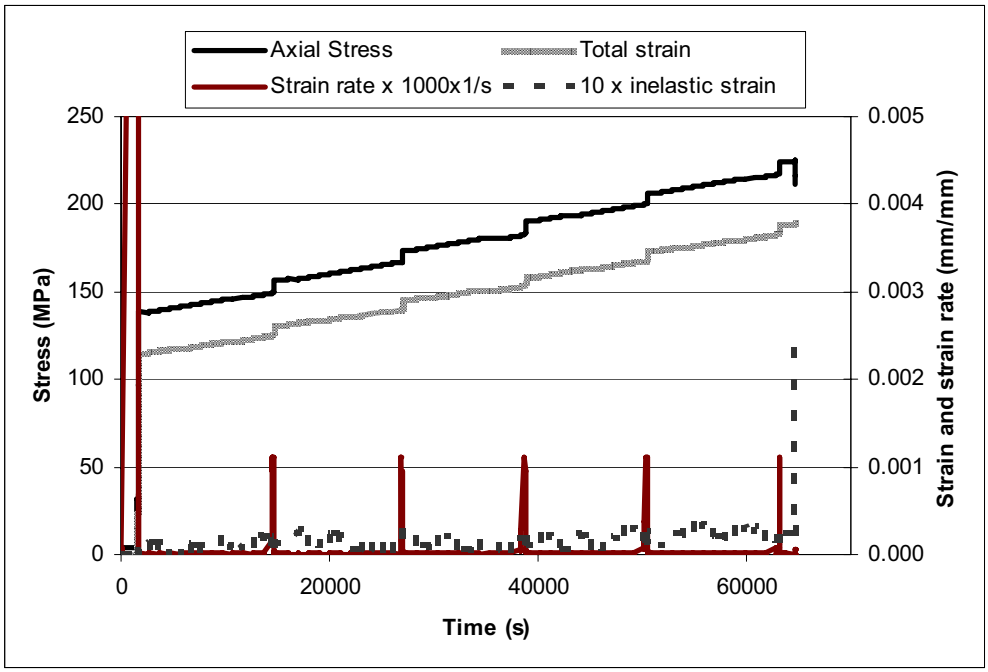

Figure 20. Numerical Strain-Stepping test. The strain stepping test has been described in section 2.3 by J. Antikainen.

6.6 Results and conclusions

6.6.1 Numerical modeling of the structural breakdown of intact rock

Fracture initiation, stable and unstable states of fracture, peak strength and post-peak behaviour including Class II behaviour have been successfully modelled using the recently updated version of the DDM code FRACOD. An important advantage of this code is its capability to model realistically the brittle axial and lateral strain response during the failure process.

Numerical core tests using the suggested parameters for Äspö diorite suggest that the shear failure is the dominating mode of failure even under uniaxial loading. Only slight, stable tensile fracture propagation appears to take place prior to the failure. The opening mode fracturing is more pronounced in the late post-failure stage of failure, where most of the axial fractures tend to dilate.

The post peak failure starts when the applied stress reaches the critical level for unstable fracture propagation. Due to stored strain energy, unstable fracture(s) will continue to propagate until the final failure. As demonstrated by the loading procedure to reveal the Class II behaviour, some extra strain energy can be removed from the system without preventing the successive failure.

The sensitivity analyses suggest that the loading configuration, material properties etc. strongly affects the post-peak behaviour. The failure absorbs energy due to the fracturing process and the failure may require additional load to continue (Class I behaviour). The unstable failure process may also cease when a propagation fracture reach another fracture. However, the simulated axial and radial stress-strain behaviour using typical rock parameters for Äspö rocks strongly suggests a Class II type of rock behaviour.

There exists a large scatter in the laboratory results, especially concerning the peak strength and the following stress-strain response associated with the radial strain controlled loading. However, when applying typical Äspö diorite rock parameters, numerical calculations are in good agreement with the average stress-strain behaviour detected in the laboratory.

6.6.2 Effect of pre-damage

Calculations suggest that besides the material properties and the loading configuration, loading history in terms of pre-damage and inhomogeneity has a significant effect on the failure processes.

When a sample with one or few pre-existing cracks with small angles to the major uniaxial load is modelled, fracture propagation takes place in mode I. A wing crack will grow from the fracture tip in the direction of the major principal stress. However, only slight confinement or interaction with a closely located neighbour crack will suppress the tensile crack and result in mode II type of failure.

6.6.3 Effect of the size of a loading increment and time

For an intact core model the onset of fracture initiation is not dependent on the loading path unless reaching the critical level for crack initiation. Further development of the failure pattern depends on the size of applied load increments. Elastic properties, slipping and opening of the new cracks alter the stress distribution and influence further initiation of cracks. The accumulated pre-damage also affects the level of stress required for stable or unstable fracture propagation and the subsequent post-peak failure process.

A conceptual model for time-dependent crack growth and creep deformation was set up and the concept was successfully implemented in a numerical code. Numerical approximations demonstrate good accuracy compared with an analytical solution. Test modelling with the creep function is ongoing, using core sample models subjected to tension and compression.

6.6.4 Discussion and further improvements

Calculations suggest that fracture initiation is generated in the direction of shear failure. A number of sensitivity analyses were made using low tensile strength of the intact rock. These models suggest more axially oriented tensile cracks and the subsequent failure process is somewhat different compared to models with high tensile strength. Modelled pre-damage has a similar effect. When pre-cracks with a small angle to the major stress are introduced in the model, propagation in the direction of the axial load is more pronounced. The radial strain response is stronger compared to the models with shear failure as the main mode of failure. Effects of pre-damage will be studied with more details in the next phase of this project.

It is suggested that a nonlinear function be implemented in the code to describe more realistically the stress-closure/opening behaviour of joints (Bandis et al. 1983). Currently FRACOD uses constant fracture stiffness. Improving the code to take into

account the stress dependent fracture properties will further improve its capacity to realistically simulate the stress-strain behaviour of loaded rock.

The anisotropy of rock strength can be taken into account using the pre-damage approach presented here. Studies to apply a more scientific approach considering both anisotropy in strength and anisotropy in deformability have been initiated. In the framework of DDM, the solution of the multiple-crack problem requires derivation of the appropriate influence functions in terms of displacements and stresses when displacement discontinuities exist in the solid body.

The preliminary calculations using the creep function seems to work well in both tension and compression. Further work is mainly focused on strain stepping test modelling, as described in the chapter on laboratory tests. Sub-critically growing fractures may contribute to the failure close to the peak strength, causing a decrease of Young's modulus prior to the peak. Also the chemical effects in terms of stress corrosion will be studied in the next phase of this project.

Acknowledgements

We would like to thank the Swedish Nuclear Fuel and Waste Management Company (SKB) for providing laboratory data, and the Finnish Research Programme on Nuclear Waste Management (KYT) and the Academy of Finland (grant 213848) for financial support.

References

Antikainen, J., *Experimental study of creep in hard rock. Preliminary results for the CREEP project*. Helsinki University of Technology Rock Engineering. 2006.

Atkinson, B. K. and Meredith, P. G., *The theory of subcritical crack growth with applications to minerals and rock*. In: Fracture Mechanics of Rock. Academic press, London,111-162. (Pp 477-526. Academic, San Diego, Calif.), 1987.

Backers, T., *Experimental Determination of Subcritical Crack Growth Parameters. GeoFrames,* Potsdam Germany. 2006.

Backers, T., *Determination of Mode I and Mode II Fracture Toughness and Fracture Normal Stiffness of Äspö diorite*. Technical Report GFZ Potsdam, 2003.

Bandis, S. C., Lumsden, A. C. and Barton, N. R., *Fundamentals of Rock Joint Deformation.* Int. J. Rock Mech. Sci. & Geomech. Abstr. 1983; 20(6), 249-268.

Charles, R. J., *Static fatigue of glass.* J. Appli. Phys., 1958 (29), 1549-1560.

Crouch, S.L., Solution of plane elasticity problems by the displacement discontinuity method. Int. J. Num. Methods Engng. 1976(10), 301-343.

Hakala, M. and Heikkilä, E., *Summary report – Development of laboratory tests and the stress-strain behaviour of Olkiluoto mica gneiss*. Posiva Oy, Helsinki. 150 p +app. ISBN 951-652-029-4. 1997.

Jacobsson, L. and Bäckström, A., *Uniaxial compression test of intact rock specimens at dry condition and at saturation by three different liquids:distilled, saline and formation water*. IPR-05-33. Svensk Kärnbränslehantering AB (SKB), Stockholm, Sweden. 2005.

Martin, C. D., *The effect of cohesion loss and stress path on brittle rock strength.* Can. Geotech. J. 1997(34):698-725.

Rinne, M., *Annual Report (preliminary). Time-dependent fracturing of rock mass and modelling of EDZ of a repository for spend nuclear fuel (CREEP)*. Phase 1 (1.1-28.10 2004). Team Fracom. 2004.

Shen, B., *Modelling Time-dependence using FRACOD. Plan for code implementation.* Fracom.Technical report, January 2005.

Shen, B., Rinne, M. and Stephansson, O., *FRACOD^{2D} Users Manual* ver 2.1, 2005.

Shen, B. and Stephansson, O.,*Modification of the G-criterion of crack propagation in compression*. Int. J. of Engineering Fracture Mechanics. 1993;47(2), 177-189.

Staub, I., Andersson, J. C. and Magnor, B., *Äspö Pillar Stability Experiment, Geology and mechanical properties of the rock mass in TASQ.* SKB report R-04-01, Stockholm Sweden. 2004.

Wawersik, W. R. *Detailed analysis of rock failure in laboratory compression tests.* Ph.D. thesis, University of Minnesota. p. 165. 1968.

Wawersik, W. R. and Fairhurst, C., 1969. *A study of brittle rock fracture in laboratory compression experiments.* Int.J. Rock Mech. Min. Sci. & Geomech. Abstr., 1969(l 7), 561-575.

7. Conclusions

A large amount of work has been completed for Phase 2 of Task B of the DECOVALEX-THMC project, especially the much improved understanding of the deformation and failure mechanisms of intact crystalline rock, as demonstrated by the work presented in Chapters 2-6 in this Report. It is impractical to evaluate the complete work of the Research Teams in detail, so a brief summary of the key achievements and outstanding issues is given below to highlight the different aspects of the work for Phase 2 of Task B. Presentation of the other Phases (see the flowchart in the Introduction), especially Phase 3 comprising the Bench Mark Test, will be the subject of future reports.

A) Achievements

A number of core samples of Äspö diorite have been tested at the Borås SP Labroatory in Sweden and also in Germany and Finland under uniaxial compression and other loading conditions, with different sample preparation conditions: dry and being saturated with distilled water, formation water and saline water. The tested data showed differences in the macroscopic elastic and failure properties of intact rock samples with the different saturation conditions, dominated by Class II behaviour (in which the complete stress-strain curve does not monotonically increase in axial strain). Although the data are limited in terms of providing definite conclusions on the chemical effects of fluids on the mechanical properties of intact rock, the physical testing served as an important physical basis for the teams' basic understanding and numerical modelling of the deformation, damage and failure mechanisms of the intact Äspö diorite.

The Research Teams have conducted a wide variety of associated numerical modelling experiments, including FEM, DEM, EPCA and BEM, to simulate the complete uniaxial stress-stain curves and failure of core samples under uniaxial compression, demonstrating a spectrum of computational capacity and flexibility for such a complex deformation and failure process as manifested by the Äspö diorite. This work, together with the data from the physical tests on the core samples, serves as a workable platform for further studies on constitutive model developments of intact rocks considering strain localization, deformation mechanism bifurcation, damage quantification and chemical and time-dependent effects. The achievement is not aimed at how good the fit is between measured and simulated results but to provide a deeper understanding of the differences between the conditions for Class I and Class II behaviour of rocks, the importance of energy exchange during bifurcation, and the importance of lateral boundary constraints. This understanding is also developed through active discussions during and in the intervals between Workshops and Task Force meetings.

The Research Teams paid special attention to the understanding of the damage processes in intact rocks, such as microcracking and plastic deformation, using equivalent continuum and discrete particle mechanics approaches. Although each approach has its own special merits (and shortcomings), their combined application for the focused study of Phase 2 work presents a fruitful multidisciplinary approach for furthering our understanding of the complete rock damage processes.

B) Outstanding issues-physical rock sample tests

Although the core testing with saturation by different fluids (distilled water, formation water and saline water) represents a significant step in understanding chemical effects on the mechanical properties of rocks for the first time in Sweden and in DECOVALEX projects, a clear distinction between chemical effects and effects of material heterogeneity on mechanical properties cannot be established just yet. More work can be envisioned for the future concerning chemical preparation of the samples (e.g. systematic and quantitative geochemical and mineral analysis of both rocks and fluids before, during and after the tests) and microscopic analyses of structural heterogeneity. Another factor is that the process of heating the rock to dryness and then re-saturating it with the chemical solution for that particular test may, in itself, alter the rock properties.

The detailed and quantitative evaluation of the statistical behaviour of microscopic structures (mineral compositions and grain sizes, fractures of different sizes, using the SEM technique for example) could be helpful for more realistic numerical modelling, especially the BEM, DEM and EPCA approaches, in terms of the meso- and micro-scopic structure of rock samples.

Additional monitoring techniques, such as Acoustic Emission (AE), could also be helpful, as demonstrated in rock mechanics and rock engineering practice, for identification of the damage extent and possible damage distribution when considered in combination with numerical modelling.

Systematic investigation of the effects of different loading and boundary conditions on the Class I or Class II behaviour of rocks could be helpful for deepening our understanding and development of more realistic and reliable constitutive models of rocks for dealing with general bifurcation processes such as strain-localization, damage and failure.

C)-Outstanding issues-numerical modelling

Except for the JAEA FEM model, all other numerical models are in 2D, which is a significant shortcoming for simulating the true 3D nature of the rock core testing.

Some of the important model parameters, such as particle size distribution in the KTH team's PFC model, the homogeneity index and seed number in the CAS team's EPCA model and the distribution of the pre-existing microstructures in the FRACOD model, lack a direct correlation with the corresponding structural features identifiable in rock core samples. The uncertainty caused by this shortcoming is difficult to evaluate quantitatively.

A rock may have Class I and Class II behaviour when different loading conditions are applied. The KTH team's PFC model results indicate that this may also be applicable for Äspö diorite, although not physically proven by testing. In fact, that is why it was called Class I or Class II behaviour, rather than a Class I or a Class II rock - because the overall structural behaviour depends on the loading conditions. The numerical capacity of predicting both types of behaviour can improve our understanding of any complex rock behaviour in almost any other circumstances, plus the energy release during failure.

The numerical modelling work for this phase of Task B was focused on simulating the core testing of the Äspö diorite samples. Development of proper constitutive models to represent the damage and failure mechanisms for the subsequent modelling works has not been presented, but is needed.

In general, both the physical core testing and numerical modelling for Phase 2 of Task B of the DECOVALEX-THMC project obtained the required results, although a great deal more work in this direction is still needed. It should be noted that rock deformation with bifurcation, with strain-localization, damage and failure is one of the

most difficult subjects but has far-reaching impacts for rock mechanics in general and the EDZ in particular, and is one of the continuing research subjects in both laboratory and numerical modelling. It may not be possible to solve completely the problems of the major issues in the foreseeable future, especially when the chemical effects are coupled, but the work performed in Phase 2 of Task B has made good progress in this direction and has achieved the required products as envisaged in the research plan.

Certainly, we are now in a position to predict the main detailed mechanistic trends relating to the development of the EDZ. The next stages of the Task B work, the Benchmark Test, assessing uncertainties and writing up the Guidance Document on characterising and measuring the EDZ will thus all be supported by the successful Phase 2 work described in this Report.

www.ski.se

STATENS KÄRNKRAFTINSPEKTION
Swedish Nuclear Power Inspectorate

POST/POSTAL ADDRESS SE-106 58 Stockholm
BESÖK/OFFICE Klarabergsviadukten 90
TELEFON/TELEPHONE +46 (0)8 698 84 00
TELEFAX +46 (0)8 661 90 86
E-POST/E-MAIL ski@ski.se
WEBBPLATS/WEB SITE www.ski.se